Eur. Phys. J. C (2023) 83:667
https://doi.org/10.1140/epjc/s10052-023-11632-6

THE EUROPEAN PHYSICAL JOURNAL C

Check for updates

Regular Article - Experimental Physics

Measurements of the Higgs boson production cross section and couplings in the W boson pair decay channel in proton-proton collisions at $\sqrt{s} = 13\,\text{TeV}$

CMS Collaboration*

CERN, 1211 Geneva 23, Switzerland

Received: 19 June 2022 / Accepted: 9 October 2022 / Published online: 26 July 2023
© CERN for the benefit of the CMS collaboration 2023

Abstract Production cross sections of the standard model Higgs boson decaying to a pair of W bosons are measured in proton-proton collisions at a center-of-mass energy of 13 TeV. The analysis targets Higgs bosons produced via gluon fusion, vector boson fusion, and in association with a W or Z boson. Candidate events are required to have at least two charged leptons and moderate missing transverse momentum, targeting events with at least one leptonically decaying W boson originating from the Higgs boson. Results are presented in the form of inclusive and differential cross sections in the simplified template cross section framework, as well as couplings of the Higgs boson to vector bosons and fermions. The data set collected by the CMS detector during 2016–2018 is used, corresponding to an integrated luminosity of $138\,\text{fb}^{-1}$. The signal strength modifier μ, defined as the ratio of the observed production rate in a given decay channel to the standard model expectation, is measured to be $\mu = 0.95^{+0.10}_{-0.09}$. All results are found to be compatible with the standard model within the uncertainties.

1 Introduction

After the observation of a scalar particle compatible with the standard model (SM) Higgs boson by the ATLAS and CMS Collaborations in 2012 [1–3], the two experiments have focused on performing precision measurements of the properties of the new particle. The large data sample collected at the CERN LHC during the data taking periods through 2018 allowed the measurement of the Higgs boson quantum numbers and couplings to other SM particles with an unprecedented level of accuracy [4]. All results reported so far are compatible with the SM within the current uncertainties.

Among all the Higgs boson decay channels predicted by the SM, the one into a pair of W bosons has the second largest branching fraction ($\approx 22\%$), while benefitting from a lower background with respect to the more probable decay in a pair of b quarks. This combination makes this channel one of the most sensitive for measuring the production cross section of the Higgs boson and its couplings to SM particles. This paper presents the measurement of the Higgs boson properties in the $\text{H} \to \text{WW}$ decay channel targeting the gluon fusion (ggH) and vector boson fusion (VBF) production mechanisms, as well as associated production with a vector boson (VH, where V stands for either a W or a Z boson). The measurement utilizes final states with at least two charged leptons arising either from the associated vector boson or from the products of the $\text{H} \to \text{WW}$ decays. In all cases at least one of the W bosons originating from the Higgs boson is required to decay leptonically.

The properties of the Higgs boson are probed by measuring the inclusive cross sections for each production mechanism, as well as the production cross sections in finer phase spaces defined according to the simplified template cross section (STXS) framework [5]. In addition, measurements of the Higgs boson couplings to fermions and vector bosons are presented.

The analysis is based on proton-proton (pp) collision data produced at the LHC at $\sqrt{s} = 13\,\text{TeV}$ and collected by the CMS detector during 2016–2018, for a total integrated luminosity of about $138\,\text{fb}^{-1}$. This paper builds on previous analyses published by the CMS Collaboration in the $\text{H} \to \text{WW}$ channel focused on the inclusive production cross section and coupling measurements at $\sqrt{s} = 7$, 8, and 13 TeV [6,7], and on differential fiducial production cross section measurements at 8 TeV [8] and 13 TeV [9]. Similar measurements have also been reported in several Higgs boson decay channels by the ATLAS and CMS Collaborations [10–14].

Results reported in this paper show an overall improvement of the measurement accuracy thanks to new analysis techniques specifically devised to increase the sensitivity to particular production mechanisms (e.g., VBF with a different-flavor lepton pair in the final state), to the inclusion of new channels that have not been investigated in Run 2

*e-mail: cms-publication-committee-chair@cern.ch

before, such as VBF and VH production with a same-flavor pair of charged leptons and a hadronically decaying V, and ZH production with a three-lepton final state, and to the larger integrated luminosity analyzed. Moreover, WH production with two same sign leptons is measured for the first time in CMS. Tabulated results are provided in the HEPData record for this analysis [15].

This paper is organized as follows. A brief overview of the CMS apparatus is given in Sect. 2. The data set and simulated samples used are described in Sect. 3. Sections 4–8 describe in detail the event selection and categorization strategy, as well as the discriminating variables used to target each final state. The estimation of the backgrounds is described in Sect. 9, and the sources of systematic uncertainty and their treatment are given in Sect. 10. Results are presented in Sect. 11. Finally, closing remarks are given in Sect. 12.

2 The CMS detector and event reconstruction

The CMS apparatus is a general purpose detector designed to tackle a wide range of measurements. The central feature of CMS is a superconducting solenoid of 6 m internal diameter, providing a magnetic field of 3.8 T. Within the solenoid volume are a silicon pixel and strip tracker, a lead tungstate crystal electromagnetic calorimeter (ECAL), and a brass and scintillator hadron calorimeter (HCAL), each composed of a barrel and two endcap sections. Forward calorimeters extend the pseudorapidity (η) coverage provided by the barrel and endcap detectors. Muons are detected in gas-ionization chambers embedded in the steel flux-return yoke outside the solenoid.

The events of interest are selected using a two-tiered trigger system. The first level, composed of custom hardware processors, uses information from the calorimeters and muon detectors to select events at a rate of around 100 kHz within a fixed latency of about 4 μs [16]. The second level, known as the high-level trigger (HLT), consists of a farm of processors running a version of the full event reconstruction software optimized for fast processing, and reduces the event rate to around 1 kHz before data storage [17]. Events passing the trigger selection are stored for offline reconstruction. A more detailed description of the CMS detector, together with a definition of the coordinate system and the kinematic variables, can be found in Ref. [18].

Muons are identified and their momenta are measured in the range $|\eta| < 2.4$ by matching tracks in the muon system and the silicon tracker. The single muon trigger efficiency exceeds 90% over the full η range, and the efficiency to reconstruct and identify muons is greater than 96%. The relative transverse momentum (p_{T}) resolution for muons with p_{T} up to 100 GeV is 1% in the barrel and 3% in the endcaps [19,20].

Electrons are identified and their momenta are measured in the interval $|\eta| < 2.5$ by combining tracks in the silicon tracker with spatially compatible energy deposits in the ECAL, also accounting for the energy of bremsstrahlung photons likely originating from the electron track. The single electron trigger efficiency exceeds 90% over the full η range. The efficiency to reconstruct and identify electrons ranges between 60 and 80% depending on the lepton p_{T}. The momentum resolution for electrons with $p_{\mathrm{T}} \approx 45$ GeV from $\mathrm{Z} \to \mathrm{ee}$ decays ranges from 1.7 to 4.5% depending on the η region. The resolution is generally better in the barrel than in the endcaps and also depends on the bremsstrahlung energy emitted by the electron as it traverses the material in front of the ECAL [21].

In order to achieve better rejection of nonprompt leptons, increasing the sensitivity of the analysis, leptons are required to be isolated and well reconstructed by imposing a set of requirements on the quality of the track reconstruction, shape of calorimetric deposits, and energy flux in the vicinity of the particle trajectory. On top of these criteria, a selection on a dedicated multivariate analysis (MVA) tagger developed for the CMS $\mathrm{t\bar{t}H}$ analysis [22], referred to as ttHMVA, is added in all analysis categories for muon candidates. In categories targeting the VH production modes with leptonically decaying V boson, it is found that adding a selection on the ttHMVA tagger for electrons improves the sensitivity of the analysis.

Multiple pp interaction vertices are identified from tracking information by use of the adaptive vertex fitting algorithm [23]. The primary vertex is taken to be the vertex corresponding to the hardest scattering in the event, evaluated using tracking information alone, as described in Section 9.4.1 of Ref. [24].

The particle-flow (PF) algorithm [25] aims to reconstruct and identify each individual particle in an event, with an optimized combination of information from the various elements of the CMS detector. The energy of muons is obtained from the curvature of the corresponding track. The energy of charged hadrons is determined from a combination of their momentum measured in the tracker and the matching ECAL and HCAL energy deposits, corrected for the response function of the calorimeters to hadronic showers. The energy of photons is obtained from the ECAL measurement. The energy of electrons is determined from a combination of the electron momentum at the primary interaction vertex as determined by the tracker, the energy of the corresponding ECAL cluster, and the energy sum of all bremsstrahlung photons spatially compatible with originating from the electron track. Finally, the energy of neutral hadrons is obtained from the corresponding corrected ECAL and HCAL energies.

Hadronic jets are reconstructed from PF objects using the infrared and collinear safe anti-k_{T} algorithm [26,27] with a distance parameter of 0.4. The jet momentum is determined from the vector sum of all PF candidate momenta in the jet.

From simulation, reconstructed jet momentum is found to be, on average, within 5–10% of the momentum of generator jets, which are jets clustered from all generator-level final-state particles excluding neutrinos, over the entire p_T spectrum and detector acceptance. Additional pp interactions within the same or nearby bunch crossings (pileup) can contribute additional tracks and calorimetric energy deposits to the jet momentum. To mitigate this effect, charged particles identified as originating from pileup vertices are discarded, and an offset correction is applied for remaining contributions from neutral pileup particles [25]. Jet energy corrections are derived from simulation studies so that the average measured response of jets becomes identical to that of generator jets. In situ measurements of the momentum imbalance in dijet, photon+jet, Z+jet, and multijet events are used to account for any residual differences in jet energy scale in data and simulation [28,29]. The jet energy resolution amounts typically to 15% at 10 GeV, 8% at 100 GeV, and 4% at 1 TeV. Additional selection criteria are applied to each jet to remove jets potentially dominated by anomalous contributions from various subdetector components or reconstruction failures. Jets are measured in the range $|\eta| < 4.7$. In the analysis of data recorded in 2017, to eliminate spurious jets caused by detector noise, all jets in the range $2.5 < |\eta| < 3.0$ were excluded [30].

We refer to the identification of jets likely originating from b quarks as b tagging [31,32]. For each jet in the event a score is calculated through a multivariate combination of different jet properties, making use of boosted decision trees (BDTs) and deep neural networks (DNNs). Jets are considered b tagged if their associated score exceeds a threshold, tuned to achieve a certain tagging efficiency as measured in $\mathrm{t\bar{t}}$ events. Typically three thresholds, called working points (WPs) in the following, are provided, labeled loose, medium, and tight, corresponding to probabilities of mistagging a jet originating from a lighter quark as coming from a bottom quark of 10, 1, and 0.1%, respectively. Unless otherwise specified, the loose WP of the DeepCSV tagger is used throughout this paper.

The missing transverse momentum vector $\vec{p}_{\mathrm{T}}^{\,\mathrm{miss}}$ is computed as the negative vector sum of the transverse momenta of all the PF candidates in an event, and its magnitude is denoted as $p_{\mathrm{T}}^{\mathrm{miss}}$ [33]. The $\vec{p}_{\mathrm{T}}^{\,\mathrm{miss}}$ is modified to account for corrections to the energy scale of the reconstructed jets in the event. The pileup per particle identification algorithm [34] is applied to reduce the pileup dependence of the $\vec{p}_{\mathrm{T}}^{\,\mathrm{miss}}$ observable. The $\vec{p}_{\mathrm{T}}^{\,\mathrm{miss}}$ is computed from the PF candidates weighted by their probability to originate from the primary interaction vertex [33].

3 Data sets and simulations

The data sets used in the analysis were recorded by the CMS detector in 2016, 2017, and 2018, corresponding to an integrated luminosity of 36.3, 41.5, and 59.7 fb^{-1}, respectively [35–37].

The events selected in the analysis are required to pass criteria based on HLT algorithms that require the presence of either one or two electrons or muons, satisfying isolation and identification requirements. For the 2016 data set, the single-electron trigger requires a p_T threshold of 25 GeV for electrons with $|\eta| < 2.1$ and 27 GeV for $2.1 < |\eta| < 2.5$. For the single-muon trigger the p_T threshold is 24 GeV for $|\eta| < 2.4$. In the dielectron (dimuon) trigger the p_T thresholds of the leading (highest p_T) and trailing (second-highest p_T) electron (muon) are respectively 23 (17) and 12 (8) GeV. In the dilepton $\mathrm{e\mu}$ trigger, the p_T thresholds are 23 and 12 GeV for the leading and trailing lepton, respectively. For the first part of data taking in 2016, a lower p_T threshold of 8 GeV for the trailing muon was used. In the 2017 data set, the p_T thresholds of the single electron and single muon triggers are raised respectively to 35 and 27 GeV, while they are set to 32 and 24 GeV in the 2018 data set. For both 2017 and 2018 data sets, the p_T thresholds of the dilepton triggers are kept the same as the last part of the 2016 data set. The trigger selection is summarized in Table 1.

Monte Carlo (MC) event generators are used in the analysis to model the signal and background processes. Three independent sets of simulated events, corresponding to the 2016, 2017, and 2018 data sets, are used for each process of interest, in order to take into account year-dependent effects in the CMS detector, data taking, and event reconstruction. Despite different matrix element generators being used for different processes, all simulated events corresponding to a given data set share the same set of parton distribution functions (PDFs), underlying event (UE) tune, and parton shower (PS) configuration. The PDF set used is NNPDF 3.0 [38,39] at NLO for 2016 and NNPDF 3.1 [40] at NNLO for 2017 and 2018. The CUETP8M1 [41] tune is used to describe the UE in 2016 simulations, while the CP5 [42] tune is adopted in 2017 and 2018 simulated events. For all the simulations, the matrix-element event generators are interfaced with PYTHIA [43] 8.226 in 2016, and 8.230 in 2017 and 2018, for the UE description, PS, and hadronization.

Simulated events are used in the analysis to model Higgs boson production through ggH, VBF, VH, and associated production with top quarks ($\mathrm{t\bar{t}H}$) or bottom quarks ($\mathrm{b\bar{b}H}$), although $\mathrm{t\bar{t}H}$ and $\mathrm{b\bar{b}H}$ have a negligible contribution in the

Table 1 Trigger requirements on the data set used in the analysis

Trigger	Year	Requirements
Single electron	2016	$p_T > 25\,\text{GeV}$, $\lvert\eta\rvert < 2.1$ or $p_T > 27\,\text{GeV}$, $2.1 < \lvert\eta\rvert < 2.5$
	2017	$p_T > 35\,\text{GeV}$, $\lvert\eta\rvert < 2.5$
	2018	$p_T > 32\,\text{GeV}$, $\lvert\eta\rvert < 2.5$
Single muon	2016	$p_T > 24\,\text{GeV}$, $\lvert\eta\rvert < 2.4$
	2017	$p_T > 27\,\text{GeV}$, $\lvert\eta\rvert < 2.4$
	2018	$p_T > 24\,\text{GeV}$, $\lvert\eta\rvert < 2.4$
Double electron	All years	$p_{T1} > 23\,\text{GeV}$, $p_{T2} > 12\,\text{GeV}$, $\lvert\eta_{1,2}\rvert < 2.5$
Double muon	All years	$p_{T1} > 17\,\text{GeV}$, $p_{T2} > 8\,\text{GeV}$, $\lvert\eta_{1,2}\rvert < 2.4$
Electron-muon	All years	$p_{T1} > 23\,\text{GeV}$, $p_{T2} > 12\,\text{GeV}$
		$p_{T2} > 8\,\text{GeV}$ in first part of 2016 data taking
		$\lvert\eta_e\rvert < 2.5$, $\lvert\eta_\mu\rvert < 2.4$

analysis phase space. All Higgs boson production processes except $b\bar{b}H$ are generated using the POWHEG v2 [44–50] event generator, which describes Higgs boson production at next-to-leading order (NLO) accuracy in quantum chromodynamics (QCD), including finite quark mass effects. Instead, $b\bar{b}H$ production is simulated using the MADGRAPH5_aMC@NLO v2.2.2 generator [51]. The ZH production process is simulated including both gluon- and quark-induced contributions. The MINLO HVJ [49] extension of POWHEG v2 is used for the simulation of WH and quark-induced ZH production, providing a description of VH+0- and 1-jet processes with NLO accuracy. For ggH production, the simulated events are reweighted to match the NNLOPS [52,53] prediction in the hadronic jet multiplicity (N_{jet}) and Higgs boson transverse momentum (p_T^H) distributions, according to a two-dimensional map constructed using these observables. Moreover, for a better description of the phase space with more than one jet, the MINLO HJJ [54] generator is used, giving NLO accuracy for $N_{\text{jet}} \geq 2$ and leading order (LO) accuracy for $N_{\text{jet}} \geq 3$. The simulated samples are normalized to the cross sections recommended in Ref. [55]; in particular, the next-to-next-to-next-to-leading order cross section is used to normalize the ggH sample. The Higgs boson mass (m_H) in the event generation is assumed to be 125 GeV, while the value of 125.38 GeV [56] is used for the calculation of cross sections and branching fractions, yielding values of 48.31 pb, 3.77 pb, 1.36 pb, 0.88 pb, and 0.12 pb for the ggH, VBF, WH, quark-induced ZH, and gluon-induced ZH processes, respectively, and 22.0% for the $H \to WW$ branching ratio [55]. The decay to a pair of W bosons and subsequently to leptons or hadrons is performed using the JHUGEN [57] v5.2.5 generator in 2016, and v7.1.4 in 2017 and 2018, for ggH, VBF, and quark-induced ZH samples. The Higgs boson and W boson decays are performed using PYTHIA 8.212 for the other signal simulations. For the ggH, VBF, and VH production mechanisms, additional Higgs boson simulations are produced using the POWHEG v2 generator, where the Higgs boson decays to a pair of τ leptons. These events are treated as signal in the analysis, with the exception of the measurement in the STXS framework, in which they are treated as background.

The background processes are simulated using several event generators. The quark-initiated nonresonant WW process is simulated using POWHEG v2 [58] with NLO accuracy for the inclusive production. The MCFM v7.0 [59–61] generator is used for the simulation of gluon-induced WW production at LO accuracy, and the normalization is chosen to match the NLO cross section [62]. The nonresonant electroweak (EW) production of WW pairs with two additional jets (in the vector boson scattering topology) is simulated at LO accuracy with MADGRAPH5_aMC@NLO v2.4.2 using the MLM matching and merging scheme [63]. Top quark pair production ($t\bar{t}$), as well as single top quark processes, including tW, s-, and t-channel contributions, are simulated with POWHEG v2 [64–66]. The Drell–Yan (DY) production of charged-lepton pairs is simulated at NLO accuracy with MADGRAPH5_aMC@NLO v2.4.2 with up to two additional partons, using the FxFx matching and merging scheme [67]. Production of a W boson associated with an initial-state radiation photon ($W\gamma$) is simulated with MADGRAPH5_aMC@NLO v2.4.2 at NLO accuracy with up to one additional parton in the matrix element calculations and the FxFx merging scheme. Diboson processes containing at least one Z boson or a virtual photon (γ^*) with mass down to 100 MeV are generated with POWHEG v2 [58] at NLO accuracy. Production of a W boson in association with a γ^* ($W\gamma^*$) for masses below 100 MeV is simulated by PYTHIA 8.212 in the parton showering of $W\gamma$ events. Triboson processes with inclusive decays are also simulated at NLO accuracy with MADGRAPH5_aMC@NLO v2.4.2.

For all processes, the detector response is simulated using a detailed description of the CMS detector, based on the GEANT4 package [68]. The distribution of the number of pileup interactions in the simulation is reweighted to match

Table 2 Overview of the selection defining the analysis categories (a more detailed breakdown is given in Table 12)

Category	Number of leptons	Number of jets	Subcategorization
ggH	2	—	(DF, SF) × (0 jets, 1 jet, ≥2 jets)
VBF	2	≥2	(DF, SF)
VH2j	2	≥2	(DF, SF)
WHSS	2	≥1	(DF, SF) × (1 jet, 2 jets)
WH3ℓ	3	0	SF lepton pair with opposite or same sign
ZH3ℓ	3	≥1	(1 jet, 2 jets)
ZH4ℓ	4	—	(DF, SF)

the one observed in data. The average number of pileup interactions was 23 (32) in 2016 (2017 and 2018).

The efficiency of the trigger system is evaluated in data on a per-lepton basis by selecting dilepton events compatible with originating from a Z boson. The per-lepton efficiencies are then combined probabilistically (i.e., the overall efficiency for an event passing any of the triggers listed above is calculated) to obtain the overall efficiencies of the trigger selections used in the analysis. The procedure has been validated by comparing the resulting efficiencies with MC simulation of the trigger. A correction has been derived as a function of $\Delta R = \sqrt{(\Delta\eta)^2 + (\Delta\phi)^2}$ between the two leptons to account for any residual discrepancy, which is found to be on average below 1%. The resulting efficiencies are then applied directly on simulated events.

4 Event selection and categorization

The analysis targets events in which a Higgs boson is produced via ggH, VBF, or VH processes, and subsequently decays to a pair of W bosons. Events are selected by requiring at least two charged leptons (electrons or muons) with high p_{T}, high $p_{\mathrm{T}}^{\mathrm{miss}}$, and a varying number of hadronic jets. Throughout this paper, unless otherwise specified, only hadronic jets with $p_{\mathrm{T}} > 30$ GeV are considered. Categories targeting Higgs bosons produced via ggH, VBF, and VH with a hadronically decaying vector boson (VH2j) are subdivided in different-flavor (DF) and same-flavor (SF) by selecting eμ, and ee/$\mu\mu$ pairs, respectively. Categories targeting VH production with a leptonically decaying vector boson are subdivided in four subcategories based on the number of leptons and hadronic jets required: WHSS (same sign), WH3ℓ, ZH3ℓ, and ZH4ℓ targeting the WH $\to \ell^{\pm}\ell^{\pm}2\nu$qq, WH $\to 3\ell 3\nu$, ZH $\to 3\ell\nu$qq, and ZH $\to 4\ell 2\nu$ processes, respectively. In all cases events containing additional leptons with $p_{\mathrm{T}} > 10$ GeV are rejected. A summary of the different categories is given in Table 2, with a more detailed breakdown given in Table 12.

Across all categories, in the 2016 data set, events are required to pass single- or double-lepton triggers. An additional requirement is placed on the lepton p_{T} to be above 10 GeV, and the highest p_{T} (leading) lepton in the event is furthermore required to have $p_{\mathrm{T}} > 25$ GeV. In the 2017 and 2018 data sets the threshold for leptons is increased to 13 GeV because of a change in the trigger setup. Where yields suffice, events are further split according to the charge and p_{T} ordering of the dilepton system, p_{T} of the subleading lepton, and number of hadronic jets in the event, as detailed in following sections. The number of expected and observed events in each category are given in Sect. 11.

5 Gluon fusion categories

This section describes the categories targeting the ggH production mechanism, both in DF and SF final states. In DF final states, the main background processes are nonresonant WW, top quark production (both single and pair), DY production of a pair of τ leptons that subsequently decay to an eμ pair and associated neutrinos, and W+jets events when a jet is misidentified as a lepton. Subdominant backgrounds include WZ, ZZ, Vγ, Vγ^*, and VVV production. In SF final states, the dominant background contribution is given by DY events, with subdominant components arising from top quark and WW production, as well as events with misidentified leptons.

5.1 Different-flavor ggH categories

On top of the common selection, the leading leptons are required to form an eμ pair with opposite charge. Contributions arising from top quark production are reduced by rejecting events containing any jet with $p_{\mathrm{T}} > 20$ GeV that is identified as originating from a bottom quark by the tagging algorithm. The dilepton invariant mass $m_{\ell\ell}$ is required to be above 12 GeV to suppress QCD events with multiple misidentified jets. Events with no genuine missing transverse momentum (arising from the presence of neutrinos in signal events), as well as $\tau\tau$ events, are suppressed by requiring $p_{\mathrm{T}}^{\mathrm{miss}} > 20$ GeV. The latter are further reduced by requiring the p_{T} of the dilepton system $p_{\mathrm{T}}^{\ell\ell}$ to exceed 30 GeV, as

leptons arising from a $\tau\tau$ pair are found to have on average lower p_{T} than those coming from a WW pair. Finally, to further suppress contributions from $\tau\tau$ and W+jets events, where the subleading lepton does not arise from a W boson decay, the transverse mass built with $\vec{p}_{\mathrm{T}}^{\,\mathrm{miss}}$ and the momentum of the subleading lepton $m_{\mathrm{T}}(\ell_2, p_{\mathrm{T}}^{\mathrm{miss}})$ is required to be greater than 30 GeV, where m_{T} for a collection of particles $\{P_i\}$ with transverse momenta $\vec{p}_{\mathrm{T},i}$ is defined as:

$$m_{\mathrm{T}}(\{P_i\}) = \sqrt{\left(\sum|\vec{p}_{\mathrm{T},i}|\right)^2 - \left|\sum \vec{p}_{\mathrm{T},i}\right|^2}. \quad (1)$$

Selected events are further split into subcategories in order to exploit the peculiar kinematics of the target final state. Events with zero, one, and more than one hadronic jets are separated into distinct categories. In order to better constrain the W+jets background, the 0- and 1-jet categories are subdivided into two categories each according to the charge and p_{T} ordering of the dilepton pair. This subdivision exploits the fact that the signal is charge symmetric, while in W+jets events W^+ bosons are more abundant than W^- bosons. Finally, these subcategories are further divided according to whether the p_{T} of the subleading lepton ($p_{\mathrm{T}2}$) is above or below 20 GeV. This results in a four-fold partitioning of the 0- and 1-jet DF ggH categories. In categories with more than one hadronic jet, a selection on the invariant mass of the leading dijet pair m_{jj} is added to ensure that there is no overlap with the VBF and VH categories.

Given the presence of neutrinos in the final state, the mass of the Higgs boson candidate can not be reconstructed in the WW channel. Nevertheless, specific features of the channel make it possible to achieve good sensitivity. In particular, the scalar nature of the Higgs boson results in the two final-state leptons being preferentially emitted in the same hemisphere. This fact compresses the distribution of $m_{\ell\ell}$ for signal events to lower values with respect to the nonresonant WW process. This shape difference alone however is not sufficient to disentangle the signal from other background processes, such as DY production of $\tau\tau$ pairs and $\mathrm{V}\gamma$, that populate the low-$m_{\ell\ell}$ phase space. The Higgs boson transverse mass $m_{\mathrm{T}}^{\mathrm{H}} = m_{\mathrm{T}}(\ell\ell, p_{\mathrm{T}}^{\mathrm{miss}})$ is thus introduced as a second discriminating variable. A selection on $m_{\mathrm{T}}^{\mathrm{H}}$ is applied by requiring its value to be above 60 GeV for signal events. It is found that signal and background events populate different regions of the $(m_{\ell\ell}, m_{\mathrm{T}}^{\mathrm{H}})$ plane. The signal extraction fit is therefore performed on a two-dimensional $(m_{\ell\ell}, m_{\mathrm{T}}^{\mathrm{H}})$ binned template, allowing for good signal-to-background discrimination.

In order to optimize background subtraction in the signal region (SR), two additional orthogonal selections are defined for each jet multiplicity category. These define two sets of control regions (CR), enriched in $\tau\tau$ and top quark events, respectively. They are defined by the same selection as the SR, but inverting the b jet veto for the top CR and the $m_{\mathrm{T}}^{\mathrm{H}}$ requirement for the $\tau\tau$ CR. The full selection and categorization strategy is summarized in Table 3. Observed distributions for $m_{\ell\ell}$ and $m_{\mathrm{T}}^{\mathrm{H}}$ for the 0-, 1-, and 2-jet ggH categories are shown in Figs. 1, 2, and 3, respectively. The WZ, ZZ, $\mathrm{V}\gamma$, $\mathrm{V}\gamma^*$, and VVV backgrounds are shown together as minor backgrounds. The observed $m_{\ell\ell}$ and $m_{\mathrm{T}}^{\mathrm{H}}$ distributions for the 0-, 1-, and 2-jet CRs enriched in top quark events are shown in Figs. 4, 5, and 6, and for the $\tau\tau$ CRs in Figs. 7, 8, and 9.

5.2 Same-flavor ggH categories

The categories described in this section target the ggH production mechanism in final states with either two electrons or two muons. The two leading leptons in the event are required to form an oppositely charged ee or $\mu\mu$ pair. Events containing at least one b-tagged jet with $p_{\mathrm{T}} > 20$ GeV are discarded. Low-mass resonances are suppressed by requiring $m_{\ell\ell} > 12$ GeV. The W+jets background is reduced by requiring the p_{T} of the dilepton system to exceed 30 GeV. Events are also required to have $p_{\mathrm{T}}^{\mathrm{miss}} > 20$ GeV to enrich the selection in processes with genuine missing transverse momentum. Finally, to reduce the DY background, which is dominant in this channel, a veto is placed on events in which $m_{\ell\ell}$ is within 15 GeV of the nominal mass of the Z boson (m_{Z}).

Events are divided in subcategories based on the number of hadronic jets, and further selections on $m_{\mathrm{T}}^{\mathrm{H}}$, $m_{\ell\ell}$, and the azimuthal angle between the two leading leptons ($\Delta\phi_{\ell\ell}$) are applied depending on the subcategory. A dedicated multivariate discriminant based on a DNN, called DYMVA in the following, is built and trained with the TensorFlow package [69] to distinguish signal events from DY events. The DNN is trained separately for each jet multiplicity subcategory. The architecture of the DNN is that of a feed-forward multilayer perceptron, taking 21, 22, and 27 input variables in the 0-, 1-, and 2-jet categories, respectively. These include kinematic information from the dilepton system, $\vec{p}_{\mathrm{T}}^{\,\mathrm{miss}}$, and jets where present. To better constrain the top quark and WW backgrounds, two CRs are defined in each jet multiplicity subcategory, enriched in the respective processes. The full selection is given in Table 4. The selection efficiency of the requirement on the DYMVA score in 0-jet categories is found to be approximately 50, 7, and 30% for signal, DY, and total background events, respectively. In 1- and 2-jet categories the corresponding efficiencies are ≈50, 1, and 10%. Once the selection is performed, the signal is extracted via a simultaneous fit to the number of events in each category.

6 Vector boson fusion categories

This section describes the categories targeting the VBF production mechanism, both in DF and SF final states. This mode involves the production of a Higgs boson in association with a

Table 3 Summary of the selection used in different-flavor ggH categories

Subcategories	Selection
Global selection	
—	$p_{T1} > 25\,\text{GeV}$, $p_{T2} > 10\,\text{GeV}$ (2016) or 13 GeV
	$p_T^{miss} > 20\,\text{GeV}$, $p_T^{\ell\ell} > 30\,\text{GeV}$, $m_{\ell\ell} > 12\,\text{GeV}$
	eμ pair with opposite charge
0-jet ggH category	
$\ell^\pm\ell^\mp$, $p_{T2} \lesseqgtr 20\,\text{GeV}$	$m_T^H > 60\,\text{GeV}$, $m_T(\ell_2, p_T^{miss}) > 30\,\text{GeV}$
	$p_{T2} \lesseqgtr 20\,\text{GeV}$
	No jet with $p_T > 30\,\text{GeV}$
	No b-tagged jet with $p_T > 20\,\text{GeV}$
Top quark CR	As SR but with no m_T^H requirement, $m_{\ell\ell} > 50\,\text{GeV}$
	At least 1 b-tagged jet with $20 < p_T < 30\,\text{GeV}$
ττ CR	As SR but with $m_T^H < 60\,\text{GeV}$
	$40 < m_{\ell\ell} < 80\,\text{GeV}$
1-jet ggH category	
$\ell^\pm\ell^\mp$, $p_{T2} \lesseqgtr 20\,\text{GeV}$	$m_T^H > 60\,\text{GeV}$, $m_T(\ell_2, p_T^{miss}) > 30\,\text{GeV}$
	$p_{T2} \lesseqgtr 20\,\text{GeV}$
	1 jet with $p_T > 30\,\text{GeV}$
	No b-tagged jet with $p_T > 20\,\text{GeV}$
Top quark CR	As SR but with no m_T^H requirement, $m_{\ell\ell} > 50\,\text{GeV}$
	At least 1 b-tagged jet with $p_T > 30\,\text{GeV}$
ττ CR	As SR but with $m_T^H < 60\,\text{GeV}$
	$40 < m_{\ell\ell} < 80\,\text{GeV}$
2-jet ggH category	
SR	$m_T^H > 60\,\text{GeV}$, $m_T(\ell_2, p_T^{miss}) > 30\,\text{GeV}$
	$p_{T2} \lesseqgtr 20\,\text{GeV}$
	At least 2 jets with $p_T > 30\,\text{GeV}$
	No b-tagged jet with $p_T > 20\,\text{GeV}$
	$m_{jj} < 65\,\text{GeV}$ or $105 < m_{jj} < 120\,\text{GeV}$
Top quark CR	As SR but with no m_T^H requirement, $m_{\ell\ell} > 50\,\text{GeV}$
	At least one b-tagged jet with $p_T > 30\,\text{GeV}$
ττ CR	As SR but with $m_T^H < 60\,\text{GeV}$
	$40 < m_{\ell\ell} < 80\,\text{GeV}$

pair of forward-backward jets. The dijet system is characterized by a large m_{jj}, large pseudorapidity separation $\Delta\eta_{jj}$, and low hadronic activity in the pseudorapidity region between the tagging jets. The fully leptonic final state in the VBF category therefore consists of two isolated leptons, large p_T^{miss} from the two undetectable neutrinos, and a pair of forward-backward jets. The main background processes for the VBF categories are the same as for the ggH categories. An additional complication however arises in the entanglement of VBF and ggH events, given the identical decay mode and the fact that the ggH cross section is larger than the VBF one by one order of magnitude.

6.1 Different-flavor VBF categories

On top of the common global selection, the same requirements on leptons and p_T^{miss} used in the DF ggH categories are applied. In this case, however, there are no subcate-

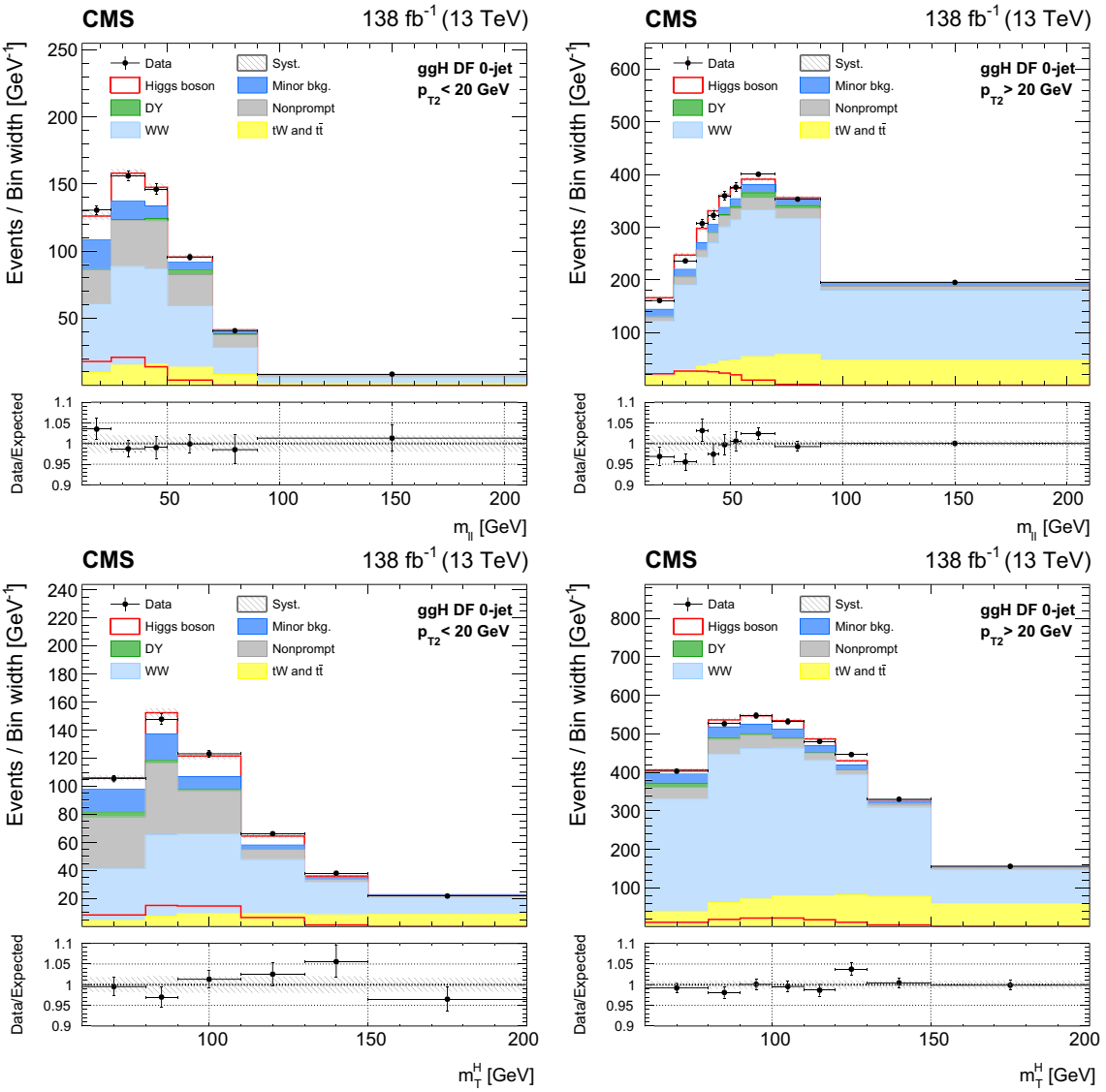


Fig. 1 Observed distributions of the $m_{\ell\ell}$ (upper) and $m_{\mathrm{T}}^{\mathrm{H}}$ (lower) fit variables in the 0-jet ggH $p_{\mathrm{T}2} < 20\,\mathrm{GeV}$ (left) and $p_{\mathrm{T}2} > 20\,\mathrm{GeV}$ (right) DF categories. The uncertainty band corresponds to the total systematic uncertainty in the templates after the fit to the data. The signal template is shown both stacked on top of the backgrounds, as well as superimposed. The yields are shown with their best fit normalizations from the simultaneous fit. Vertical bars on data points represent the statistical uncertainty in the data. The overflow is included in the last bin. The lower panel in each figure shows the ratio of the number of events observed in data to that of the total SM MC as extracted from the fit

gories based on jet multiplicity. Instead, exactly two jets with $p_{\mathrm{T}} > 30\,\mathrm{GeV}$ and $m_{\mathrm{jj}} > 120\,\mathrm{GeV}$ are required, while still requiring the absence of b-tagged jets with $p_{\mathrm{T}} > 20\,\mathrm{GeV}$. In this category the DEEPFLAVOR tagger [32] is used. Finally, $60 < m_{\mathrm{T}}^{\mathrm{H}} < 125\,\mathrm{GeV}$ is required.

In order to separate the signal from the background, a DNN approach has been followed. The DNN is constructed to perform a multiclass classification of an event as either signal (VBF) or any of the three main background processes, namely: WW, top quark production, and ggH. As a result, a vector $\vec{o}$ of four numbers is attributed to an event. Each number represents the degree of agreement of the event with the signal and the three background processes. Each of these outputs can be interpreted as a probability, since they are normalized to one. Therefore, for a given event, the process j with the highest output o_j is interpreted as the most probable process. For this reason, the four outputs are referred to as classifiers: C_{VBF}, C_{t}, C_{WW}, and C_{ggH}. In the SR four orthogonal categories are made using the classifiers. If, for a given event, C_j is higher than the other three, the event is classified in the *j-like* category, and C_j is used as the discriminating variable. A shape-based analysis is hence performed

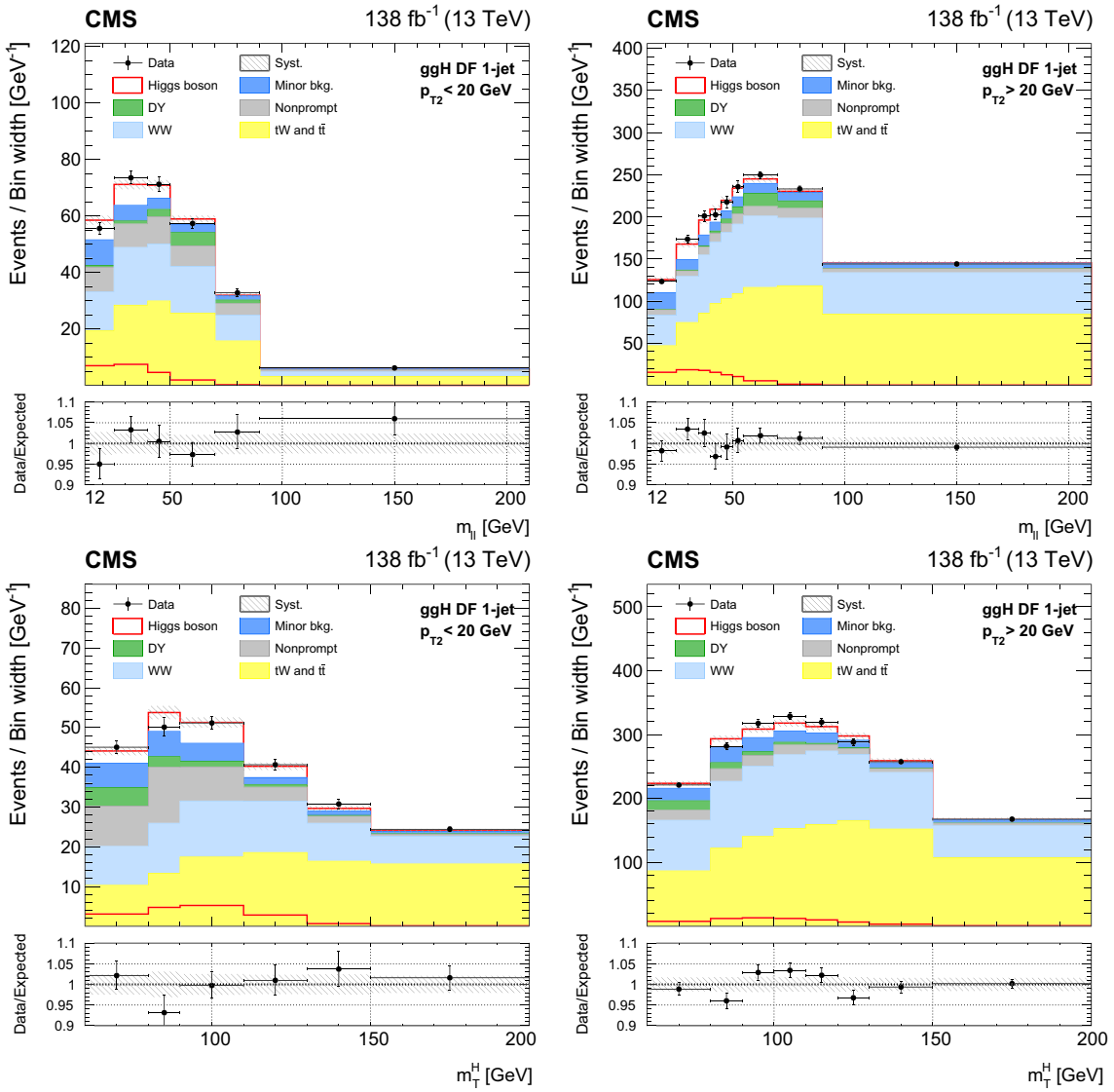


Fig. 2 Observed distributions of the $m_{\ell\ell}$ (upper) and $m_{\mathrm{T}}^{\mathrm{H}}$ (lower) fit variables in the 1-jet ggH $p_{\mathrm{T}2} < 20\,\mathrm{GeV}$ (left) and $p_{\mathrm{T}2} > 20\,\mathrm{GeV}$ (right) DF categories. A detailed description is given in the Fig. 1 caption

in these categories. The DNN is trained on a set of 26 input variables, including kinematic information from the dilepton system, $\vec{p}_{\mathrm{T}}^{\,\mathrm{miss}}$, and jets. The variables with the most discrimination power are found to be m_{jj}, $\Delta\eta_{\mathrm{jj}}$ and $m_{\ell\ell}$. As done in the DF ggH categories, in order to optimize background subtraction in the SR, two CRs are defined, enriched in $\tau\tau$ and top quark events, respectively. They are defined by the same selection as the SR, but inverting the b jet veto for the top quark CR and the $m_{\mathrm{T}}^{\mathrm{H}}$ requirement for the $\tau\tau$ CR. The full selection and categorization strategy is summarized in Table 5. Observed distributions for the C_{VBF} and C_{ggH} classifiers in the *VBF-like* and *ggH-like* categories respectively are shown in Fig. 10.

In order to verify that the simulated background processes agree with data in the DNN classifiers, the distributions are also checked at the level of the VBF SR global selection, i.e., before the further event categorization based on the classifier outputs. The C_{VBF} DNN output in the aforementioned global selection region is shown in Fig. 11.

6.2 Same-flavor VBF categories

On top of the common global selection, the same selection used in the SF ggH categories is applied. However, in this case, at least two jets with $p_{\mathrm{T}} > 30\,\mathrm{GeV}$ are required, with $m_{\mathrm{jj}} > 350\,\mathrm{GeV}$, while also rejecting events that contain any b-tagged jets with $p_{\mathrm{T}} > 20\,\mathrm{GeV}$. To define a Higgs-boson-enriched phase space, a selection on the DYMVA DNN is added. The DNN is trained and optimized separately in each category. Two background CRs help in constraining the normalization of the top quark and WW backgrounds. These CRs consist in regions of phase space orthogonal but as close as

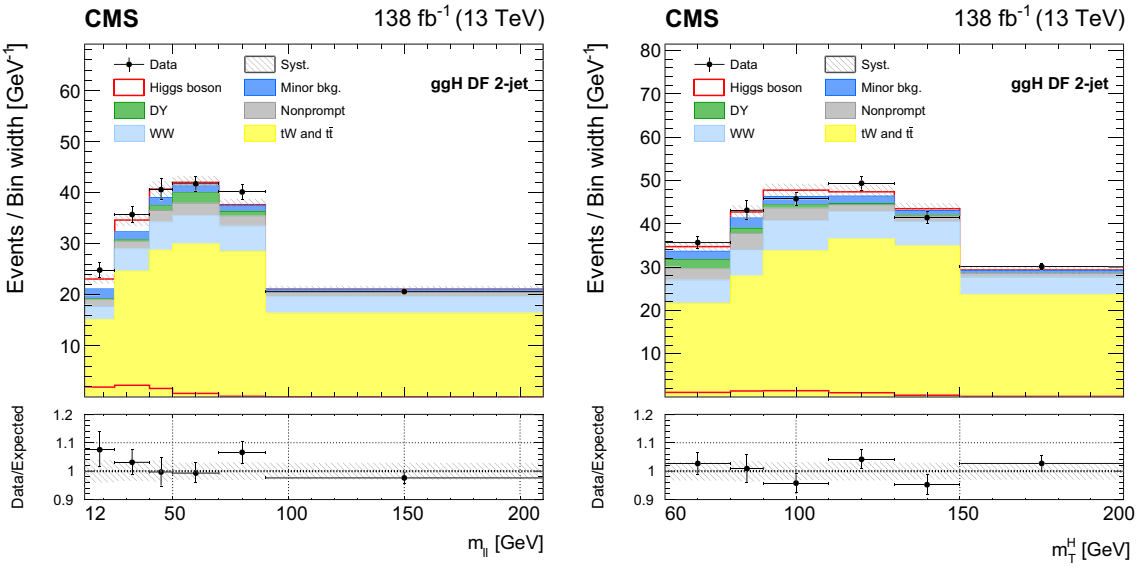


Fig. 3 Observed distributions of the $m_{\ell\ell}$ (left) and $m_{\mathrm{T}}^{\mathrm{H}}$ (right) fit variables in the 2-jet ggH DF category. A detailed description is given in the Fig. 1 caption

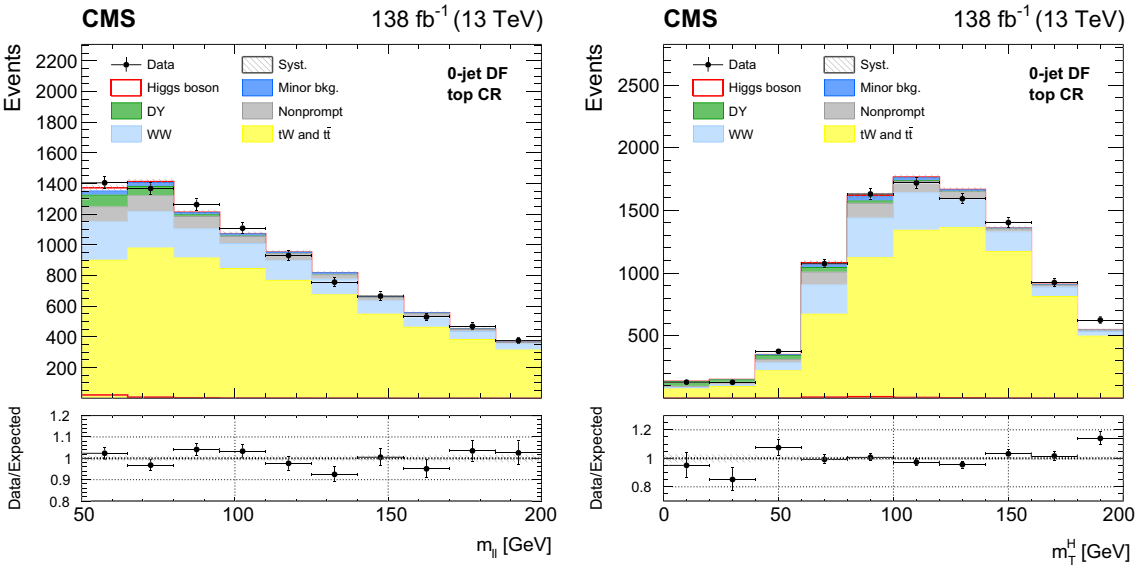


Fig. 4 Observed distributions of the $m_{\ell\ell}$ (left) and $m_{\mathrm{T}}^{\mathrm{H}}$ (right) variables in the 0-jet DF top quark control region. A detailed description is given in the Fig. 1 caption

possible to the signal phase space. This channel utilizes a simple counting experiment analysis, thus the event requirements are chosen to maximize the expected signal significance. The full selection and categorization strategy is summarized in Table 6.

7 Vector boson associated production categories

This section describes categories targeting the VH production mode. Four subcategories are defined (WHSS, WH3ℓ, ZH3ℓ, and ZH4ℓ) to target final states in which the vector boson V, produced in association with the Higgs boson, decays leptonically. Two more categories (VH 2j DF/SF) select events in which the V boson decays into two resolved jets. An additional selection is applied in each category to reduce the background, as well as an event categorization, defining phase spaces more sensitive to either signal or specific backgrounds. Details on the event selection and categorization are given below.

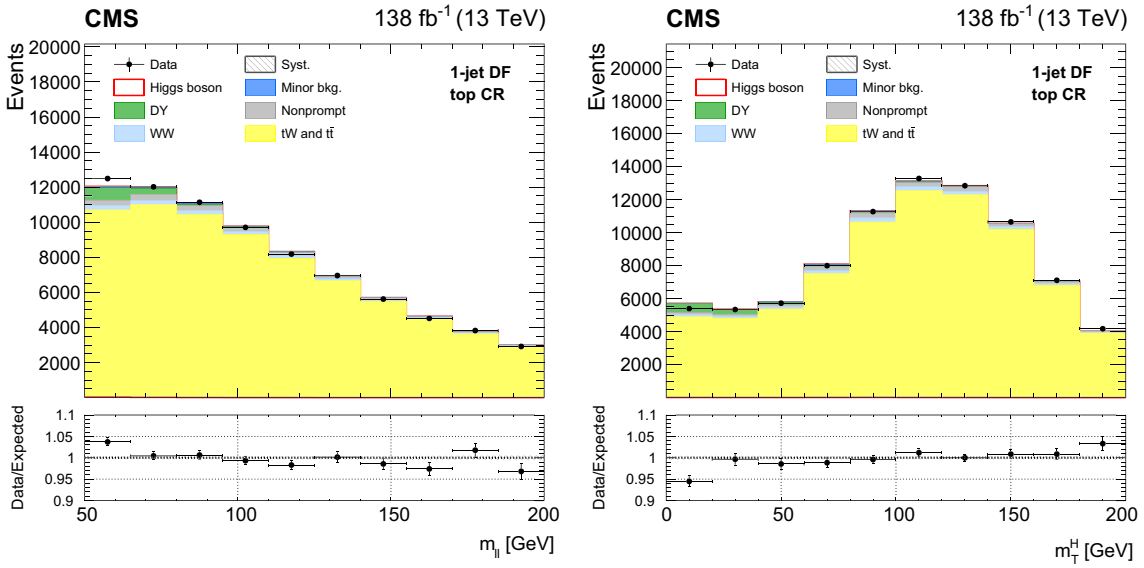


Fig. 5 Observed distributions of the $m_{\ell\ell}$ (left) and $m_{\mathrm{T}}^{\mathrm{H}}$ (right) variables in the 1-jet DF top quark control region. A detailed description is given in the Fig. 1 caption

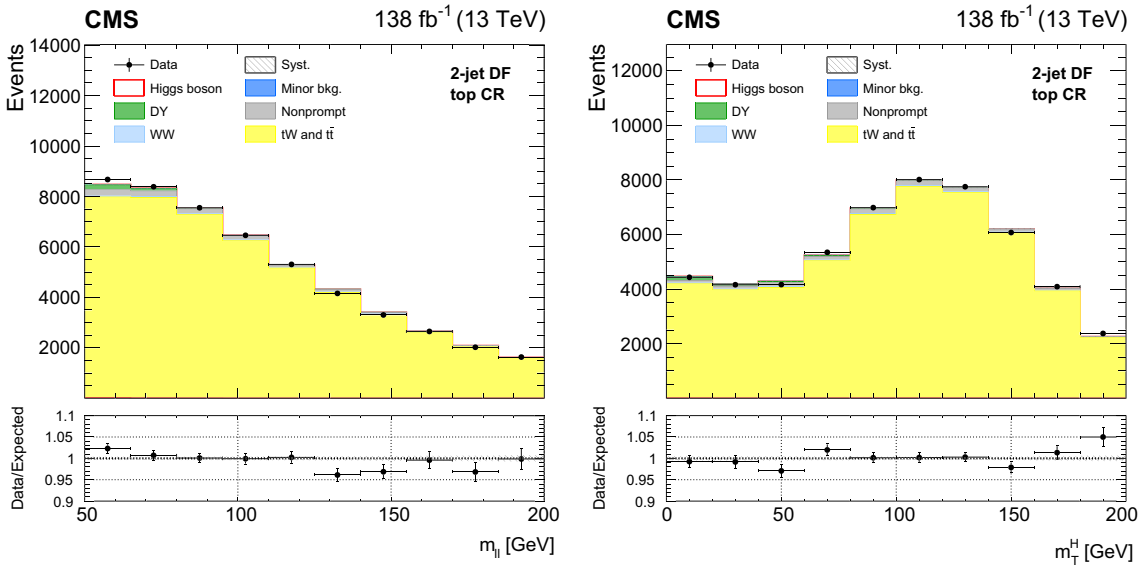


Fig. 6 Observed distributions of the $m_{\ell\ell}$ (left) and $m_{\mathrm{T}}^{\mathrm{H}}$ (right) variables in the 2-jet DF top quark control region. A detailed description is given in the Fig. 1 caption

7.1 WHSS categories

The WHSS category targets the WH $\rightarrow 2\ell 2\nu$qq final state, where the two charged leptons are required to have same sign to reduce DY background. Therefore, the final state contains two same-sign leptons, $p_{\mathrm{T}}^{\mathrm{miss}}$, and at least one jet. The analysis requires the leading (subleading) lepton to have $p_{\mathrm{T}} >$ 25 (20) GeV. To remove contributions from low-mass resonances, $m_{\ell\ell}$ is required to be greater than 12 GeV. The two leptons must have a pseudorapidity separation ($\Delta\eta_{\ell\ell}$) of less than two. Events are also required to have $p_{\mathrm{T}}^{\mathrm{miss}} > 30$ GeV, as well as no b-tagged jet with $p_{\mathrm{T}} > 20$ GeV.

Signal region events are further categorized based on the number of jets and the lepton flavor composition. Events in the 1-jet category are required to contain exactly one jet with $p_{\mathrm{T}} > 30$ GeV and $|\eta| < 4.7$. Events in the 2-jet category are required to contain at least two jets with the same kinematic constraints. For events containing more than two jets, only the two jets with highest p_{T} are considered for the analysis. These jets must have $m_{\mathrm{jj}} < 100$ GeV. The SRs are further divided into eμ and $\mu\mu$ categories. Events with two electrons

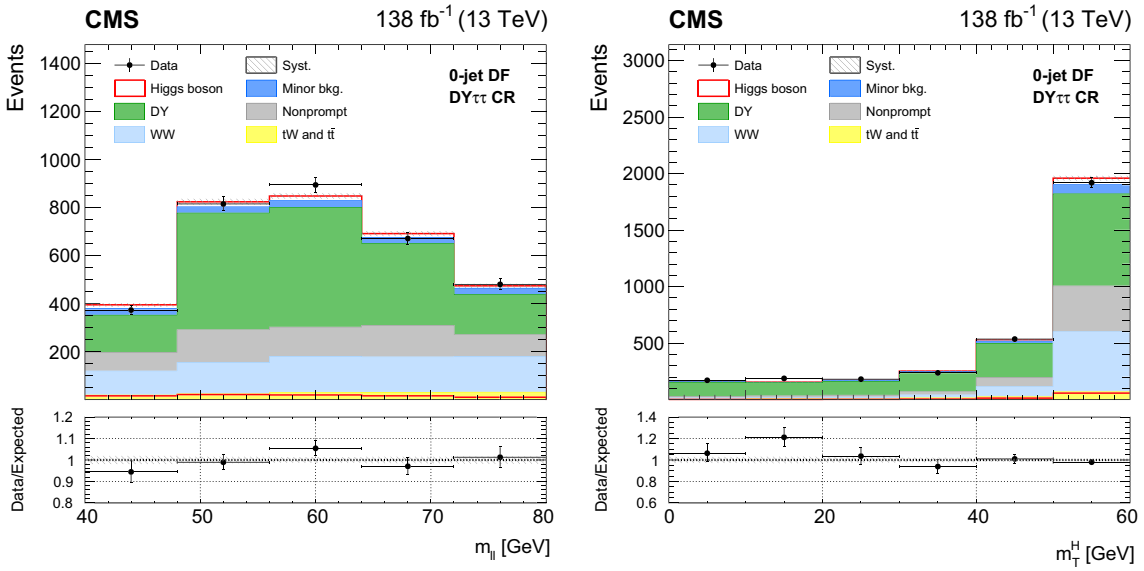


Fig. 7 Observed distributions of the $m_{\ell\ell}$ (left) and $m_{\mathrm{T}}^{\mathrm{H}}$ (right) variables in the 0-jet DF $\tau\tau$ control region. A detailed description is given in the Fig. 1 caption

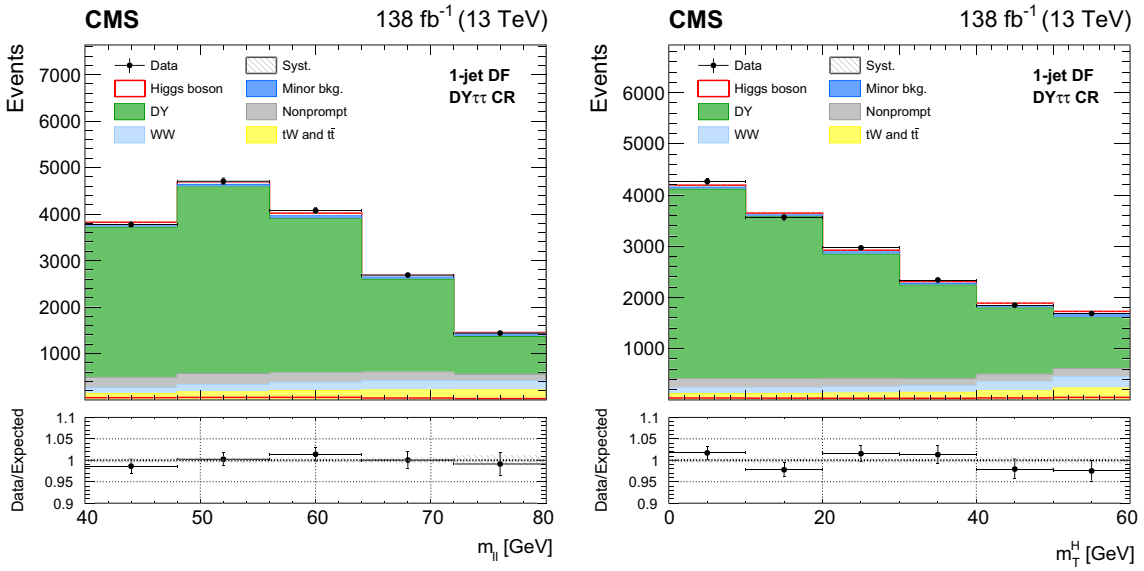


Fig. 8 Observed distributions of the $m_{\ell\ell}$ (left) and $m_{\mathrm{T}}^{\mathrm{H}}$ (right) variables in the 1-jet DF $\tau\tau$ control region. A detailed description is given in the Fig. 1 caption

are not considered, as this flavor category is less sensitive to signal.

To improve discrimination between signal and background, the variable $\widetilde{m}_{\mathrm{H}}$ is defined, which serves as a proxy for m_{H}. It is computed as the invariant mass of the dijet pair four-momentum $P_{\mathrm{jj}} = (E_{\mathrm{jj}}, \vec{p}_{\mathrm{jj}})$ and twice the four-momentum of the lepton closest to the dijet pair $P_{\ell} = (p_{\ell}, \vec{p}_{\ell})$:

$$\widetilde{m}_{\mathrm{H}} = \sqrt{(P_{jj} + 2P_{\ell})^2}. \quad (2)$$

The second lepton four-momentum serves as a proxy for the neutrino. If an event in the 1-jet category contains a second jet with $20 < p_{\mathrm{T}} < 30\,\mathrm{GeV}$, this jet is included in the computation of this variable; otherwise the four-momentum of the single jet is used. Events in all categories are required to have $\widetilde{m}_{\mathrm{H}} > 50\,\mathrm{GeV}$. A summary of the event selection is given in Table 7.

The main backgrounds in the WHSS category are WZ, W+jets, Vγ, and Vγ^* production. Additional backgrounds are top quark, triboson, WW, and ZZ production. The W+jets events pass the selection when a nonprompt lepton passes

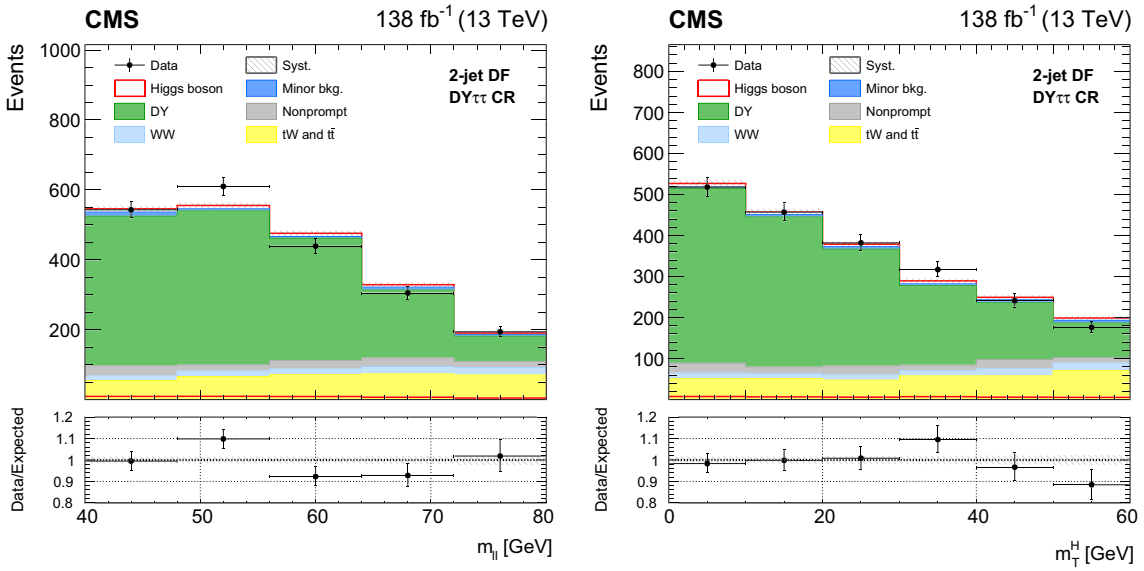


Fig. 9 Observed distributions of the $m_{\ell\ell}$ (left) and $m_{\mathrm{T}}^{\mathrm{H}}$ (right) variables in the 2-jet DF $\tau\tau$ control region. A detailed description is given in the Fig. 1 caption

the lepton selection. This nonprompt background is estimated from data, as described in Sect. 9. The remaining backgrounds are estimated using MC simulation. The WZ background normalization is estimated in the 1- and 2-jet CRs shared with the ZH3ℓ category, described in Sect. 7.3.

To extract the Higgs boson production cross section, a binned fit is performed to the $\widetilde{m}_{\mathrm{H}}$ variable. Figure 12 shows the $\widetilde{m}_{\mathrm{H}}$ distribution after the fit to the data.

7.2 WH3ℓ categories

The WH3ℓ category targets the WH $\rightarrow 3\ell 3\nu$ decay. The final state therefore contains three leptons and $p_{\mathrm{T}}^{\mathrm{miss}}$. The analysis selects events containing three leptons with $p_{\mathrm{T}} > 25$, 20, and 15 GeV, respectively and total charge ($\mathrm{Q}_{3\ell}$) ± 1. The invariant mass of any dilepton pair is required to be greater than 12 GeV to remove low-mass resonances. Events are rejected if they contain a jet with $p_{\mathrm{T}} > 30$ GeV, or any b-tagged jet with $p_{\mathrm{T}} > 20$ GeV.

Events in the SR are categorized based on the flavor composition of the lepton pairs. Events with at least one opposite-sign SF (OSSF) lepton pair are placed in the OSSF category, while all other events are placed in the same-sign SF (SSSF) category. To reject backgrounds containing Z bosons, events in the OSSF SR must pass a Z boson veto, where all lepton pairs must satisfy $|m_{\ell\ell} - m_{\mathrm{Z}}| > 20$ GeV, as well as $p_{\mathrm{T}}^{\mathrm{miss}} > 40$ GeV.

The main backgrounds in the WH3ℓ category are WZ, ZZ, Vγ, and Vγ^* production, as well as backgrounds containing nonprompt leptons. Nonprompt backgrounds are estimated from data, as described in Sect. 9. The remaining backgrounds are estimated from simulated samples. The WZ and Zγ backgrounds are normalized using dedicated CRs, matching the OSSF SR with the exception of an inverted Z boson veto, a differing $p_{\mathrm{T}}^{\mathrm{miss}}$ requirement, and an additional selection on the invariant mass of the full lepton system ($m_{3\ell}$). A summary of the event selection and categorization is given in Table 8.

To discriminate between signal and background, two BDTs, trained separately for the OSSF and SSSF categories, are used. The BDTs are built using the TMVA [70] package and trained on events passing the OSSF and SSSF SR selections without the $|m_{\ell\ell} - m_{\mathrm{Z}}|$ requirement. The number of input variables used in the BDT training is 19 and 15 in the OSSF and SSSF regions, respectively. They include kinematic information on the leptons, $\vec{p}_{\mathrm{T}}^{\,\mathrm{miss}}$, b tagging scores for the leading jets, and various invariant masses built from leptons and $\vec{p}_{\mathrm{T}}^{\,\mathrm{miss}}$, with the minimum invariant mass and ΔR separation of the opposite sign lepton pairs giving the most discrimination power. To extract the Higgs boson production cross section, a binned fit is performed to the BDT score. Figure 13 shows the BDT discriminant distributions after the fit to the data.

7.3 ZH3ℓ categories

The ZH3ℓ category targets the ZH $\rightarrow 3\ell\nu$qq decay. The final state therefore contains three leptons with total charge ± 1. The invariant mass of any dilepton pair is required to be greater than 12 GeV to reject low-mass resonances. The event must contain an OSSF lepton pair with invariant mass $|m_{\ell\ell} - m_{\mathrm{Z}}| < 25$ GeV. Events are rejected if any b-tagged jet

Table 4 Summary of the selection used in same-flavor ggH categories. The DYMVA threshold is optimized separately in each subcategory and data set

Subcategories	Selection
Global selection	
—	$p_{T1} > 25\,\text{GeV}$, $p_{T2} > 10\,\text{GeV}$ (2016) or 13 GeV
	$p_T^{miss} > 20\,\text{GeV}$, $p_T^{\ell\ell} > 30\,\text{GeV}$
	ee or $\mu\mu$ pair with opposite charge
	$m_{\ell\ell} > 12\,\text{GeV}$, $\lvert m_{\ell\ell} - m_Z \rvert > 15\,\text{GeV}$
0-jet ggH category	
ee, $\mu\mu$	$m_{\ell\ell} < 60\,\text{GeV}$, $m_T^H > 90\,\text{GeV}$, $\lvert \Delta\phi_{\ell\ell} \rvert < 2.3$
	No b-tagged jets with $p_T > 20\,\text{GeV}$
	DYMVA above threshold
WW CR	As SR but with $m_{\ell\ell} > 100\,\text{GeV}$
	$m_T^H > 60\,\text{GeV}$, $m_T(\ell_2, p_T^{miss}) > 30\,\text{GeV}$
Top quark CR	As SR but with $m_{\ell\ell} > 100\,\text{GeV}$, $m_T(\ell_2, p_T^{miss}) > 30\,\text{GeV}$
	At least one b-tagged jet with $20 < p_T < 30\,\text{GeV}$
1-jet ggH category	
ee, $\mu\mu$	$m_{\ell\ell} < 60\,\text{GeV}$, $m_T^H > 80\,\text{GeV}$, $\lvert \Delta\phi_{\ell\ell} \rvert < 2.3$
	No b-tagged jets with $p_T > 20\,\text{GeV}$
	DYMVA above threshold
WW CR	As SR but with $m_{\ell\ell} > 100\,\text{GeV}$
	$m_T^H > 60\,\text{GeV}$, $m_T(\ell_2, p_T^{miss}) > 30\,\text{GeV}$
Top quark CR	As SR but with $m_{\ell\ell} > 100\,\text{GeV}$, $m_T(\ell_2, p_T^{miss}) > 30\,\text{GeV}$
	At least one b-tagged jet with $p_T > 30\,\text{GeV}$
2-jet ggH category	
ee, $\mu\mu$	$m_{\ell\ell} < 60\,\text{GeV}$, $65 < m_T^H < 150\,\text{GeV}$
	No b-tagged jets with $p_T > 20\,\text{GeV}$
	DYMVA above threshold
WW CR	As SR but with $m_{\ell\ell} > 100\,\text{GeV}$
	$m_T^H > 60\,\text{GeV}$, $m_T(\ell_2, p_T^{miss}) > 30\,\text{GeV}$
Top quark CR	As SR but with $m_{\ell\ell} > 100\,\text{GeV}$, $m_T(\ell_2, p_T^{miss}) > 30\,\text{GeV}$
	At least one b-tagged jet with $p_T > 30\,\text{GeV}$

Table 5 Selection used in the different-flavor VBF categories

Subcategories	Selection
Global selection	
—	$p_{T1} > 25\,\text{GeV}$, $p_{T2} > 10\,\text{GeV}$ (2016) or 13 GeV
	$p_T^{miss} > 20\,\text{GeV}$, $p_T^{\ell\ell} > 30\,\text{GeV}$, $m_{\ell\ell} > 12\,\text{GeV}$
	eμ pair with opposite charge
2-jet VBF category	
SR	$60 < m_T^H < 125\,\text{GeV}$, $m_T(\ell_2, p_T^{miss}) > 30\,\text{GeV}$
	2 jets with $p_T > 30\,\text{GeV}$, $m_{jj} > 120\,\text{GeV}$
	No b-tagged jet with $p_T > 20\,\text{GeV}$
Top quark CR	As SR but with no m_T^H requirement, $m_{\ell\ell} > 50\,\text{GeV}$
	At least one b-tagged jet with $p_T > 30\,\text{GeV}$
$\tau\tau$ CR	As SR but with $m_T^H < 60\,\text{GeV}$
	$40 < m_{\ell\ell} < 80\,\text{GeV}$

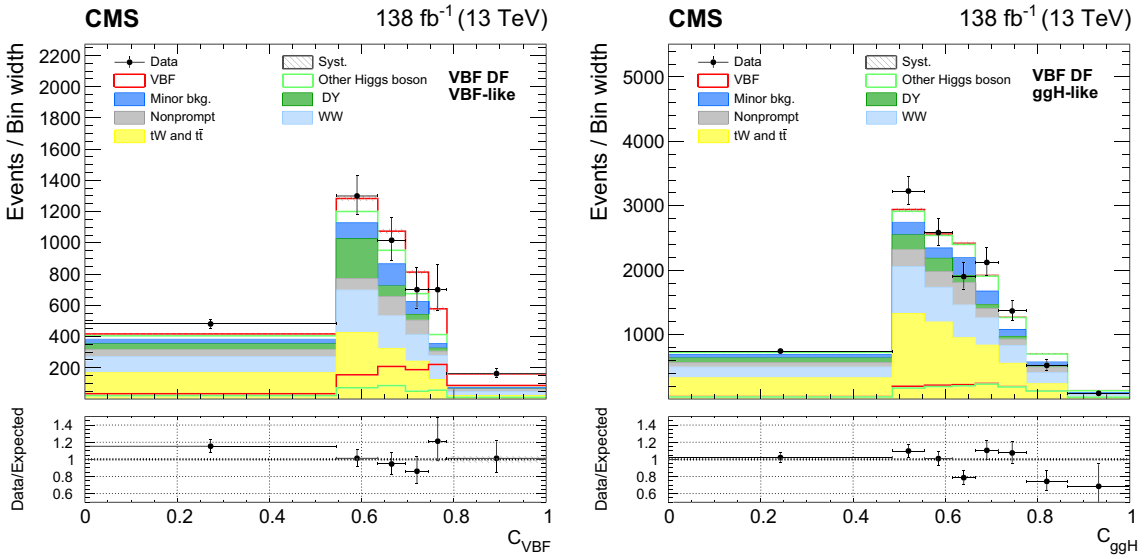


Fig. 10 Distributions for the C_{VBF} (left) and C_{ggH} (right) classifiers in the *VBF-like* and *ggH-like* VBF DF categories, respectively. A detailed description is given in the Fig. 1 caption

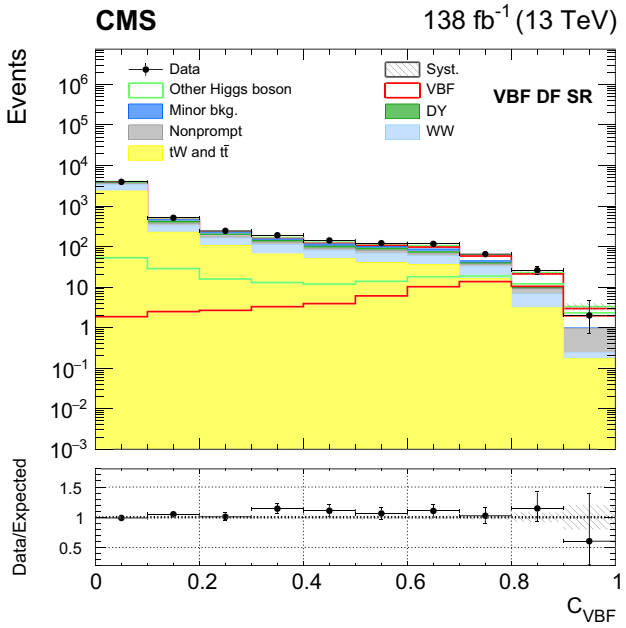


Fig. 11 Distribution of the C_{VBF} classifier in the VBF DF SR, before the further event categorization based on the classifier outputs. A detailed description is given in the Fig. 1 caption

with $p_{\mathrm{T}} > 20\,\mathrm{GeV}$ passing the medium WP of the tagging algorithm is found.

Events are categorized based on the number of jets. Events in the 1-jet category contain exactly one jet with $p_{\mathrm{T}} > 30\,\mathrm{GeV}$ and $|\eta| < 4.7$, while events in the 2-jet category contain at least two jets passing these requirements. Signal region events must also have an azimuthal separation between the two W bosons ($\Delta\phi(\ell p_{\mathrm{T}}^{\mathrm{miss}}, j(j))$), represented by the $\ell + p_{\mathrm{T}}^{\mathrm{miss}}$ and (di)jet systems respectively, below $\pi/2$, and pass a Z boson internal conversion veto $|m_{3\ell} - m_{\mathrm{Z}}| > 20\,\mathrm{GeV}$.

The main backgrounds in the ZH3ℓ analysis are WZ, ZZ, and Z+jets events. The Zγ/γ^*, VVV, and $\mathrm{t\bar{t}}$+jets processes also contribute. The Z+jets events pass the selection when a nonprompt lepton passes the lepton selection. This background is estimated from data as described in Sect. 9. The remaining backgrounds are modeled using MC simulation. The WZ normalization as a function of the number of jets is extracted from dedicated CRs, which are categorized by the number of jets in the same way as the SRs. The WZ CRs are also used to constrain the WZ background in the WHSS category. A summary of the event selection and categorization is shown in Table 9.

To extract the Higgs boson production cross section, a binned fit is performed to the $m_{\mathrm{T}}^{\mathrm{H}} = m_{\mathrm{T}}(\ell p_{\mathrm{T}}^{\mathrm{miss}}, j(j))$ variable, defined in Eq. (1). Figure 14 shows the $m_{\mathrm{T}}^{\mathrm{H}}$ distributions after the fit to the data.

7.4 ZH4ℓ categories

The ZH4ℓ category targets the $\mathrm{ZH} \to 4\ell 2\nu$ decay. The final state therefore contains four leptons and $p_{\mathrm{T}}^{\mathrm{miss}}$. The analysis selects events containing four leptons with $p_{\mathrm{T}} > 25$, 15, 10, and 10 GeV, respectively, and null total charge ($\mathrm{Q}_{4\ell}$). The invariant mass of any dilepton pair is required to be greater than 12 GeV to reject low-mass resonances. The opposite-sign SF lepton pair with $m_{\ell\ell}$ closest to m_{Z} is designated as the Z boson candidate, while the remaining lepton pair is referred to as the X candidate. The Z boson candidate mass

Table 6 Selection used in the same-flavor VBF categories. The DYMVA threshold is optimized separately in each subcategory and data set

Subcategories	Selection
Global selection	
—	$p_{T1} > 25\,\text{GeV}$, $p_{T2} > 10\,\text{GeV}$ (2016) or 13 GeV
	$p_T^{miss} > 20\,\text{GeV}$, $p_T^{\ell\ell} > 30\,\text{GeV}$
	ee or $\mu\mu$ pair with opposite charge
	$m_{\ell\ell} > 12\,\text{GeV}$, $\lvert m_{\ell\ell} - m_Z \rvert > 15\,\text{GeV}$
2-jet VBF category	
ee, $\mu\mu$	$m_{\ell\ell} < 60\,\text{GeV}$, $65 < m_T^H < 150\,\text{GeV}$
	At least 2 jets with $p_T > 30\,\text{GeV}$
	$\lvert \Delta\phi_{\ell\ell} \rvert < 1.6$, $m_{jj} > 350\,\text{GeV}$
	No b-tagged jets with $p_T > 20\,\text{GeV}$
	DYMVA above threshold
WW CR	As SR but with $m_{\ell\ell} > 100\,\text{GeV}$
	$m_T^H > 60\,\text{GeV}$, $m_T(\ell_2, p_T^{miss}) > 30\,\text{GeV}$
Top quark CR	As SR but with $m_{\ell\ell} > 100\,\text{GeV}$, $m_T(\ell_2, p_T^{miss}) > 30\,\text{GeV}$
	At least one of the leading jets b-tagged

Table 7 Event selection and categorization in the WHSS category

Subcategories	Selection
Global selection	
—	$p_{T1} > 25\,\text{GeV}$, $p_{T2} > 20\,\text{GeV}$
	$m_{\ell\ell} > 12\,\text{GeV}$, $\lvert \Delta\eta_{\ell\ell} \rvert < 2$, $p_T^{miss} > 30\,\text{GeV}$
	$\widetilde{m}_H > 50\,\text{GeV}$, no b-tagged jet with $p_T > 20\,\text{GeV}$
Signal region	
1-jet e$\mu(\mu\mu)$	One jet with $p_T > 30\,\text{GeV}$
	e$\mu(\mu\mu)$ pair with same charge
2-jet e$\mu(\mu\mu)$	At least two jets with $p_T > 30\,\text{GeV}$, $m_{jj} < 100\,\text{GeV}$
	e$\mu(\mu\mu)$ pair with same charge
Control region	
WZ	Shared with ZH3ℓ

is required to be within 15 GeV of m_Z. Events are rejected if they contain any b-tagged jet with $p_T > 20\,\text{GeV}$.

Events are categorized based on the flavor of the lepton pair forming the X candidate. Events in the XSF category have an SF X lepton pair, while events in the XDF category have a DF X lepton pair. In the XSF category, events are required to satisfy $m_{4\ell} > 140\,\text{GeV}$, $10 < m_{\ell\ell}^X < 60\,\text{GeV}$, and $p_T^{miss} > 35\,\text{GeV}$. Events in the XDF category must have $10 < m_{\ell\ell}^X < 70\,\text{GeV}$ and $p_T^{miss} > 20\,\text{GeV}$.

Production of ZZ pairs is the main background in this category. Additional contributions arise from $t\bar{t}Z$, VVV, and Vγ processes. These backgrounds are all modeled with MC simulation. The ZZ normalization is extracted from data in a dedicated CR defined by the requirements $75 < m_{\ell\ell}^X < 105\,\text{GeV}$ and $p_T^{miss} < 35\,\text{GeV}$. The event selection and categorization in the ZH4ℓ category is summarized in Table 10.

A BDT approach is used to discriminate between signal and background. The BDT is trained on events passing the global selection, with $p_T^{miss} > 20\,\text{GeV}$ and $10 < m_{\ell\ell}^X < 70\,\text{GeV}$. The number of inputs used in the BDT is eight, and these include separation in the η-ϕ plane between the leptons in each dilepton pair, transverse masses of combinations of leptons and $\vec{p}_T^{miss}$, as well as p_T^{miss} itself. The kinematic variables of the X candidate give the most discriminating power, along with p_T^{miss}. To extract the Higgs boson cross section, a binned fit is performed on the BDT score. Figure 15 shows the BDT score distributions after the fit to the data.

7.5 Different-flavor VH2j categories

This category targets VH events in which the vector boson decays into two resolved jets and the Higgs boson decays to an eμ pair and neutrinos. The final state, and therefore the selection, is analogous to that of the ggH DF 2-jet category, with the added requirement that the dijet invariant mass be close to that of the W and Z bosons.

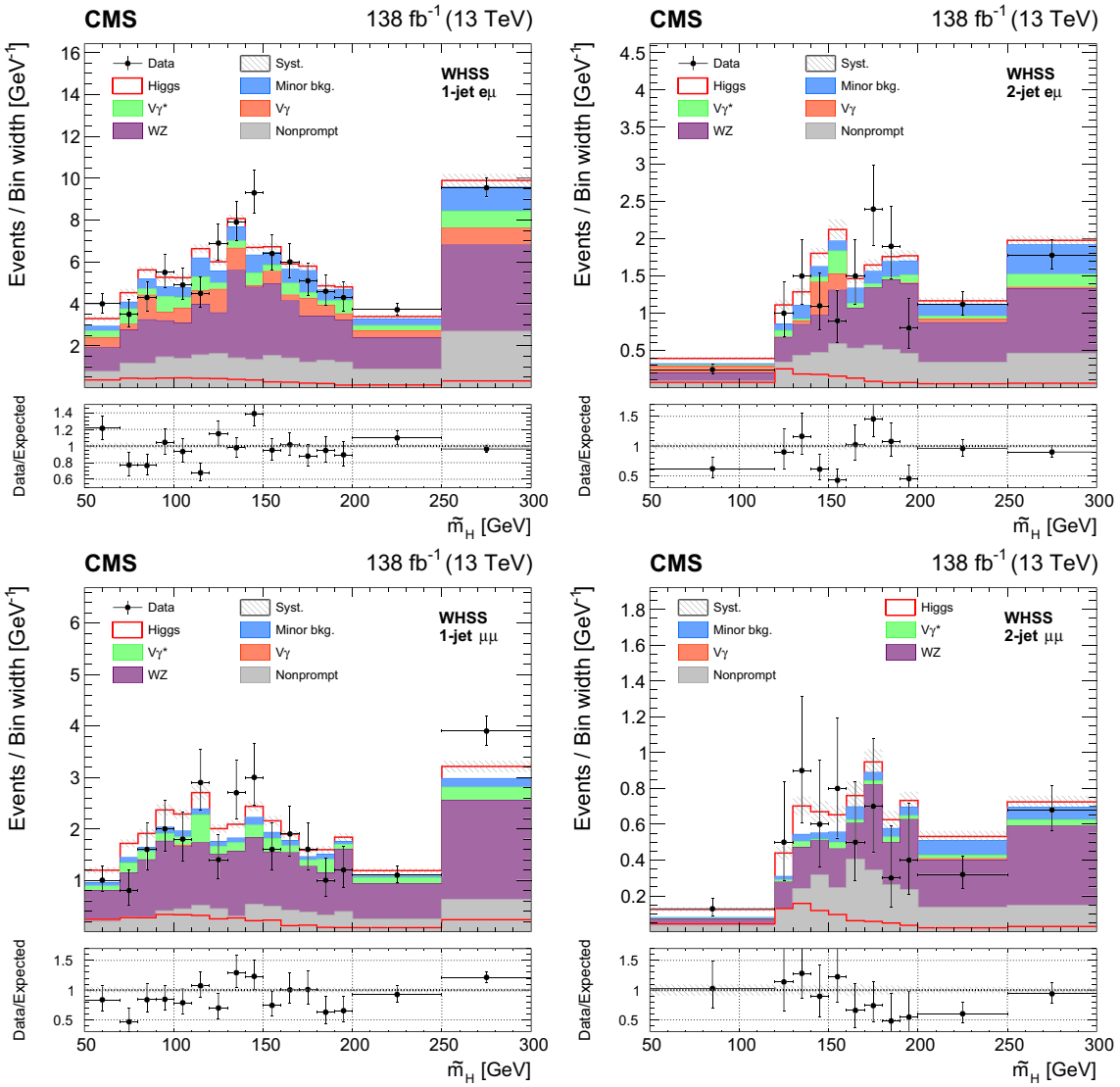


Fig. 12 Observed distributions of the $\widetilde{m}_{\mathrm{H}}$ fit variable in the WHSS 1-jet eμ (upper left), 2-jet eμ (upper right), 1-jet $\mu\mu$ (lower left), and 2-jet $\mu\mu$ (lower right) SRs. A detailed description is given in the Fig. 1 caption

Table 8 Event selection and categorization in the WH3ℓ category

Subcategories	Selection
Global selection	
—	$p_{\mathrm{T}1} > 25\,\mathrm{GeV}$, $p_{\mathrm{T}2} > 20\,\mathrm{GeV}$, $p_{\mathrm{T}3} > 15\,\mathrm{GeV}$
	$\mathrm{Q}_{3\ell} = \pm 1$, $\min(m_{\ell\ell}) > 12\,\mathrm{GeV}$, $\Delta\eta_{\ell\ell} > 2.0$
	$p_{\mathrm{T}}^{\mathrm{miss}} > 30\,\mathrm{GeV}$, $\widetilde{m}_{\mathrm{H}} > 50\,\mathrm{GeV}$
	No jets with $p_{\mathrm{T}} > 30\,\mathrm{GeV}$, no b-tagged jet with $p_{\mathrm{T}} > 20\,\mathrm{GeV}$
Signal region	
OSSF	OSSF lepton pair, $\lvert m_{\ell\ell} - m_{\mathrm{Z}}\rvert > 20\,\mathrm{GeV}$, $p_{\mathrm{T}}^{\mathrm{miss}} > 40\,\mathrm{GeV}$
SSSF	No OSSF lepton pair
Control region	
WZ	OSSF lepton pair, $\lvert m_{\ell\ell} - m_{\mathrm{Z}}\rvert < 20\,\mathrm{GeV}$
	$p_{\mathrm{T}}^{\mathrm{miss}} > 45\,\mathrm{GeV}$, $m_{3\ell} > 100\,\mathrm{GeV}$
Zγ	OSSF lepton pair, $\lvert m_{\ell\ell} - m_{\mathrm{Z}}\rvert < 20\,\mathrm{GeV}$
	$p_{\mathrm{T}}^{\mathrm{miss}} < 40\,\mathrm{GeV}$, $80 < m_{3\ell} < 100\,\mathrm{GeV}$

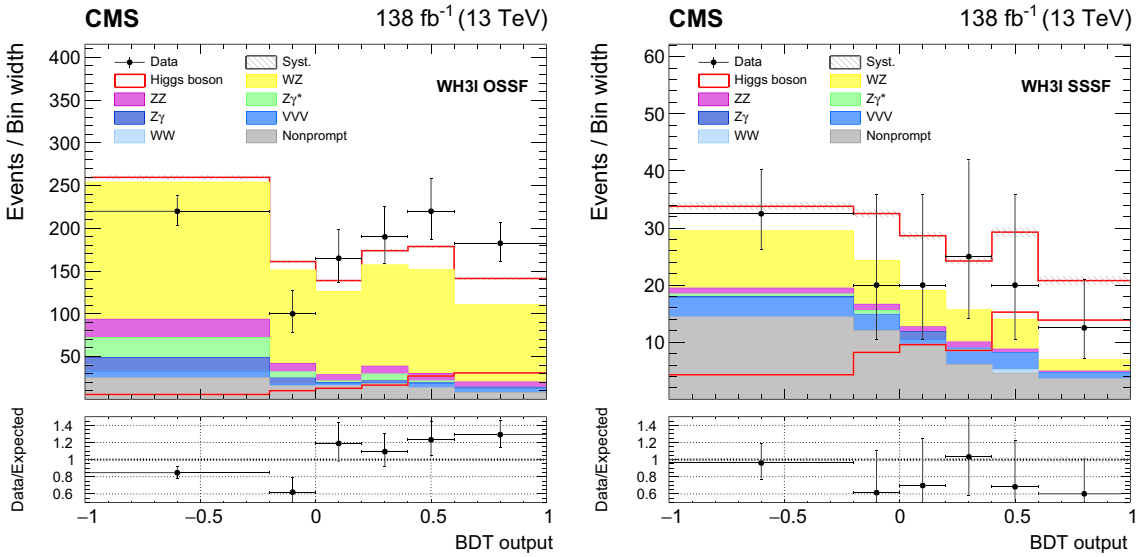


Fig. 13 Observed distributions of the BDT score in the WH3ℓ OSSF (left) and SSSF (right) SRs. A detailed description is given in the Fig. 1 caption

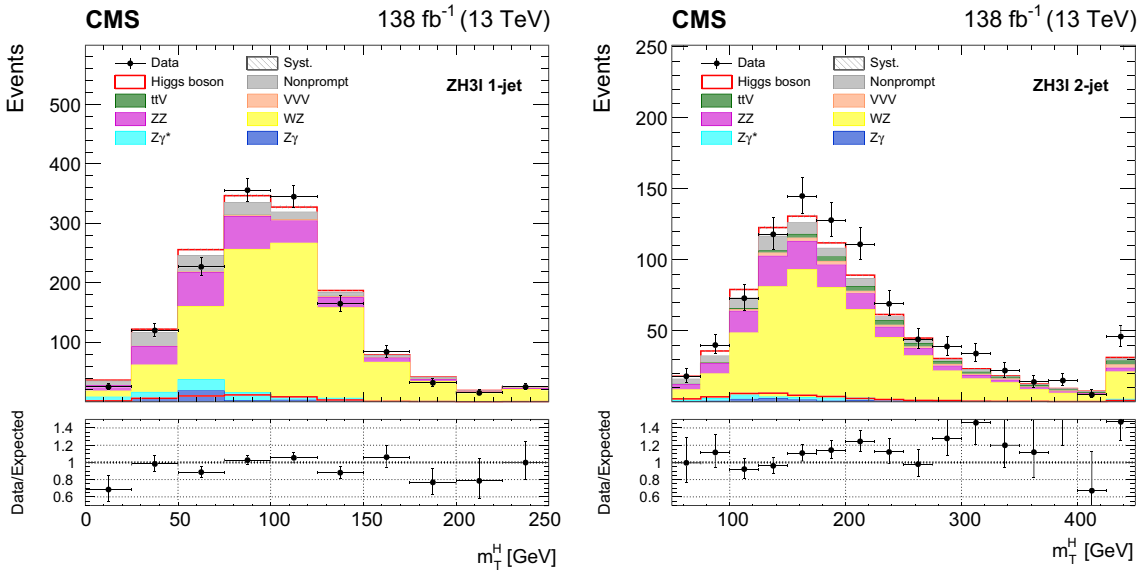


Fig. 14 Observed distributions of the $m_{\mathrm{T}}^{\mathrm{H}}$ fit variable in the ZH3ℓ 1-jet (left) and 2-jet (right) SRs. A detailed description is given in the Fig. 1 caption

The main backgrounds in this category are top quark and nonresonant WW pair production, as well as $\tau\tau$ pair production. The top quark and $\tau\tau$ backgrounds are normalized to the data in dedicated CRs. The full selection is summarized in Table 11. The VH production is found to contribute about 30% of the total signal in the VH2j DF SR.

The signal extraction fit is performed on a binned template shape of $m_{\ell\ell}$, which has a different profile for the signal and the nonresonant WW background. The distribution of $m_{\ell\ell}$ after the fit to the data is shown in Fig. 16.

7.6 Same-flavor VH2j categories

This category targets VH events in which the vector boson decays into two jets and the Higgs boson decays to either an ee or a $\mu\mu$ pair and neutrinos. The selection is identical to the 2-jet ggH SF categories described in Sect. 5.2 and Table 4, with the following modifications: the additional requirement $65 < m_{\mathrm{jj}} < 105$ GeV is imposed, the $m_{\ell\ell}$ threshold is moved to 70 GeV, a selection on $m_{\mathrm{T}}^{\mathrm{H}} < 150$ GeV is added, and the angle between the two leptons in the transverse plane ($\Delta\phi_{\ell\ell}$) is required to be less than 1.6. The threshold on the DYMVA

Table 9 Event selection and categorization in the ZH3ℓ category

Subcategories	Selection
Global selection	
—	$p_{T1} > 25\,\text{GeV}$, $p_{T2} > 20\,\text{GeV}$, $p_{T3} > 15\,\text{GeV}$
	$Q_{3\ell} = \pm 1$, $\min(m_{\ell\ell}) > 12\,\text{GeV}$
	$\lvert m_{\ell\ell} - m_Z \rvert < 25\,\text{GeV}$, $\lvert m_{3\ell} - m_Z \rvert > 20\,\text{GeV}$
	No b-tagged jet with $p_T > 20\,\text{GeV}$
Signal region	
1-jet	=1 jet with $p_T > 30\,\text{GeV}$, $\Delta\phi(\ell p_T^{\text{miss}}, j(j)) < \pi/2$
2-jet	≥2 jets with $p_T > 30\,\text{GeV}$, $\Delta\phi(\ell p_T^{\text{miss}}, j(j)) < \pi/2$
Control region	
1-jet WZ	=1 jet with $p_T > 30\,\text{GeV}$, $\Delta\phi(\ell p_T^{\text{miss}}, j(j)) > \pi/2$
2-jet WZ	≥2 jets with $p_T > 30\,\text{GeV}$, $\Delta\phi(\ell p_T^{\text{miss}}, j(j)) > \pi/2$

Table 10 Event selection and categorization in the ZH4ℓ category

Subcategories	Selection
Global selection	
—	$p_{T1} > 25\,\text{GeV}$, $p_{T2} > 15\,\text{GeV}$, $p_{T3} > 10\,\text{GeV}$, $p_{T4} > 10\,\text{GeV}$
	$Q_{4\ell} = 0$, $\min(m_{\ell\ell}) > 12\,\text{GeV}$, $\lvert m_{\ell\ell} - m_Z \rvert < 15\,\text{GeV}$
	No b-tagged jet with $p_T > 20\,\text{GeV}$
Signal region	
XSF	Same-flavor X pair, $m_{4\ell} > 140\,\text{GeV}$
	$10 < m_{\ell\ell}^X < 60\,\text{GeV}$, $p_T^{\text{miss}} > 35\,\text{GeV}$
XDF	Different-flavor X pair, $10 < m_{\ell\ell}^X < 70\,\text{GeV}$
	$p_T^{\text{miss}} > 20\,\text{GeV}$
Control region	
ZZ	$75 < m_{\ell\ell}^X < 105\,\text{GeV}$, $p_T^{\text{miss}} < 35\,\text{GeV}$

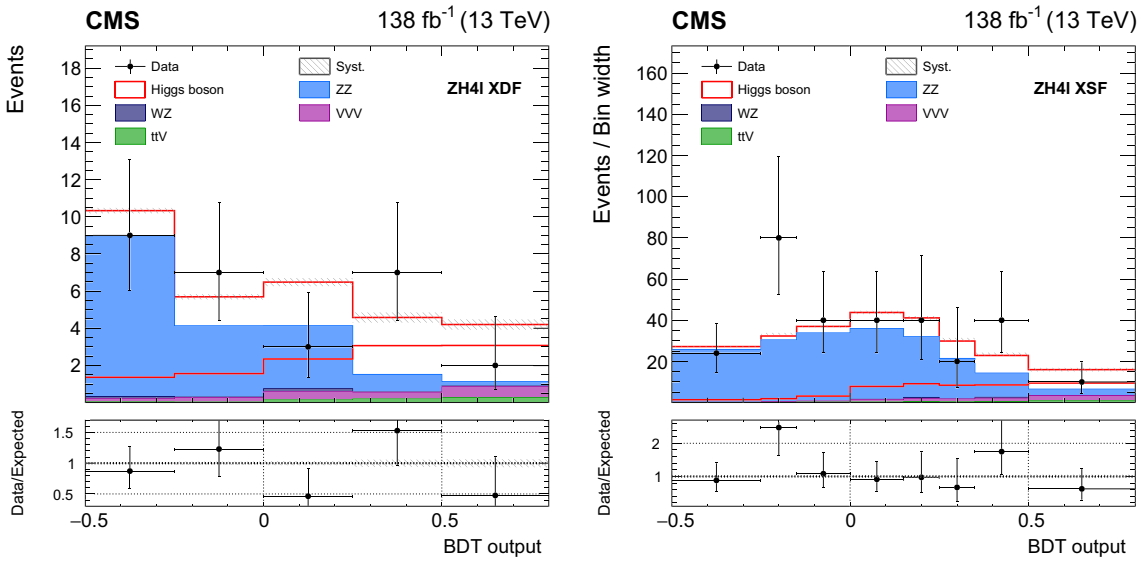


Fig. 15 Observed distributions of the BDT score in the ZH4ℓXDF (left) and XSF (right) SRs. A detailed description is given in the Fig. 1 caption

is tuned to achieve the highest signal-to-background ratio. The signal is extracted via a simultaneous fit to the number of events in each category.

8 The STXS measurement

Together with inclusive production cross sections, differential cross section measurements are also presented. These are performed within the STXS framework, using Stage 1.2 definitions [55]. In the STXS framework, the cross sections of different Higgs boson production mechanisms are measured in mutually exclusive regions of generator-level phase space, referred to as STXS bins, designed to enhance sensitivity to possible deviations from the SM. The full set of Stage 1.2 STXS bins is given in Fig. 17. The selections used in the STXS measurement match the ones described in the previous section, and the measurement is carried out by defining a set of analysis categories that target each STXS bin, as summarized in Fig. 18. The same CR setup as described in the previous section is maintained, and each CR is then subdivided to match the STXS categorization shown in Fig. 18. In all cases, the number of events is used as a fit variable in CRs. Results are then unfolded to the generator level, with the contribution from each STXS bin to each analysis category estimated from MC simulation, as shown in Fig. 19. Given the statistical power of the present data set, sensitivity to some of the Stage 1.2 bins is limited. Some bins are therefore measured together, by fixing the corresponding cross section ratios to the value predicted by the SM. We refer to this procedure as bin merging. Some STXS bins have been excluded, given the very low sensitivity. Groups of STXS bins merged with this procedure are highlighted in Fig. 17.

In the DF ggH and VBF categories, the discriminants of the same DNN explained in Sect. 6 are used for the categories which are common between VBF and ggH ($m_{\mathrm{jj}} > 350\,\mathrm{GeV}$ and $p_{\mathrm{T}}^{\mathrm{H}} < 200\,\mathrm{GeV}$), and in the category exclusive to the VBF ($m_{\mathrm{jj}} > 350\,\mathrm{GeV}$ and $p_{\mathrm{T}} > 200\,\mathrm{GeV}$). The signal extraction fit is performed on the two-dimensional ($m_{\ell\ell}$, m_{jj}) template in the VH2j DF category ($60 < m_{\mathrm{jj}} < 120\,\mathrm{GeV}$), while either $m_{\ell\ell}$ or ($m_{\ell\ell}$, $m_{\mathrm{T}}^{\mathrm{H}}$) templates are used in the remaining DF categories, depending on the number of expected events in each. In the same flavor categories a similar approach is followed, but only the number of events is used for the fit.

In the VH categories with a leptonic decay of the V boson, to extract the cross section as a function of the vector boson p_{T}, events are categorized into corresponding regions of reconstructed vector boson p_{T}. The reconstructed vector boson p_{T} is defined differently depending on the vector boson type and decay channel. Because in the WHSS and WH3ℓ categories the W boson p_{T} ($\vec{p}_{\mathrm{T}}^{\,\mathrm{W}}$) cannot be fully reconstructed due to the unobserved neutrino, proxies are defined

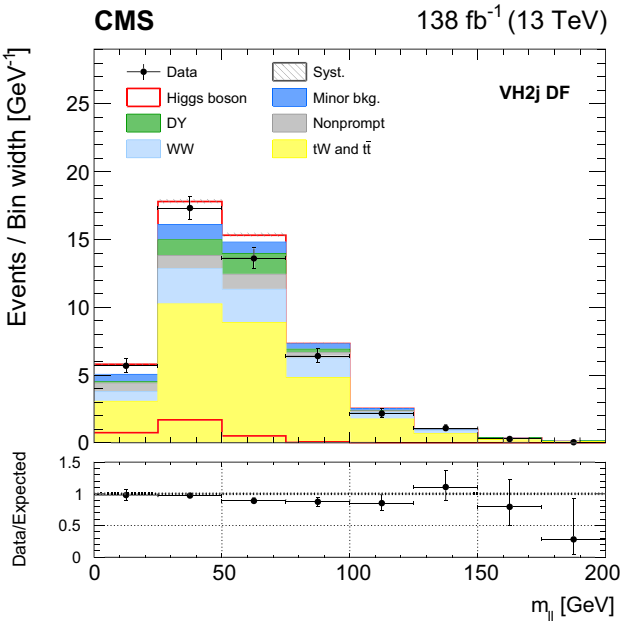


Fig. 16 Observed distribution of the $m_{\ell\ell}$ fit variable in the VH2j DF SR. A detailed description is given in the Fig. 1 caption

in both cases. In the WHSS category, the four-momenta of the lepton and neutrino from the associated W boson decay can be designated ℓ_{W} and ν_{W}, while the four-momenta of the lepton and neutrino from the Higgs boson decay can be designated ℓ_{H} and ν_{H}. The lepton from the W boson decay is identified as the one with the largest azimuthal separation from the jet or dijet. The transverse momentum of the W boson is defined as $\vec{\ell}_{\mathrm{W,T}} + \vec{\nu}_{\mathrm{W,T}}$, where $\vec{\nu}_{\mathrm{W}}$ is defined as:

$$\vec{\nu}_{\mathrm{W,T}} = \vec{p}_{\mathrm{T}}^{\,\mathrm{miss}} - \vec{\nu}_{\mathrm{H,T}} = \vec{p}_{\mathrm{T}}^{\,\mathrm{miss}} - \vec{\ell}_{\mathrm{H,T}} \left(\frac{125\,\mathrm{GeV}}{|\vec{\ell}_{\mathrm{H}} + \vec{j}j|} - 1 \right) \quad (3)$$

for events with two jets, or $\vec{p}_{\mathrm{T}}^{\,\mathrm{miss}} - \vec{\ell}_{\mathrm{H,T}}$ for events with fewer than two jets. Here $\vec{j}j$ indicates the dijet momentum. In the WH3ℓ category, $\vec{p}_{\mathrm{T}}^{\,\mathrm{W}}$ is difficult to resolve given the ambiguities from the three neutrinos in the final state. Instead, $p_{\mathrm{T}}(\ell_{\mathrm{W}})$ is used as a proxy for the W boson p_{T} in the WH3ℓ category. Here, ℓ_{W} is defined as the lepton pointing away from the opposite-sign dilepton pair with smallest angular separation ΔR. In the ZH3ℓ and ZH4ℓ categories, the reconstructed Z boson p_{T} ($\vec{p}_{\mathrm{T}}^{\,\mathrm{Z}}$) is defined as the p_{T} of the OSSF dilepton pair with $m_{\ell\ell}$ closest to m_{Z}. The variables used in the fit are the same as described in Sect. 7.

A summary of the expected signal fraction of the considered STXS signal processes in each category is shown in Fig. 20, together with the total number of expected $\mathrm{H} \rightarrow \mathrm{WW}$ signal events.

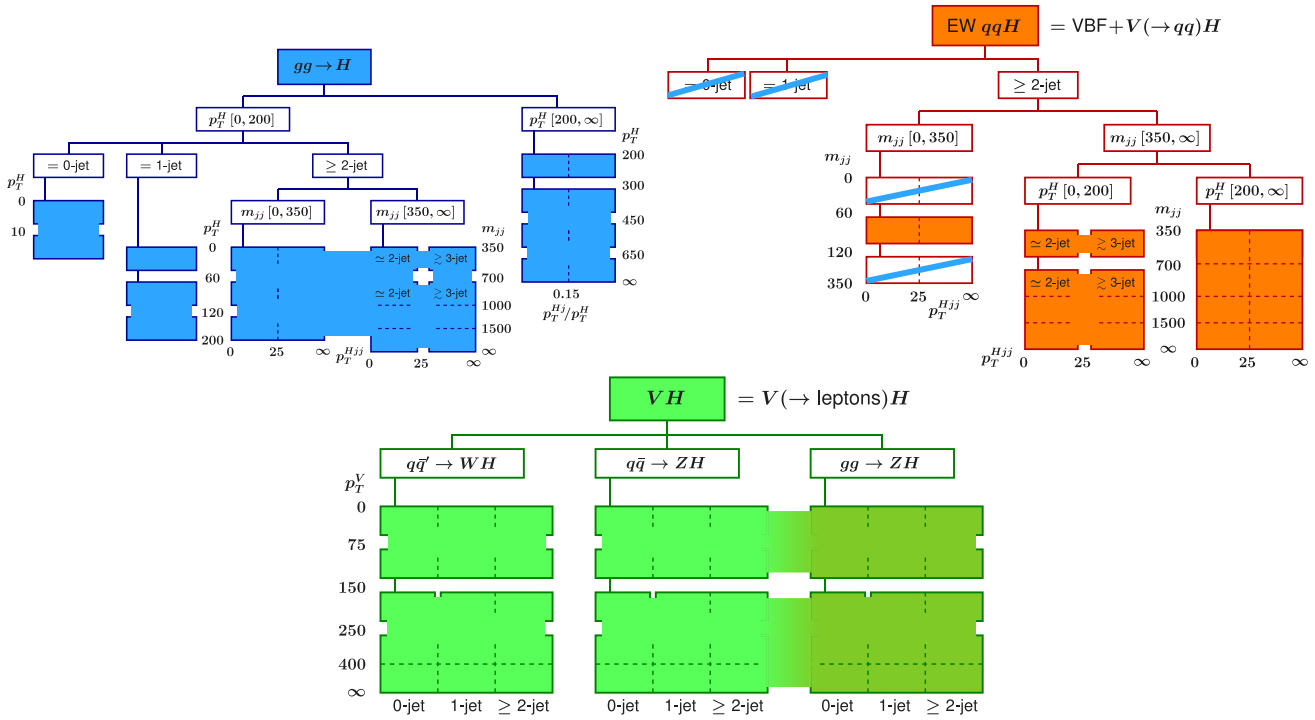


Fig. 17 The STXS Stage 1.2 binning scheme. Each rectangle corresponds to one of the STXS Stage 1.2 bins. Dashed lines indicate a possible finer splitting of some of the bins (not used in this analysis). Bins fused together with solid colors are merged in the analysis, i.e., they are measured as a single bin. Crossed-out bins are not measured

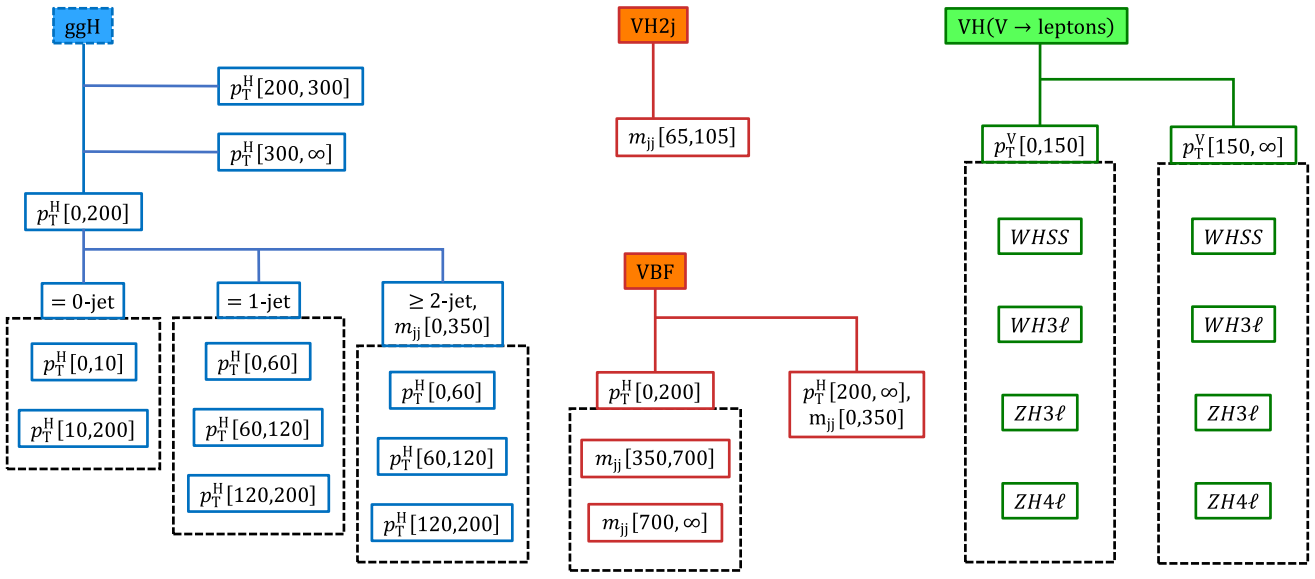


Fig. 18 Analysis categories for the STXS measurement. The baseline ggH, VBF, and VH selections are identical to what was described in Sects. 5–7. All dimensional quantities are measured in GeV

Table 11 Summary of the selection applied to different-flavor VH2j categories

Subcategory	Selection
Global selection	
—	$p_{T1} > 25$ GeV, $p_{T2} > 10$ GeV (2016) or 13 GeV
	$p_T^{miss} > 20$ GeV, $p_T^{\ell\ell} > 30$ GeV, $m_{\ell\ell} > 12$ GeV
	eμ pair with opposite charge
Signal region	
—	At least 2 jets with $p_T > 30$ GeV, $\lvert\eta_{j1}\rvert, \lvert\eta_{j2}\rvert < 2.5$
	$\Delta\eta_{jj} < 3.5$, $65 < m_{jj} < 105$ GeV
	$60\,\text{GeV} < m_T^H < 125\,\text{GeV}$, $\Delta R_{\ell\ell} < 2$
	No b-tagged jet with $p_T > 20$ GeV
Control region	
Top quark CR	As SR but with no m_T^H requirement, $m_{\ell\ell} > 50$ GeV
	At least 1 b-tagged jet with $p_T > 30$ GeV
ττ CR	As signal region but with $m_T^H < 60$ GeV
	$40 < m_{\ell\ell} < 80$ GeV

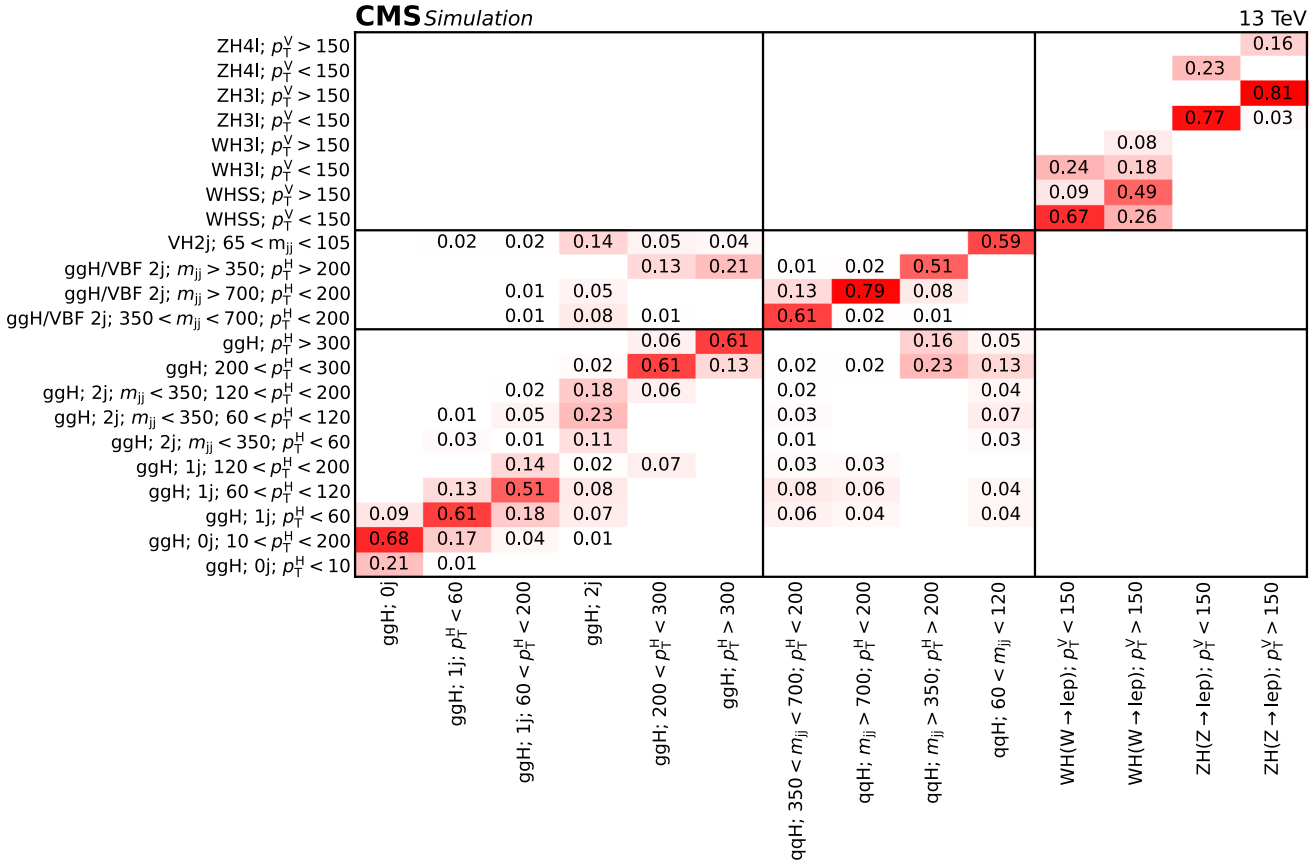


Fig. 19 Expected signal composition in each STXS bin. Generator-level bins are reported in the horizontal axis, and the corresponding analysis categories on the vertical axis. All quantities in the definitions of bins are measured in GeV

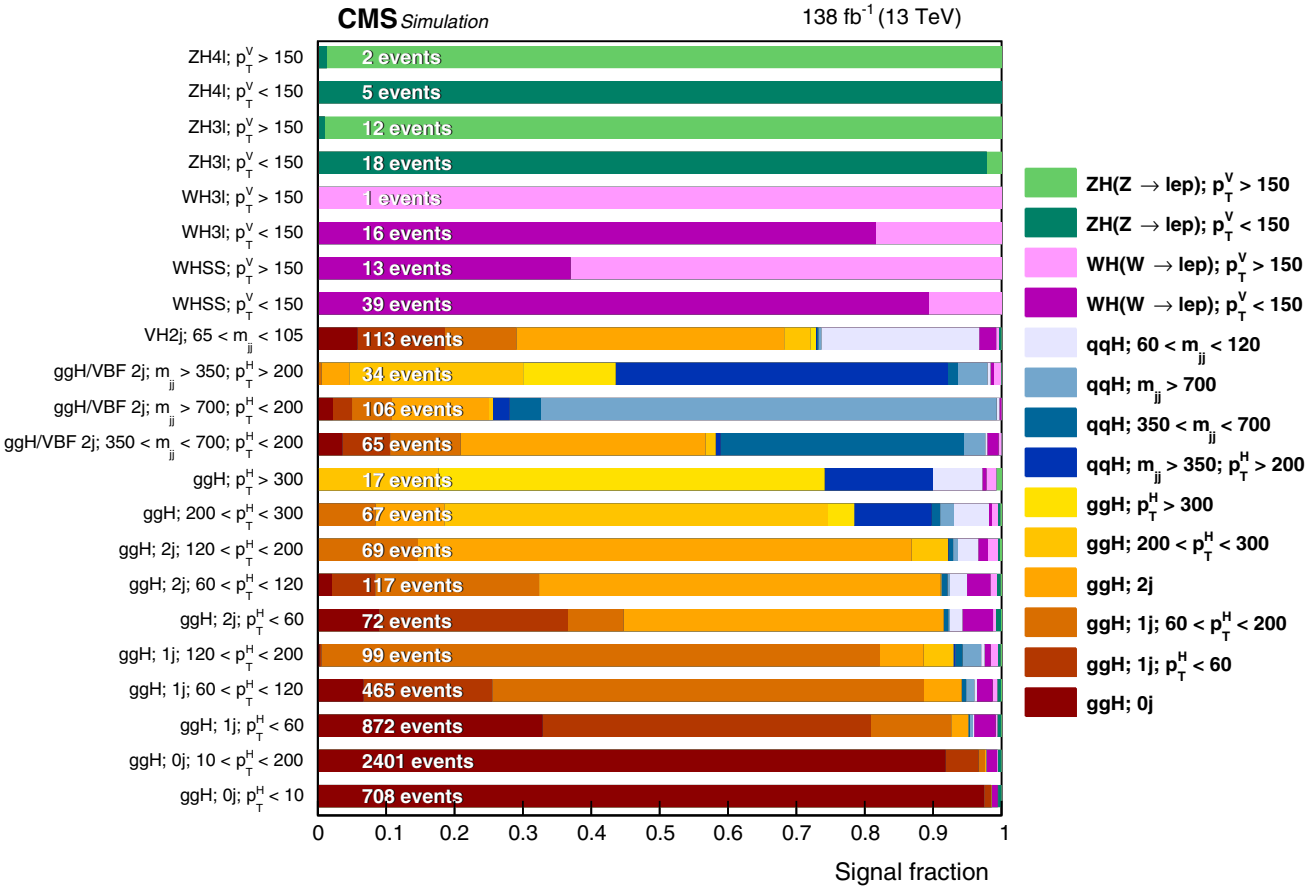


Fig. 20 Expected relative fractions of different STXS signal processes in each category. The total number of expected H → WW signal events in each category is also shown. All dimensional quantities in the definitions of bins are measured in GeV

9 Background estimation

9.1 Nonprompt lepton background

The nonprompt lepton backgrounds originating from leptonic decays of heavy quarks, hadrons misidentified as leptons, and electrons from photon conversions are suppressed by the identification and isolation requirements imposed on electrons and muons. The nonprompt lepton background in the two-lepton final state primarily originates from W+jets events, while the nonprompt lepton background in the three-lepton final state primarily comes from Z+jets events. Top quark production with a jet misidentified as a lepton also contributes to the three-lepton final state. The nonprompt lepton background gives a negligible contribution in the four-lepton final state. This background is estimated from data, as described in detail in Ref. [7]. The rate at which a nonprompt lepton passing a loose selection further passes a tight selection (misidentification rate) is measured in a data sample enriched in events composed uniquely of jets produced through the strong interaction, referred to as QCD multijet events. The corresponding rate for a prompt lepton to pass this selection (prompt rate) is measured using a tag-and-probe method [71] in a data sample enriched in DY events. The misidentification and prompt rates are used to construct a relation between the number of leptons passing the loose selection, the number of leptons passing the tight selection, and the number of true prompt leptons in an event. This relation is applied as a transfer function to a data sample containing leptons passing the loose selection, weighting the events by the probability for N leptons to pass the tight selection while fewer than N leptons are truly prompt. The nonprompt background with two leptons is validated with data in a CR enriched with W+jets events, in which a pair of same-sign leptons is required, while the nonprompt background with three leptons is validated in a CR enriched with top quark events or DY events. The systematic uncertainty in the misidentification rate determination, which arises mainly from the different jet flavor composition between the events entering the QCD multijet and the analysis phase space, is estimated with a twofold approach. First, a validation check in the aforementioned CRs yields a normalization uncertainty of about 30% that fully covers any differences with respect to data in all the kinematic distributions of interest in this anal-

ysis. Second, a shape uncertainty is estimated by varying the jet p_T threshold used in the calculation of the misidentification rate in the 15–25 GeV range, in bins of the lepton η and p_T. For each threshold variation, the fake rate is recomputed and the difference with respect to the nominal fake rate is taken as a systematic uncertainty.

9.2 Top quark background

The background contributions from top quark processes are estimated using a combination of MC simulations and dedicated regions in data. A reweighting of the top quark and antiquark p_T spectra at parton level is performed for the $t\bar{t}$ simulation in order to match the NNLO and next-to-next-to-leading logarithmic (NNLL) QCD predictions, including also the NLO EW contribution [72]. A shape uncertainty based on renormalization (μ_R) and factorization (μ_F) scale variations is taken into account. For the ggH, VBF, and V H2j categories, in which the contribution of top quark backgrounds is dominant, the normalization of the simulated templates is left unconstrained in the fit separately for 0-, 1-, 2-jet ggH, VH, and VBF categories. The normalizations in these phase spaces are therefore measured from the data, by constraining the free-floating normalization parameters in top quark enriched CRs.

9.3 Nonresonant WW background

The nonresonant WW background is estimated using a combination of MC simulations and dedicated regions in data, and the quark-induced WW simulated events are reweighted to match the diboson p_T spectrum computed at NNLO+NNLL QCD accuracy [73,74]. The shape uncertainties related to the missing higher-order corrections are estimated by varying the μ_R and μ_F scales, as well as considering the independent variation of the resummation scale from its nominal value, taken as the mass of the W boson. For the ggH, VBF, and VH2j categories, the normalizations of the quark-induced and gluon-induced WW backgrounds are left unconstrained in the fit (the ratio between the two is kept fixed within the uncertainty), keeping a different parameter for each signal phase space as done for the top quark background. In the DF final states the normalization parameters are constrained directly in the SRs without the need of defining CRs, as the SRs span the high-$m_{\ell\ell}$ phase space enriched in WW events with a negligible Higgs boson signal contribution. Since in SF final states a counting analysis is performed, dedicated CRs enriched in WW events are defined selecting events with high $m_{\ell\ell}$. The normalizations of the EW and QCD WW+2 jets backgrounds are instead fixed to the respective SM cross sections provided by the MC simulation, taking into account the theoretical uncertainties arising from the variation of the μ_R and μ_F scales.

9.4 Drell–Yan background

The backgrounds arising from DY+jets processes are estimated using a different approach depending on the signal category.

In the ggH, VBF, and VH2j DF categories, the only source of DY background arises from $\tau\tau$ production with subsequent leptonic decays of the τ leptons. This background process is estimated with a data-embedding technique [75], in which $\mu^+\mu^-$ events with well-identified muons are selected in a data sample. In each event, the selected muons are removed and replaced with simulated τ leptons, keeping the same four-momentum of the initial muons. The embedded sample is then corrected using scale factors related to the simulation of τ leptons. The usage of the embedded sample allows for a better modeling of the observables that are sensitive to the detector response and calibration, such as $\vec{p}_T^{\,miss}$ and other variables related to the hadronic activity in the event. Since the embedded sample takes into account all processes with a $\tau\tau$ pair decaying to either electrons or muons, simulated $t\bar{t}$, single top, and diboson background events that contain a $\tau\tau$ pair are not considered in the analysis to avoid any double counting. To correct for any additional discrepancy associated with the different acceptance of the $H \to WW$ signal phase space, the normalization of the embedded samples is left unconstrained in the fit as done for top quark and WW backgrounds. An orthogonal $\tau\tau$ enriched CR is defined for the 0-, 1-, 2-jet ggH-like, 2-jet VH-like, and 2-jet VBF-like phase spaces to help in constraining the free normalization parameters. The embedded samples cover the events that pass the $e\mu$ triggers, which represent the vast majority of the events selected in the DF final state. The contribution of the remaining $\tau\tau$ events that enter the analysis phase space thanks to the single-lepton triggers ($\approx$5% of the total) is estimated using MC simulation.

In the ggH, VBF, and VH2j SF categories, the dominant background contribution arises from DY production of $\ell\ell$ pairs and is estimated using a data-driven technique described in Ref. [7]. The $\ell\ell$ background contribution for events with $|m_{\ell\ell} - m_Z| > 7.5$ GeV is estimated by counting the number of events in data passing a selection with an inverted $m_{\ell\ell}$ requirement (i.e., under the Z boson mass peak), subtracting the non-Z-boson contribution from it, and scaling the obtained yield by the fraction of events outside and inside the Z boson mass region in MC simulation. The contribution of processes such as top quark and WW production in the Z boson mass peak region, which have the same probability to decay into the ee, $e\mu$, μe, and $\mu\mu$ final states, is estimated by counting the number of $e^{\pm}\mu^{\mp}$ events in data, and applying a correction factor that accounts for the differences in the detection efficiency between electrons and muons. Other minor processes in the Z boson mass peak region (mainly ZZ and ZW) are subtracted based on MC simulations. The

yield obtained with this approach outside the Z boson mass peak is further corrected with a scale factor that takes into account the different acceptances between the estimation and SRs. The method is validated in orthogonal CRs enriched in DY events with a negligible signal contribution. The residual mismodeling between data and the estimated DY contribution arising from this validation is taken into account as a systematic uncertainty. The same procedure is repeated separately for estimating and validating the DY contribution in the e^+e^- and $\mu^+\mu^-$ final states.

In the leptonic VH categories DY represents a minor background and is estimated using MC simulations.

9.5 Multiboson background

In categories with two charged leptons, the production of WZ and Wγ^* contributes to the SRs whenever one of the three leptons is not identified. This background contribution is simulated as described in Sect. 3, and a data-to-simulation scale factor is derived in a three-lepton CR, orthogonal to the three-lepton SRs, as described in Ref. [7]. A normalization uncertainty of about 25% is associated to the scale factor determination. A different CR containing events with one pair of same-sign muons is also used as an additional validation of the Wγ^* simulation. The contribution of the Wγ process may also be a background in two-lepton SRs due to photon conversions in the detector material when one of the three leptons is not identified. This process is estimated using MC simulation and validated using data in a two-lepton CR requesting events with a leading μ and a trailing e with same sign and a separation in ΔR smaller than 0.5. These requirements mainly select events arising from Wγ production where the W boson decays to $\mu\nu_\mu$ and the photon is produced as final-state radiation from the muon. The theoretical uncertainties in Wγ and Wγ^* processes estimated using μ_R and μ_F scale variations are taken into account.

The WZ process represents one of the main backgrounds in the leptonic VH categories and its normalization is left as a free parameter in the fit, separately for different jet multiplicity categories. Dedicated 0-, 1- and 2-jet CRs are included in the fit to help constraining the WZ normalization parameters.

The production of a Z boson pair is the main background in the ZH4ℓ category and is estimated using MC simulation. The normalization of this background is left free to float and constrained using data in a ZZ-enriched CR.

Triple vector boson production is a minor background in all the considered categories and is estimated using MC simulation.

10 Statistical procedure and systematic uncertainties

The statistical approach used to interpret the selected data sets for this analysis and to combine the results from the independent categories has been developed by the ATLAS and CMS Collaborations in the context of the LHC Higgs Combination Group [76]. All selections have been optimized entirely on MC simulation and have been frozen before comparing the templates to data, in order to minimize possible biases. In all the categories considered, the signal extraction is performed using binned templates based on variables that allow for a good discrimination between signal and background, as summarized in Table 12. Therefore, the effect of each source of systematic uncertainty is either a change of the normalization of a given signal or background process, or a change of its template shape. The signal extraction is performed by a binned maximum likelihood fit, and each such change is modeled as a constrained nuisance parameter distributed according to a log-normal probability distribution function with standard deviation set to the size of the corresponding change. Where the change in shape of a template caused by a nuisance parameter is found to be negligible (i.e., its effect on the expected uncertainty on signal strength modifiers is well below 1%), only its effect on the normalization is considered.

The systematic uncertainties in this analysis arise either from an experimental or a theoretical source. The experimental uncertainties in the signal and background processes, as well as the theoretical uncertainties in the background processes, are taken into account for all the results discussed in Sect. 11. The treatment of the theoretical uncertainties in the signal processes is instead dependent on the measurement and interpretation being made. As an example, when measuring production cross sections for the STXS measurements, the theoretical uncertainties affecting the signal cross section in a given STXS bin are dropped and only the shape component is kept.

The following experimental uncertainties are included in the signal extraction fit.

- The integrated luminosities for the 2016, 2017, and 2018 data-taking years have 1.2–2.5% individual uncertainties, while the overall uncertainty for the 2016–2018 period is 1.6% [35–37]. This uncertainty is partially correlated among the three data sets, and is applied to all samples that are purely based on simulation.
- The uncertainties in the trigger efficiency and lepton reconstruction and identification efficiencies are modeled in bins of the lepton p_T and η, independently for electrons and muons. These uncertainties cause both a normalization and a shape change of the signal and background templates and are kept uncorrelated among the three data

Table 12 Overview of the fit variables and CRs used in each analysis category. In all CRs, the number of events is used. The number of subcategories shown in the last column includes both SRs and CRs

Category	SR subcategorization	SR fit variable	Contributing CRs	$N_{\text{subcategories}}$
ggH DF	(0j, 1j) × ($p_{\text{T}2} \lessgtr 20\,\text{GeV}$) × ($\ell^{\pm}\ell^{\mp}$), ($\geq$2j)	($m_{\ell\ell}$, m_{T}^{H})	Top quark, $\tau\tau$	15
ggH SF	(0j, 1j, $\geq$2j) × (ee, $\mu\mu$)	N_{events}	Top quark, WW	12
VBF DF	$\max_j C_j$	DNN output	Top quark, $\tau\tau$	6
VBF SF	(ee, $\mu\mu$)	N_{events}	Top quark, WW	4
WHSS	(DF, SF) × (1j, 2j)	$\widetilde{m}_{\text{H}}$	WZ	4
WH3ℓ	SF lepton pair with opposite or same sign	BDT output	WZ, Zγ	4
ZH3ℓ	(1j, 2j)	m_{T}^{H}	WZ	4
ZH4ℓ	(DF, SF)	BDT output	ZZ	3
VH2j DF	—	$m_{\ell\ell}$	Top quark, $\tau\tau$	3
VH2j SF	(ee, $\mu\mu$)	N_{events}	Top quark, WW	4

sets. Their effect is of ≈2% for electrons and ≈1% for muons.

- The uncertainties in the determination of the lepton momentum scale, jet energy scale, and unclustered energy scale cause the migration of the simulated events inside or outside the analysis acceptance, as well as migrations across the bins of the signal and background templates. The impact of these sources in the template normalizations is 0.6–1.0% for the electron momentum scale, 0.2% for the muon momentum scale, and 1–10% for $\vec{p}_{\text{T}}^{\,\text{miss}}$. The main contribution to these uncertainties arises from the limited data sample used for their estimation, and they are therefore treated as uncorrelated nuisance parameters among the three years. The jet energy scale uncertainty is modeled by implementing eleven independent nuisance parameters corresponding to different jet energy correction sources, six of which are correlated among the three data sets. Their effects vary in the range of 1–10%, according mainly to the jet multiplicity in the analysis phase space.
- The uncertainty in the jet energy resolution smearing applied to simulated samples to match the p_{T} resolution measured in data causes both a normalization and a shape change of the templates. This uncertainty has a minor impact on all the analyzed categories (effect below ≈ 1%) and is uncorrelated among the three data sets.
- The uncertainty in the pileup jet identification efficiency is modeled in bins of the jet p_{T} and η. It is considered for jets with $p_{\text{T}} < 50\,\text{GeV}$, since pileup jet identification techniques are only used for low-p_{T} jets. This uncertainty produces a change in both normalization and shape of the signal and background templates and is kept uncorrelated among the three data sets. The effect of this uncertainty on the measured quantities is found to be below 1%.
- The uncertainty in the b tagging efficiency is modeled by implementing seventeen nuisance parameters, five of which are related to the theoretical uncertainties involved in the measurements and are therefore correlated among the three data sets. The remaining four parameters per data set, which arise from the statistical accuracy of the efficiency measurement, are kept uncorrelated [31]. These uncertainties have an impact on both the shape of the templates and their normalization for all the simulated samples.
- The uncertainties in the nonprompt lepton background estimation affect both the normalization and shape of the templates of this process. They arise from the limited size of the data set used for the misidentification rate measurement and the difference in the flavor composition of jets mismeasured as leptons between the measurement region and the signal phase space. Both sources are implemented as uncorrelated nuisance parameters between electrons and muons, given the different mismeasurement probabilities for the two flavors, and are uncorrelated among the three data sets. Their effects vary between few percent to ≈ 10% depending on the SR. A further normalization uncertainty of 30% is assigned to cover any additional mismodeling of the jet flavor composition using data in control samples, as described in Sect. 9. The latter uncertainty is correlated among the data sets, but uncorrelated among SRs containing different lepton flavor combinations, for which the main mechanism of nonprompt lepton production arises from different processes.

- The statistical uncertainty due to the limited number of simulated events is associated with each bin of the simulated signal and background templates [77].

The theoretical uncertainties relevant to the simulated MC samples have different sources: the choice of the PDF set and the strong coupling constant α_S, missing higher-order corrections in the perturbative expansion of the simulated matrix elements, and modeling of the pileup. Template variations, both in shape and normalization, associated with the aforementioned sources are treated as correlated nuisance parameters for the three data sets.

The uncertainties in the PDF set and α_S choice are found to have a negligible effect on the simulated templates (the effect of the shape variation on the expected uncertainties was found to be below 1%), therefore only the normalization change is considered, taking into account the effect due to the cross section and acceptance variation. These uncertainties are not considered for backgrounds with normalization constrained through data in dedicated CRs. For the Higgs boson signal processes, these theoretical uncertainties are computed by the LHC Higgs Cross Section Working Group [55] for each production mechanism.

The effect of missing higher-order corrections for the background processes is estimated by reweighting the MC simulation events with alternative event weights, where the μ_R and μ_F scales are varied by a factor of 0.5 or 2, and the envelopes of the varied templates are taken as the one standard deviation variation. All the combinations of the μ_R and μ_F scale variations are considered for computing the envelope, except for the extreme case where μ_R is varied by 0.5 and μ_F by 2, or vice versa. For backgrounds with normalization constrained using data in dedicated CRs, only the shape variation of the simulated templates arising from this procedure is considered. For the WW background, an uncertainty in the higher-order reweighting described in Sect. 9 is derived by shifting μ_R, μ_F, and the resummation scale. For the ggH signal sample, the uncertainties are decomposed into several sources according to Ref. [55], to account for the overall cross section, migrations of events among jet multiplicity and p_T^H bins, choice of the resummation scale, and finite top quark mass effects. For the VBF signal sample, different sources of uncertainty are also decoupled to account for the overall normalization, migrations of events among Higgs boson p_T, N_{jet}, and m_{jj} bins, and EW corrections to the production cross section. The uncertainties due to missing higher-order corrections for the other signal samples are taken from Ref. [55]. For both PDF and missing higher-order uncertainties, the nuisance parameters are correlated for the WH and ZH processes and uncorrelated for the other ones.

In order to assess the uncertainty in the pileup modeling, the total inelastic pp cross section of 69.2 mb [78,79] is varied within a 5% uncertainty, which includes the uncertainty in the inelastic cross section measurement, as well as the difference in the primary vertex reconstruction efficiency between data and simulation.

A theoretical uncertainty due to the modeling of the PS and UE is taken into account for all the simulated samples. The uncertainty in the PS modeling is evaluated by varying the PS weights computed by PYTHIA 8.212 on an event-by-event basis, keeping the variations of the weights related to initial- and final-state radiation contributions uncorrelated. The uncertainty in the UE modeling is evaluated by shifting the nominal templates according to alternative MC simulations generated with a variation of the UE tune within its uncertainty. The corresponding nuisance parameter is correlated among all samples and between 2017 and 2018 data sets. An uncorrelated nuisance parameter is used for the 2016 data set, as the corresponding simulations are based on a different UE tune. The PS uncertainty affects the shape of the templates mainly through the migration of events across jet multiplicity bins, while the UE uncertainty is found to have a negligible impact on the shape of the templates and a normalization effect of $\approx 1.5\%$.

Additional theoretical uncertainties in specific background processes are also taken into account. A 15% uncertainty is assigned to the relative fraction of the gluon-induced component in the WW background process [62]. An uncertainty of 8% is assigned to the relative fraction of single top quark and $t\bar{t}$ processes. A 30% uncertainty is assigned to the $W\gamma^*$ process associated with the measurement of the scale factor in the trilepton CR.

For the measurement of the signal cross sections in the STXS framework, the effect of theoretical uncertainties in the template normalizations is removed for signal processes in each STXS bin being measured. In cases where two or more STXS bins are measured together because of the lack of statistical accuracy in measuring single bin cross sections, the shape effect of theoretical uncertainties causing event migrations among the merged bins is kept. In addition, residual theoretical uncertainties arising from μ_R and μ_F variations are taken into account to describe the acceptance effects that cause a shape variation of the signal templates within each STXS bin. The latter uncertainties are correlated among STXS bins that share a similar phase space definition, for example, ggH 0-jet bins, ggH 1-jet bins, ggH high-p_T bins, and ggH in VBF topology bins. A similar approach is used for the VBF STXS bins. For the measurement of leptonic VH cross sections in STXS bins, the aforementioned theoretical uncertainties are found to have a marginal impact with respect to the measurement statistical accuracy and have been neglected.

The contributions of different sources of systematic uncertainty in the signal strength measurement are summarized in Table 13.

Table 13 Contributions of different sources of uncertainty in the signal strength measurement. The systematic component includes the combined effect from all sources besides background normalization and the size of the dataset, which make up the statistical part

Uncertainty source	$\Delta\mu/\mu$	$\Delta\mu_{\mathrm{ggH}}/\mu_{\mathrm{ggH}}$	$\Delta\mu_{\mathrm{VBF}}/\mu_{\mathrm{VBF}}$	$\Delta\mu_{\mathrm{WH}}/\mu_{\mathrm{WH}}$	$\Delta\mu_{\mathrm{ZH}}/\mu_{\mathrm{ZH}}$
Theory (signal)	4%	5%	13%	2%	<1%
Theory (background)	3%	3%	2%	4%	5%
Lepton misidentification	2%	2%	9%	15%	4%
Integrated luminosity	2%	2%	2%	2%	3%
b tagging	2%	2%	3%	<1%	2%
Lepton efficiency	3%	4%	2%	1%	4%
Jet energy scale	1%	<1%	2%	<1%	3%
Jet energy resolution	<1%	1%	<1%	<1%	3%
$p_{\mathrm{T}}^{\mathrm{miss}}$ scale	<1%	1%	<1%	2%	2%
PDF	1%	2%	<1%	<1%	2%
Parton shower	<1%	2%	<1%	1%	1%
Backg. norm.	3%	4%	6%	4%	6%
Stat. uncertainty	5%	6%	28%	21%	31%
Syst. uncertainty	9%	10%	23%	19%	11%
Total uncertainty	10%	11%	36%	29%	33%

11 Results

Results are presented in terms of signal strength modifiers, STXS cross sections, and coupling modifiers. In all cases they are extracted via a simultaneous maximum likelihood fit to all the analysis categories, as explained in Sect. 10. The mass of the Higgs boson is assumed to be 125.38 GeV, as measured by the CMS Collaboration [56]. The effect on event yields of varying m_{H} within its uncertainty is found to be below 1%. The number of expected and measured events for signal and background processes, as well as the number of observed events in each category, are reported in Tables 14, 15, 16 and 17. The normalization factors of the background contributions are found to be consistent with unity within their uncertainties. Figure 21 summarizes the full analysis template by showing the distribution of events as a function of the observed significance of the corresponding bins.

The $\mathrm{H} \rightarrow \mathrm{WW}$ selection is subject to some degree of contamination from events in which the Higgs boson decays to a pair of τ leptons that themselves decay leptonically. These events are included in the signal definition, and their contribution ranges from below 1% in the ggH and VBF categories up to $\approx 10\%$ in some of the WH categories. As described in previous sections, CRs are used to fix the normalization of dominant backgrounds from data. This is achieved by scaling the corresponding background contributions jointly in the CR and SR. Given that the procedure effectively amounts to a measurement of the cross section of the background in question, the contributions from the 2017 and 2018 data sets are scaled together. The 2016 data set is kept separate in this regard because a different PYTHIA tune was used.

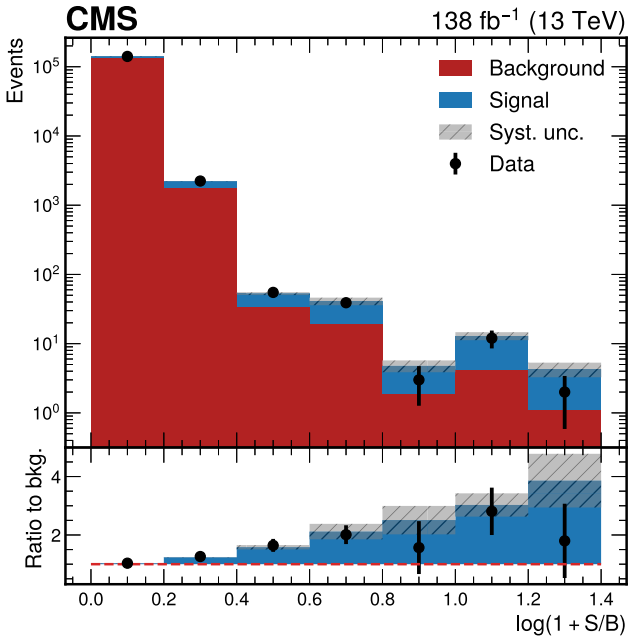


Fig. 21 Distribution of events as a function of the statistical significance of their corresponding bin in the analysis template, including all categories. Signal and background contributions are shown after the fit to the data

For inclusive measurements, results are extracted in the form of signal strength modifiers μ. These are defined as the product of the production cross section and the branching ratio to a W boson pair, normalized to the SM prediction $(\sigma\mathcal{B}/(\sigma\mathcal{B})_{\mathrm{SM}})$. Couplings of the Higgs boson to fermions and vector bosons are measured in the κ framework [80], while STXS results are provided as cross sections.

Table 14 Number of events by process in the ggH DF categories after the fit to the data, scaling the ggH, VBF, WH, and ZH production modes separately. The $t\bar{t}H$ contribution is fixed to its SM expectation. Numbers in parenthesis indicate expected yields

Process	0-jets ggH DF	1-jet ggH DF	2-jets ggH DF
ggH	1875 ± 45 (2157)	881 ± 28 (942)	67 ± 5 (71)
VBF	15 ± 2 (23)	62 ± 7 (92)	4 ± 1 (6)
WH	103 ± 7 (51)	124 ± 10 (60)	18 ± 2 (9)
ZH	38 ± 3 (19)	33 ± 3 (17)	7 ± 1 (4)
$t\bar{t}H$	—	1 ± 1 (1)	1 ± 1 (1)
Total signal	2032 ± 51 (2250)	1101 ± 31 (1111)	99 ± 6 (90)
WW	37297 ± 285 (34781)	12703 ± 307 (14932)	748 ± 121 (1101)
Top quark	10165 ± 179 (10204)	19711 ± 298 (19766)	3989 ± 123 (3868)
Nonprompt	4407 ± 225 (5888)	1999 ± 141 (2769)	252 ± 42 (262)
DY	495 ± 24 (563)	822 ± 12 (792)	87 ± 4 (86)
$VZ/V\gamma^*$	1464 ± 45 (1776)	1297 ± 44 (1531)	123 ± 7 (140)
$V\gamma$	1181 ± 19 (1273)	723 ± 18 (777)	57 ± 3 (56)
Triboson	38 ± 1 (39)	66 ± 1 (72)	13 ± 1 (14)
Total background	55045 ± 409 (54524)	37321 ± 453 (40639)	5269 ± 178 (5526)
Total prediction	57077 ± 412 (56773)	38422 ± 454 (41750)	5368 ± 178 (5616)
Data	57024	38373	5380

Table 15 Number of events by process in the ggH SF categories after the fit to the data, scaling the ggH, VBF, WH, and ZH production modes separately. The $t\bar{t}H$ contribution is fixed to its SM expectation. Numbers in parenthesis indicate expected yields

Process	0-jets ggH SF	1-jet ggH SF	2-jets ggH SF
ggH	780 ± 31 (891)	397 ± 18 (422)	86 ± 7 (89)
VBF	5 ± 1 (7)	29 ± 4 (42)	10 ± 1 (13)
WH	24 ± 3 (11)	34 ± 4 (16)	12 ± 1 (6)
ZH	14 ± 1 (7)	16 ± 2 (8)	7 ± 1 (3)
$t\bar{t}H$	—	—	1 ± 1 (1)
Total signal	823 ± 31 (915)	476 ± 18 (489)	114 ± 7 (112)
WW	7034 ± 184 (6464)	2711 ± 128 (3064)	276 ± 61 (480)
Top quark	1345 ± 42 (1294)	3711 ± 75 (3524)	1879 ± 51 (1758)
Nonprompt	641 ± 88 (701)	366 ± 54 (412)	103 ± 18 (119)
DY	3149 ± 271 (2706)	4098 ± 197 (3284)	1403 ± 83 (829)
$VZ/V\gamma^*$	327 ± 13 (371)	270 ± 10 (301)	63 ± 4 (70)
$V\gamma$	138 ± 6 (145)	193 ± 15 (201)	48 ± 5 (47)
Triboson	4 ± 1 (5)	10 ± 1 (11)	6 ± 1 (6)
Total background	12639 ± 342 (11684)	11359 ± 253 (10797)	3777 ± 117 (3309)
Total prediction	13462 ± 343 (12599)	11835 ± 254 (11286)	3891 ± 117 (3421)
Data	13507	11976	3950

11.1 Signal strength modifiers

The global signal strength modifier is extracted by fitting the template to data leaving all contributions coming from the Higgs boson free to float, but keeping the relative importance of the different production modes fixed to the values predicted by the SM. As such, this measurement gives information on the compatibility of the SM with the LHC Run 2 data set. The observed signal strength modifier is:

$$\mu = 0.95^{+0.10}_{-0.09} = 0.95 \pm 0.05\,(\text{stat}) \pm 0.08\,(\text{syst}), \quad (4)$$

where the uncertainty has been broken down into its statistical and systematic components. The purely statistical component is extracted by fixing all nuisance parameters in the likelihood function to their best fit values and extracting the corresponding profile. The systematic component is obtained

Table 16 Number of events by process in the VBF and VH2j categories after the fit to the data, scaling the ggH, VBF, WH, and ZH production modes separately. The $t\bar{t}H$ contribution is fixed to its SM expectation. Numbers in parenthesis indicate expected yields

Process	VBF DF	VBF SF	VH2j DF	VH2j SF
ggH	114 ± 8 (115)	21 ± 2 (21)	36 ± 3 (39)	27 ± 2 (29)
VBF	62 ± 11 (91)	39 ± 5 (57)	2 ± 1 (3)	2 ± 1 (2)
WH	14 ± 1 (7)	1 ± 1 (1)	26 ± 4 (13)	16 ± 2 (8)
ZH	5 ± 1 (2)	1 ± 1 (0)	13 ± 2 (7)	8 ± 1 (4)
$t\bar{t}H$	—	—	—	—
Total signal	195 ± 14 (215)	62 ± 6 (79)	77 ± 5 (62)	53 ± 3 (43)
WW	1319 ± 57 (1368)	109 ± 17 (102)	98 ± 44 (205)	56 ± 22 (134)
Top quark	2875 ± 65 (3148)	267 ± 8 (249)	743 ± 32 (730)	539 ± 16 (514)
Nonprompt	404 ± 36 (399)	28 ± 4 (32)	81 ± 13 (113)	62 ± 10 (72)
DY	249 ± 4 (241)	402 ± 27 (465)	77 ± 3 (77)	555 ± 48 (479)
VZ/Vγ^*	184 ± 9 (221)	11 ± 1 (12)	49 ± 3 (55)	23 ± 2 (27)
Vγ	110 ± 4 (117)	10 ± 1 (10)	26 ± 3 (25)	16 ± 5 (17)
Triboson	11 ± 1 (11)	1 ± 1 (1)	6 ± 1 (7)	4 ± 1 (3)
Total background	5154 ± 94 (5505)	827 ± 33 (871)	1080 ± 56 (1212)	1255 ± 56 (1245)
Total prediction	5349 ± 95 (5720)	889 ± 34 (950)	1157 ± 56 (1274)	1308 ± 56 (1288)
Data	5254	862	1164	1318

Table 17 Number of events by process in the WHSS, WH3ℓ, ZH3ℓ, and ZH4ℓ categories after the fit to the data, scaling the ggH, VBF, WH, and ZH production modes separately. The $t\bar{t}H$ contribution is fixed to its SM expectation. Numbers in parenthesis indicate expected yields

Process	WHSS	WH3ℓ	ZH3ℓ	ZH4ℓ
ggH	1 ± 1 (1)	—	—	—
VBF	—	—	—	—
WH	148 ± 12 (69)	44 ± 5 (20)	2 ± 1 (1)	—
ZH	10 ± 11 (5)	3 ± 1 (2)	74 ± 7 (36)	19 ± 2 (10)
$t\bar{t}H$	1 ± 1 (1)	—	1 ± 1 (1)	—
Total signal	159 ± 12 (76)	48 ± 5 (22)	76 ± 7 (38)	19 ± 2 (10)
WW	40 ± 1 (39)	—	—	—
Top quark	62 ± 1 (62)	—	—	—
Nonprompt	596 ± 37 (805)	55 ± 6 (85)	166 ± 16 (215)	—
DY	28 ± 7 (35)	—	30 ± 1 (29)	1 ± 1 (1)
VZ/Vγ^*	1309 ± 26 (1355)	311 ± 10 (276)	1905 ± 25 (1796)	45 ± 1 (39)
Vγ	135 ± 11 (162)	14 ± 3 (20)	36 ± 6 (40)	—
Triboson	41 ± 1 (41)	15 ± 1 (15)	30 ± 1 (30)	3 ± 1 (3)
Total background	2211 ± 47 (2498)	396 ± 12 (397)	2167 ± 30 (2110)	50 ± 1 (44)
Total prediction	2370 ± 49 (2574)	444 ± 13 (419)	2243 ± 31 (2148)	69 ± 2 (54)
Data	2359	423	2315	69

by the difference in quadrature between the total uncertainty and the statistical one. The observed and expected profile likelihood functions, both with the full set of uncertainty sources as well as with statistical ones only, are shown in Fig. 22.

Results are also extracted for individual production modes, by performing a 4-parameter fit in which contributions from the ggH, VBF, WH, and ZH modes are left free to float independently. Contributions from the $t\bar{t}H$ and $b\bar{b}H$ production modes are fixed to their SM expected values within uncertainties, given that this analysis has little sensitivity to them. Results are summarized in Fig. 23, where the separate contributions of statistical and systematic sources of uncertainty are also shown. Results correspond to observed (expected) significances of 10.5 (11.8)σ, 3.15 (4.74)σ, 3.61 (1.82)σ, and 3.73 (2.19)σ for the ggH, VBF, WH, and ZH

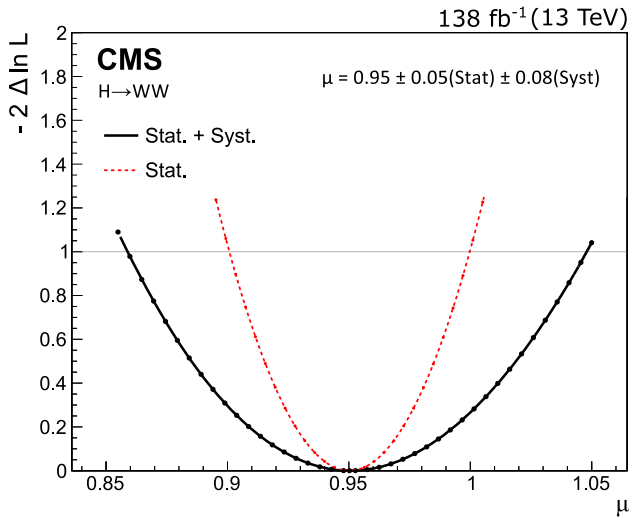


Fig. 22 Observed profile-likelihood function for the global signal strength modifier μ. The dashed curve corresponds to the profile-likelihood function obtained considering statistical uncertainties only

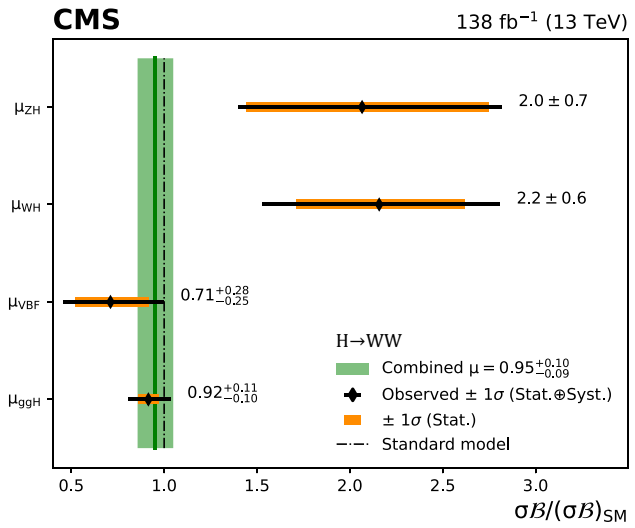


Fig. 23 Observed signal strength modifiers for the main SM production modes

modes, respectively. The correlation matrix among the signal strengths is given in Fig. 24. The compatibility of the result with the SM is found to be 7%.

11.2 Higgs boson couplings

Given its large branching fraction and relatively low background, the H → WW channel is a good candidate to measure the couplings of the Higgs boson to fermions and vector bosons. This is performed in the so-called κ framework. Two coupling modifiers κ_V and κ_f are defined, for couplings to vector bosons and fermions respectively. These scale the

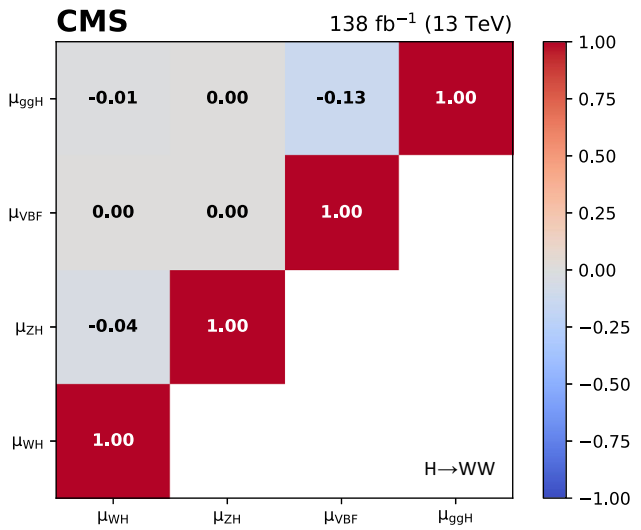


Fig. 24 Correlation matrix between the signal strength modifiers of the main production modes of the Higgs boson

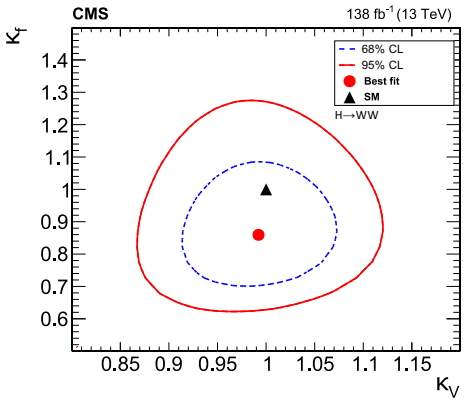


Fig. 25 Two-dimensional likelihood profile as a function of the coupling modifiers κ_V and κ_f, using the κ-framework parametrization. The 95 and 68% confidence level contours are shown as continuous and dashed lines, respectively

signal yield of the H → WW channel as follows:

$$\sigma\mathcal{B}(\mathrm{X}_i \to \mathrm{H} \to \mathrm{WW}) = \kappa_i^2 \frac{\kappa_\mathrm{V}^2}{\kappa_\mathrm{H}^2} \sigma_\mathrm{SM}\mathcal{B}_\mathrm{SM}(\mathrm{X}_i \to \mathrm{H} \to \mathrm{WW}), \quad (5)$$

where $\kappa_\mathrm{H} = \kappa_\mathrm{H}(\kappa_\mathrm{V}, \kappa_\mathrm{f})$ is the modifier to the total Higgs boson width, and X_i are the different production modes. The corresponding coupling modifiers κ_i equal κ_f for the ggH, $\mathrm{t\bar{t}H}$, and $\mathrm{b\bar{b}H}$ modes, and κ_V for the VBF and VH modes. Possible contributions to the total width of the Higgs boson coming from outside of the SM are neglected. The best fit values for the coupling modifiers are found to be $\kappa_\mathrm{V} = 0.99 \pm 0.05$ and $\kappa_\mathrm{f} = 0.86^{+0.14}_{-0.11}$, where the better sensitivity to κ_V is due to the H → WW decay vertex. The two-dimensional likelihood profile for the fit is shown in Fig. 25.

Table 18 Observed cross sections of the H → WW process in each STXS bin. The uncertainties in the observed cross sections and their ratio to the SM expectation do not include the theoretical uncertainties on the latter. In cases where the ratio to the SM cross section is measured below zero, an upper limit at 68% confidence level on the observed cross section is reported. All dimensional quantities in STXS bin definitions are measured in GeV

STXS bin	$\sigma(\mathrm{H}\to\mathrm{WW})/\sigma(\mathrm{H}\to\mathrm{WW})_{\mathrm{SM}}$	$\sigma(\mathrm{H}\to\mathrm{WW})$ [pb]	$\sigma(\mathrm{H}\to\mathrm{WW})_{\mathrm{SM}}$ [pb]
ZH (Z → leptons); $p_{\mathrm{T}}^{\mathrm{V}} > 150$	$-0.1^{+1.2}_{-0.9}\,(\mathrm{stat}) \pm 0.1\,(\mathrm{theo})^{+0.4}_{-0.3}\,(\mathrm{exp})$	<0.03	0.139 ± 0.013
ZH (Z → leptons); $p_{\mathrm{T}}^{\mathrm{V}} < 150$	$3.3^{+1.0}_{-0.9}\,(\mathrm{stat}) \pm 0.1\,(\mathrm{theo})^{+0.4}_{-0.3}\,(\mathrm{exp})$	0.10 ± 0.03	0.030 ± 0.004
WH (W → leptons); $p_{\mathrm{T}}^{\mathrm{V}} > 150$	$3.8^{+1.5}_{-1.3}\,(\mathrm{stat}) \pm 0.1\,(\mathrm{theo})^{+0.8}_{-0.7}\,(\mathrm{exp})$	$0.8^{+0.4}_{-0.3}$	0.22 ± 0.02
WH (W → leptons); $p_{\mathrm{T}}^{\mathrm{V}} < 150$	$1.6 \pm 0.8\,(\mathrm{stat}) \pm 0.1\,(\mathrm{theo})^{+0.7}_{-0.6}\,(\mathrm{exp})$	0.06 ± 0.04	0.035 ± 0.005
qqH; $60 < m_{\mathrm{jj}} < 120$	$4.1 \pm 2.6\,(\mathrm{stat})^{+0.7}_{-0.6}\,(\mathrm{theo}) \pm 2.2\,(\mathrm{exp})$	1.5 ± 1.2	0.36 ± 0.01
qqH; $p_{\mathrm{T}}^{\mathrm{H}} > 200$	$1.1^{+0.7}_{-0.6}\,(\mathrm{stat}) \pm 0.1\,(\mathrm{theo}) \pm 0.3\,(\mathrm{exp})$	$0.17^{+0.11}_{-0.10}$	0.15 ± 0.02
qqH; $p_{\mathrm{T}}^{\mathrm{H}} < 200$; $m_{\mathrm{jj}} > 700$	$0.7 \pm 0.3\,(\mathrm{stat}) \pm 0.1\,(\mathrm{theo}) \pm 0.2\,(\mathrm{exp})$	$0.023^{+0.011}_{-0.010}$	0.032 ± 0.004
qqH; $p_{\mathrm{T}}^{\mathrm{H}} < 200$; $350 < m_{\mathrm{jj}} < 700$	$0.4^{+0.8}_{-0.7}\,(\mathrm{stat}) \pm 0.2\,(\mathrm{theo}) \pm 0.5\,(\mathrm{exp})$	0.04 ± 0.10	0.11 ± 0.03
ggH; $p_{\mathrm{T}}^{\mathrm{H}} > 300$	$-2.1^{+1.7}_{-1.5}\,(\mathrm{stat})^{+0.2}_{-0.3}\,(\mathrm{theo})^{+1.6}_{-2.0}\,(\mathrm{exp})$	<0.04	0.028 ± 0.009
ggH; $200 < p_{\mathrm{T}}^{\mathrm{H}} < 300$	$2.3 \pm 0.9\,(\mathrm{stat}) \pm 0.1\,(\mathrm{theo}) \pm 0.6\,(\mathrm{exp})$	0.22 ± 0.10	0.09 ± 0.02
ggH; ≥2j	$1.8 \pm 0.6\,(\mathrm{stat}) \pm 0.4\,(\mathrm{theo}) \pm 0.4\,(\mathrm{exp})$	1.5 ± 0.7	0.9 ± 0.4
ggH; 1j; $p_{\mathrm{T}}^{\mathrm{H}} > 60$	$0.41 \pm 0.25\,(\mathrm{stat})^{+0.10}_{-0.06}\,(\mathrm{theo}) \pm 0.17\,(\mathrm{exp})$	0.5 ± 0.4	1.15 ± 0.16
ggH; 1j; $p_{\mathrm{T}}^{\mathrm{H}} < 60$	$1.7 \pm 0.3\,(\mathrm{stat}) \pm 0.2\,(\mathrm{theo}) \pm 0.2\,(\mathrm{exp})$	$2.6^{+0.7}_{-0.6}$	1.5 ± 0.2
ggH; 0j	$0.74 \pm 0.07\,(\mathrm{stat}) \pm 0.04\,(\mathrm{theo})^{+0.08}_{-0.07}\,(\mathrm{exp})$	$4.2^{+0.7}_{-0.6}$	5.8 ± 0.3

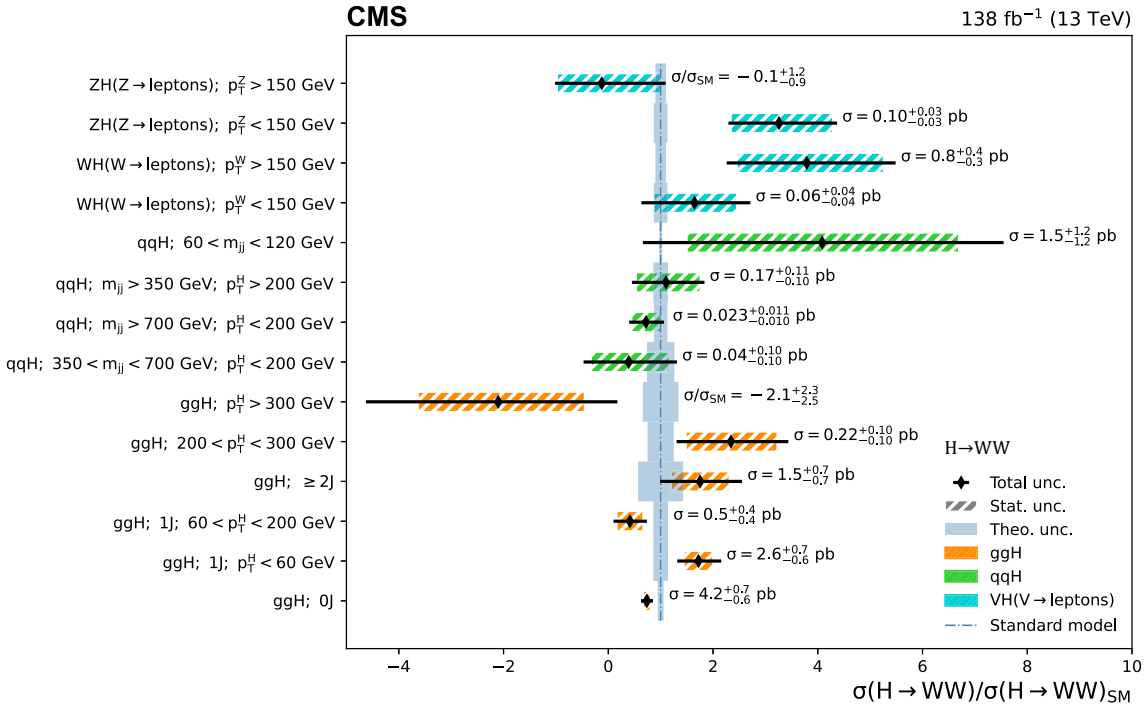


Fig. 26 Observed cross sections of the H → WW process in each STXS bin, normalized to the SM expectation

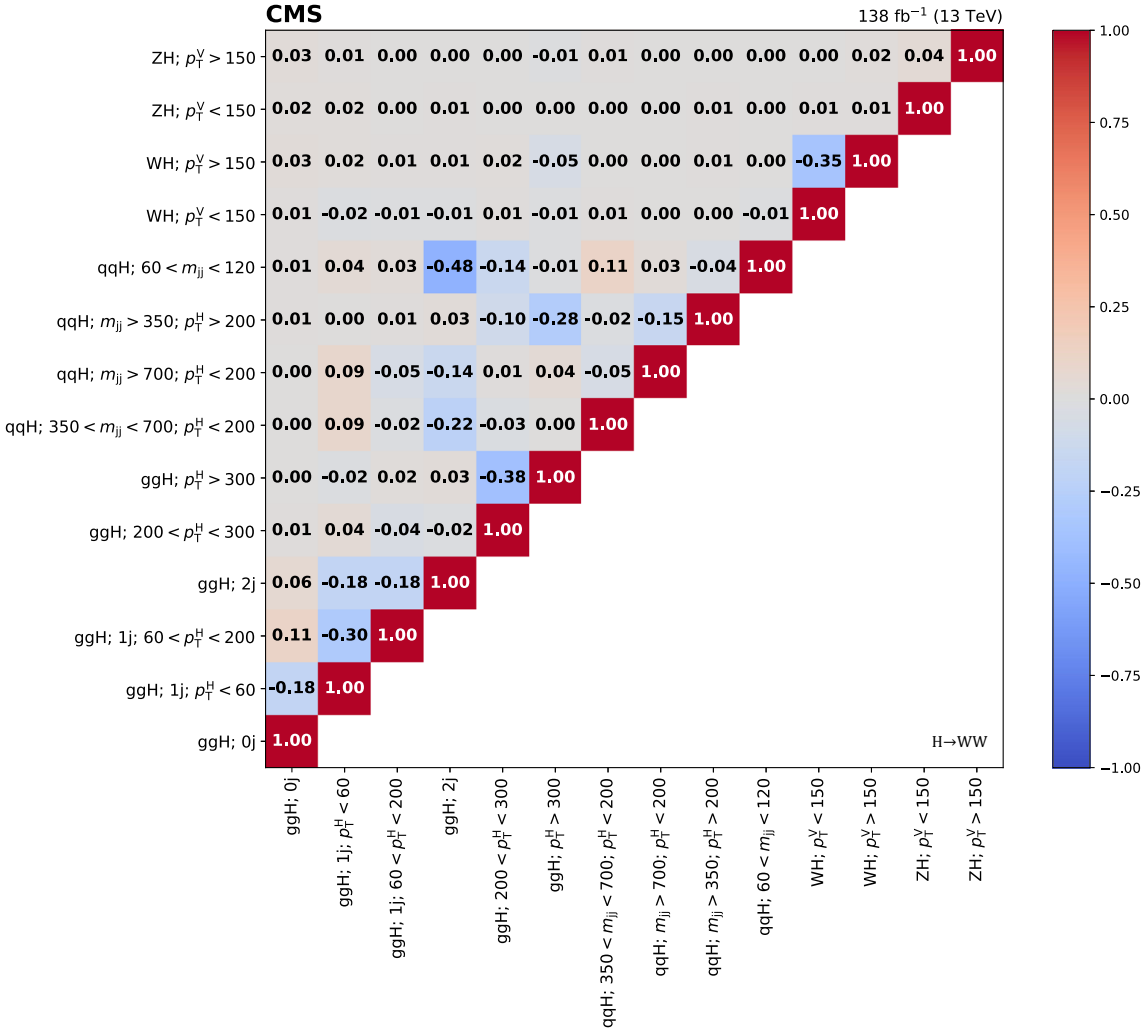


Fig. 27 Correlation matrix between the measured STXS bins. All dimensional quantities in bin definitions are measured in GeV

11.3 STXS

As explained in Sect. 8, the STXS measurement is carried out under the Stage 1.2 framework, although not all STXS bins are measured independently because of sensitivity limitations. Results are shown in Table 18 and in Fig. 26, for the signal strength modifiers and cross sections. The uncertainties are reported separately for statistical (stat), theoretical (theo), and experimental (exp) systematic sources. The correlation matrix for the measured STXS bins is shown in Fig. 27. Since final results are reported as cross sections, the effect of theoretical uncertainties in the normalization of signal templates is dropped, while uncertainties in the shape of the templates, such as STXS bin migration, are accounted for. In cases where cross sections are measured to be zero, an upper limit is reported instead of a symmetric confidence interval, so that all intervals reported correspond to a 68% confidence level. The compatibility of the STXS fit with the SM is found to be 1%.

12 Summary

A measurement of production cross sections for the Higgs boson has been performed targeting the gluon fusion, vector boson fusion, and Z or W associated production processes in the H $\rightarrow$ WW decay channel. Results are presented as signal strength modifiers, coupling modifiers, and differential cross sections in the simplified template cross section Stage 1.2 framework. The measurement has been performed on data from proton-proton collisions recorded by the CMS detector at a center-of-mass energy of 13 TeV in 2016–2018, corresponding to an integrated luminosity of 138 fb^{-1}. Specific event selections targeting different final states have been employed, and results have been extracted via a simultaneous maximum likelihood fit to all analysis categories. The overall signal strength for production of a Higgs boson is found to be $\mu = 0.95^{+0.10}_{-0.09}$. All results are in good agreement with the standard model expectation.

Acknowledgements We congratulate our colleagues in the CERN accelerator departments for the excellent performance of the LHC and thank the technical and administrative staffs at CERN and at other CMS institutes for their contributions to the success of the CMS effort. In addition, we gratefully acknowledge the computing centers and personnel of the Worldwide LHC Computing Grid and other centers for delivering so effectively the computing infrastructure essential to our analyses. Finally, we acknowledge the enduring support for the construction and operation of the LHC, the CMS detector, and the supporting computing infrastructure provided by the following funding agencies: BMBWF and FWF (Austria); FNRS and FWO (Belgium); CNPq, CAPES, FAPERJ, FAPERGS, and FAPESP (Brazil); MES and BNSF (Bulgaria); CERN; CAS, MoST, and NSFC (China); MINCIENCIAS (Colombia); MSES and CSF (Croatia); RIF (Cyprus); SENESCYT (Ecuador); MoER, ERC PUT and ERDF (Estonia); Academy of Finland, MEC, and HIP (Finland); CEA and CNRS/IN2P3 (France); BMBF, DFG, and HGF (Germany); GSRI (Greece); NKFIH (Hungary); DAE and DST (India); IPM (Iran); SFI (Ireland); INFN (Italy); MSIP and NRF (Republic of Korea); MES (Latvia); LAS (Lithuania); MOE and UM (Malaysia); BUAP, CINVESTAV, CONACYT, LNS, SEP, and UASLP-FAI (Mexico); MOS (Montenegro); MBIE (New Zealand); PAEC (Pakistan); MES and NSC (Poland); FCT (Portugal); MESTD (Serbia); MCIN/AEI and PCTI (Spain); MOSTR (Sri Lanka); Swiss Funding Agencies (Switzerland); MST (Taipei); MHESI and NSTDA (Thailand); TUBITAK and TENMAK (Turkey); NASU (Ukraine); STFC (United Kingdom); DOE and NSF (USA). Individuals have received support from the Marie-Curie program and the European Research Council and Horizon 2020 Grant, contract Nos. 675440, 724704, 752730, 758316, 765710, 824093, 884104, and COST Action CA16108 (European Union); the Leventis Foundation; the Alfred P. Sloan Foundation; the Alexander von Humboldt Foundation; the Belgian Federal Science Policy Office; the Fonds pour la Formation á la Recherche dans l'Industrie et dans l'Agriculture (FRIA-Belgium); the Agentschap voor Innovatie door Wetenschap en Technologie (IWT-Belgium); the F.R.S.-FNRS and FWO (Belgium) under the "Excellence of Science – EOS" – be.h project n. 30820817; the Beijing Municipal Science & Technology Commission, No. Z191100007219010; the Ministry of Education, Youth and Sports (MEYS) of the Czech Republic; the Hellenic Foundation for Research and Innovation (HFRI), Project Number 2288 (Greece); the Deutsche Forschungsgemeinschaft (DFG), under Germany's Excellence Strategy – EXC 2121 "Quantum Universe" – 390833306, and under project number 400140256 - GRK2497; the Hungarian Academy of Sciences, the New National Excellence Program - ÚNKP, the NKFIH research grants K 124845, K 124850, K 128713, K 128786, K 129058, K 131991, K 133046, K 138136, K 143460, K 143477, 2020-2.2.1-ED-2021-00181, and TKP2021-NKTA-64 (Hungary); the Council of Science and Industrial Research, India; the Latvian Council of Science; the Ministry of Education and Science, project no. 2022/WK/14, and the National Science Center, contracts Opus 2021/41/B/ST2/01369 and 2021/43/B/ST2/01552 (Poland); the Fundação para a Ciência e a Tecnologia, grant CEECIND/01334/2018 (Portugal); the National Priorities Research Program by Qatar National Research Fund; MCIN/AEI/10.13039/501100011033, ERDF "a way of making Europe", and the Programa Estatal de Fomento de la Investigación Científica y Técnica de Excelencia María de Maeztu, grant MDM-2017-0765 and Programa Severo Ochoa del Principado de Asturias (Spain); the Chulalongkorn Academic into Its 2nd Century Project Advancement Project, and the National Science, Research and Innovation Fund via the Program Management Unit for Human Resources & Institutional Development, Research and Innovation, grant B05F650021 (Thailand); the Kavli Foundation; the Nvidia Corporation; the SuperMicro Corporation; the Welch Foundation, contract C-1845; and the Weston Havens Foundation (USA).

Data Availability Statement This manuscript has associated data in a data repository. [Authors' comment: Release and preservation of data used by the CMS Collaboration as the basis for publications is guided by the CMS policy as stated in https://cms-docdb.cern.ch/cgibin/PublicDocDB/RetrieveFile?docid=6032&filename=CMSDataPolicyV1.2.pdf&version=2 CMS preservation, re-use and open access policy.]

Declarations

Conflict of interest The authors declare that they have no conflict of interest.

Open Access This article is licensed under a Creative Commons Attribution 4.0 International License, which permits use, sharing, adaptation, distribution and reproduction in any medium or format, as long as you give appropriate credit to the original author(s) and the source, provide a link to the Creative Commons licence, and indicate if changes were made. The images or other third party material in this article are included in the article's Creative Commons licence, unless indicated otherwise in a credit line to the material. If material is not included in the article's Creative Commons licence and your intended use is not permitted by statutory regulation or exceeds the permitted use, you will need to obtain permission directly from the copyright holder. To view a copy of this licence, visit http://creativecommons.org/licenses/by/4.0/.

Funded by SCOAP[3]. SCOAP[3] supports the goals of the International Year of Basic Sciences for Sustainable Development.

References

1. ATLAS Collaboration, Observation of a new particle in the search for the standard model Higgs boson with the ATLAS detector at the LHC. Phys. Lett. B **716**, 1 (2012). https://doi.org/10.1016/j.physletb.2012.08.020. arXiv:1207.7214
2. CMS Collaboration, Observation of a new boson at a mass of 125 GeV with the CMS experiment at the LHC. Phys. Lett. B **716**, 30 (2012). https://doi.org/10.1016/j.physletb.2012.08.021. arXiv:1207.7235
3. CMS Collaboration, Observation of a new boson with mass near 125 GeV in pp collisions at $\sqrt{s} = 7$ and 8 TeV. JHEP **06**, 081 (2013). https://doi.org/10.1007/JHEP06(2013)081. arXiv:1303.4571
4. ATLAS and CMS Collaborations, Measurements of the Higgs boson production and decay rates and constraints on its couplings from a combined ATLAS and CMS analysis of the LHC pp collision data at $\sqrt{s} = 7$ and 8 TeV. JHEP **08**, 45 (2016). https://doi.org/10.1007/JHEP08(2016)045. arXiv:1606.02266
5. N. Berger et al., Simplified template cross sections—stage 1.1 (2019). arXiv:1906.02754
6. CMS Collaboration, Measurement of Higgs boson production and properties in the WW decay channel with leptonic final states. JHEP **01**, 096 (2014). https://doi.org/10.1007/JHEP01(2014)096. arXiv:1312.1129
7. CMS Collaboration, Measurements of properties of the Higgs boson decaying to a W boson pair in pp collisions at $\sqrt{s} = 13TeV$. Phys. Lett. B **791**, 96 (2019). https://doi.org/10.1016/j.physletb.2018.12.073. arXiv:1806.05246
8. CMS Collaboration, Measurement of the transverse momentum spectrum of the Higgs boson produced in pp collisions at $\sqrt{s} = 8TeV$ using $H \rightarrow WW$ decays. JHEP **03**, 032 (2017). https://doi.org/10.1007/JHEP03(2017)032. arXiv:1606.01522
9. CMS Collaboration, Measurement of the inclusive and differential Higgs boson production cross sections in the leptonic WW decay mode at $\sqrt{s} = 13$ TeV. JHEP **03**, 003 (2021). https://doi.org/10.1007/JHEP03(2021)003. arXiv:2007.01984

10. CMS Collaboration, Measurement of the inclusive and differential Higgs boson production cross sections in the decay mode to a pair of τ leptons in pp collisions at $\sqrt{s} = 13$ TeV. Phys. Rev. Lett. **128**, 081805 (2021). https://doi.org/10.1103/PhysRevLett.128.081805. arXiv:2107.11486
11. CMS Collaboration, Measurements of Higgs boson production cross sections and couplings in the diphoton decay channel at $\sqrt{s}$ = 13 TeV. JHEP **07**, 027 (2021). https://doi.org/10.1007/JHEP07(2021)027. arXiv:2103.06956
12. CMS Collaboration, Measurements of production cross sections of the Higgs boson in the four-lepton final state in proton–proton collisions at $\sqrt{s} = 13$ TeV. Eur. Phys. J. C **81**, 488 (2021). https://doi.org/10.1140/epjc/s10052-021-09200-x. arXiv:2103.04956
13. ATLAS Collaboration, Measurements of the Higgs boson inclusive and differential fiducial cross sections in the 4ℓ decay channel at $\sqrt{s}$ = 13 TeV. Eur. Phys. J. C **80**, 942 (2020). https://doi.org/10.1140/epjc/s10052-020-8223-0. arXiv:2004.03969
14. ATLAS Collaboration, Higgs boson production cross-section measurements and their EFT interpretation in the 4ℓ decay channel at $\sqrt{s}$ =13 TeV with the ATLAS detector. Eur. Phys. J. C **80**, 957 (2020). https://doi.org/10.1140/epjc/s10052-020-8227-9. arXiv:2004.03447. [Errata: https://doi.org/10.1140/epjc/s10052-020-08644-x, https://doi.org/10.1140/epjc/s10052-021-09116-6]
15. HEPData record for this analysis (2022). https://doi.org/10.17182/hepdata.130966
16. CMS Collaboration, Performance of the CMS Level-1 trigger in proton-proton collisions at $\sqrt{s}$ = 13 TeV. JINST **15**, P10017 (2020). https://doi.org/10.1088/1748-0221/15/10/P10017. arXiv:2006.10165
17. CMS Collaboration, The CMS trigger system. JINST **12**, P01020 (2017). https://doi.org/10.1088/1748-0221/12/01/P01020. arXiv:1609.02366
18. CMS Collaboration, The CMS experiment at the CERN LHC. JINST **3**, S08004 (2008). https://doi.org/10.1088/1748-0221/3/08/S08004
19. CMS Collaboration, Performance of the CMS muon detector and muon reconstruction with proton-proton collisions at $\sqrt{s} = 13TeV$. JINST **13**, P06015 (2018). https://doi.org/10.1088/1748-0221/13/06/P06015. arXiv:1804.04528
20. CMS Collaboration, Performance of the reconstruction and identification of high-momentum muons in proton-proton collisions at $\sqrt{s} = 13TeV$. JINST **15**, P02027 (2020). https://doi.org/10.1088/1748-0221/15/02/P02027. arXiv:1912.03516
21. CMS Collaboration, Performance of electron reconstruction and selection with the CMS detector in proton-proton collisions at $\sqrt{s} = 8TeV$. JINST **10**, P06005 (2015). https://doi.org/10.1088/1748-0221/10/06/P06005. arXiv:1502.02701
22. CMS Collaboration, Measurement of the Higgs boson production rate in association with top quarks in final states with electrons, muons, and hadronically decaying tau leptons at $\sqrt{s} = 13$ TeV. Eur. Phys. J. C **81**, 378 (2021). https://doi.org/10.1140/epjc/s10052-021-09014-x. arXiv:2011.03652
23. W. Waltenberger, R. Frühwirth, P. Vanlaer, Adaptive vertex fitting. J. Phys. G **34**, N343 (2007). https://doi.org/10.1088/0954-3899/34/12/N01
24. CMS Collaboration, Technical proposal for the Phase-II upgrade of the Compact Muon Solenoid. CMS Technical Proposal CERN-LHCC-2015-010, CMS-TDR-15-02 (2015). http://cds.cern.ch/record/2020886
25. CMS Collaboration, Particle-flow reconstruction and global event description with the CMS detector. JINST **12**, P10003 (2017). https://doi.org/10.1088/1748-0221/12/10/P10003. arXiv:1706.04965
26. M. Cacciari, G.P. Salam, G. Soyez, The anti-k_T jet clustering algorithm. JHEP **04**, 063 (2008). https://doi.org/10.1088/1126-6708/2008/04/063. arXiv:0802.1189
27. M. Cacciari, G.P. Salam, G. Soyez, FastJet user manual. Eur. Phys. J. C **72**, 1896 (2012). https://doi.org/10.1140/epjc/s10052-012-1896-2. arXiv:1111.6097
28. CMS Collaboration, Jet energy scale and resolution in the CMS experiment in pp collisions at 8 TeV. JINST **12**, P02014 (2017). https://doi.org/10.1088/1748-0221/12/02/P02014. arXiv:1607.03663
29. CMS Collaboration, Jet energy scale and resolution performance with 13 TeV data collected by CMS in 2016-2018. CMS Detector Performance Summary CMS-DP-2020-019 (2020). https://cds.cern.ch/record/2715872
30. CMS Collaboration, Jet algorithms performance in 13 TeV data. CMS Physics Analysis Summary CMS-PAS-JME-16-003 (2017). http://cds.cern.ch/record/2256875
31. CMS Collaboration, Identification of heavy-flavour jets with the CMS detector in pp collisions at 13 TeV. JINST **13**, P05011 (2018). https://doi.org/10.1088/1748-0221/13/05/P05011. arXiv:1712.07158
32. CMS Collaboration, CMS Phase 1 heavy flavour identification performance and developments. CMS Detector Performance Summary CMS-DP-2020-019 (2017). http://cds.cern.ch/record/2263802
33. CMS Collaboration, Performance of missing transverse momentum reconstruction in proton-proton collisions at $\sqrt{s}$ = 13 TeV using the CMS detector. JINST **14**, P07004 (2019). https://doi.org/10.1088/1748-0221/14/07/P07004. arXiv:1903.06078
34. D. Bertolini, P. Harris, M. Low, N. Tran, Pileup per particle identification. JHEP **10**, 059 (2014). https://doi.org/10.1007/JHEP10(2014)059. arXiv:1407.6013
35. CMS Collaboration, Precision luminosity measurement in proton-proton collisions at $\sqrt{s}$ = 13 TeV in 2015 and 2016 at CMS. Eur. Phys. J. C **81**, 800 (2021). https://doi.org/10.1140/epjc/s10052-021-09538-2. arXiv:2104.01927
36. CMS Collaboration, CMS luminosity measurement for the 2017 data-taking period at $\sqrt{s} = 13TeV$. CMS Physics Analysis Summary CMS-PAS-LUM-17-004 (2017). https://cds.cern.ch/record/2621960
37. CMS Collaboration, CMS luminosity measurement for the 2018 data-taking period at $\sqrt{s} = 13TeV$. CMS Physics Analysis Summary CMS-PAS-LUM-18-002 (2019). https://cds.cern.ch/record/2676164
38. NNPDF Collaboration, Parton distributions with QED corrections. Nucl. Phys. B **877**, 290 (2013). https://doi.org/10.1016/j.nuclphysb.2013.10.010. arXiv:1308.0598
39. NNPDF Collaboration, Unbiased global determination of parton distributions and their uncertainties at NNLO and at LO. Nucl. Phys. B **855**, 153 (2012). https://doi.org/10.1016/j.nuclphysb.2011.09.024. arXiv:1107.2652
40. NNPDF Collaboration, Parton distributions from high-precision collider data. Eur. Phys. J. C **77**, 663 (2017). https://doi.org/10.1140/epjc/s10052-017-5199-5. arXiv:1706.00428
41. CMS Collaboration, Event generator tunes obtained from underlying event and multiparton scattering measurements. Eur. Phys. J. C **76**, 155 (2016). https://doi.org/10.1140/epjc/s10052-016-3988-x. arXiv:1512.00815
42. CMS Collaboration, Extraction and validation of a new set of CMS PYTHIA8 tunes from underlying-event measurements. Eur. Phys. J. C **80**, 4 (2020). https://doi.org/10.1140/epjc/s10052-019-7499-4. arXiv:1903.12179
43. T. Sjöstrand et al., An introduction to PYTHIA 8.2. Comput. Phys. Commun. **191**, 159 (2015). https://doi.org/10.1016/j.cpc.2015.01.024. arXiv:1410.3012

44. P. Nason, A new method for combining NLO QCD with shower Monte Carlo algorithms. JHEP **11**, 040 (2004). https://doi.org/10.1088/1126-6708/2004/11/040. arXiv:hep-ph/0409146
45. S. Frixione, P. Nason, C. Oleari, Matching NLO QCD computations with parton shower simulations: the POWHEG method. JHEP **11**, 070 (2007). https://doi.org/10.1088/1126-6708/2007/11/070. arXiv:0709.2092
46. S. Alioli, P. Nason, C. Oleari, E. Re, A general framework for implementing NLO calculations in shower Monte Carlo programs: the POWHEG BOX. JHEP **06**, 043 (2010). https://doi.org/10.1007/JHEP06(2010)043. arXiv:1002.2581
47. E. Bagnaschi, G. Degrassi, P. Slavich, A. Vicini, Higgs production via gluon fusion in the POWHEG approach in the SM and in the MSSM. JHEP **02**, 088 (2012). https://doi.org/10.1007/JHEP02(2012)088. arXiv:1111.2854
48. P. Nason, C. Oleari, NLO Higgs boson production via vector-boson fusion matched with shower in POWHEG. JHEP **02**, 037 (2010). https://doi.org/10.1007/JHEP02(2010)037. arXiv:0911.5299
49. G. Luisoni, P. Nason, C. Oleari, F. Tramontano, $HW^{\pm}/HZ + 0$ and 1 jet at NLO with the POWHEG BOX interfaced to GoSam and their merging within MiNLO. JHEP **10**, 083 (2013). https://doi.org/10.1007/JHEP10(2013)083. arXiv:1306.2542
50. H.B. Hartanto, B. Jager, L. Reina, D. Wackeroth, Higgs boson production in association with top quarks in the POWHEG BOX. Phys. Rev. D **91**, 094003 (2015). https://doi.org/10.1103/PhysRevD.91.094003. arXiv:1501.04498
51. J. Alwall et al., The automated computation of tree-level and next-to-leading order differential cross sections, and their matching to parton shower simulations. JHEP **07**, 079 (2014). https://doi.org/10.1007/JHEP07(2014)079. arXiv:1405.0301
52. K. Hamilton, P. Nason, E. Re, G. Zanderighi, NNLOPS simulation of Higgs boson production. JHEP **10**, 222 (2013). https://doi.org/10.1007/JHEP10(2013)222. arXiv:1309.0017
53. K. Hamilton, P. Nason, G. Zanderighi, Finite quark-mass effects in the NNLOPS POWHEG+MiNLO Higgs generator. JHEP **05**, 140 (2015). https://doi.org/10.1007/JHEP05(2015)140. arXiv:1501.04637
54. R. Frederix, K. Hamilton, Extending the MINLO method. JHEP **05**, 042 (2016). https://doi.org/10.1007/JHEP05(2016)042. arXiv:1512.02663
55. LHC Higgs Cross Section Working Group, Handbook of LHC Higgs cross sections: 4. Deciphering the nature of the Higgs sector. CERN Report CERN-2017-002-M (2016). https://doi.org/10.23731/CYRM-2017-002. arXiv:1610.07922
56. CMS Collaboration, A measurement of the Higgs boson mass in the diphoton decay channel. Phys. Lett. B **805**, 135425 (2020). https://doi.org/10.1016/j.physletb.2020.135425. arXiv:2002.06398
57. S. Bolognesi et al., On the spin and parity of a single-produced resonance at the LHC. Phys. Rev. D **86**, 095031 (2012). https://doi.org/10.1103/PhysRevD.86.095031. arXiv:1208.4018
58. P. Nason, G. Zanderighi, W^+W^-, WZ and ZZ production in the POWHEG-BOX-V2. Eur. Phys. J. C **74**, 2702 (2014). https://doi.org/10.1140/epjc/s10052-013-2702-5. arXiv:1311.1365
59. J.M. Campbell, R.K. Ellis, An update on vector boson pair production at hadron colliders. Phys. Rev. D **60**, 113006 (1999). https://doi.org/10.1103/PhysRevD.60.113006. arXiv:hep-ph/9905386
60. J.M. Campbell, R.K. Ellis, C. Williams, Vector boson pair production at the LHC. JHEP **07**, 018 (2011). https://doi.org/10.1007/JHEP07(2011)018. arXiv:1105.0020
61. J.M. Campbell, R.K. Ellis, W.T. Giele, A multi-threaded version of MCFM. Eur. Phys. J. C **75**, 246 (2015). https://doi.org/10.1140/epjc/s10052-015-3461-2. arXiv:1503.06182
62. F. Caola et al., QCD corrections to vector boson pair production in gluon fusion including interference effects with off-shell Higgs at the LHC. JHEP **07**, 087 (2016). https://doi.org/10.1007/JHEP07(2016)087. arXiv:1605.04610
63. J. Alwall et al., Comparative study of various algorithms for the merging of parton showers and matrix elements in hadronic collisions. Eur. Phys. J. C **53**, 473 (2008). https://doi.org/10.1140/epjc/s10052-007-0490-5. arXiv:0706.2569
64. S. Frixione, P. Nason, G. Ridolfi, A positive-weight next-to-leading-order Monte Carlo for heavy flavour hadroproduction. JHEP **09**, 126 (2007). https://doi.org/10.1088/1126-6708/2007/09/126. arXiv:0707.3088
65. S. Alioli, P. Nason, C. Oleari, E. Re, NLO single-top production matched with shower in POWHEG: s- and t-channel contributions. JHEP **09**, 111 (2009). https://doi.org/10.1088/1126-6708/2009/09/111. arXiv:0907.4076. [Erratum: https://doi.org/10.1007/JHEP02(2010)011]
66. E. Re, Single-top Wt-channel production matched with parton showers using the POWHEG method. Eur. Phys. J. C **71**, 1547 (2011). https://doi.org/10.1140/epjc/s10052-011-1547-z. arXiv:1009.2450
67. R. Frederix, S. Frixione, Merging meets matching in MC@NLO. JHEP **12**, 061 (2012). https://doi.org/10.1007/JHEP12(2012)061. arXiv:1209.6215
68. GEANT4 Collaboration, Geant4—a simulation toolkit. Nucl. Instrum. Methods A **506**, 250 (2003). https://doi.org/10.1016/S0168-9002(03)01368-8
69. M. Abadi et al., TensorFlow: large-scale machine learning on heterogeneous systems (2015). Software available from tensorflow.org. https://doi.org/10.5281/zenodo.5949169
70. A. Hoecker et al., TMVA 4—toolkit for multivariate data analysis with ROOT (2018). https://doi.org/10.48550/ARXIV.PHYSICS/0703039
71. CMS Collaboration, Measurements of inclusive W and Z cross sections in pp collisions at $\sqrt{s} = 7$ TeV. JHEP **01**, 080 (2011). https://doi.org/10.1007/JHEP01(2011)080. arXiv:1012.2466
72. M. Czakon et al., Top-pair production at the LHC through NNLO QCD and NLO EW. JHEP **10**, 186 (2017). https://doi.org/10.1007/JHEP10(2017)186. arXiv:1705.04105
73. P. Meade, H. Ramani, M. Zeng, Transverse momentum resummation effects in W^+W^- measurements. Phys. Rev. D **90**, 114006 (2014). https://doi.org/10.1103/PhysRevD.90.114006. arXiv:1407.4481
74. P. Jaiswal, T. Okui, Explanation of the WW excess at the LHC by jet-veto resummation. Phys. Rev. D **90**, 073009 (2014). https://doi.org/10.1103/PhysRevD.90.073009. arXiv:1407.4537
75. C.M.S. Collaboration, An embedding technique to determine $\tau\tau$ backgrounds in proton-proton collision data. JINST **14**, P06032 (2019). https://doi.org/10.1088/1748-0221/14/06/P06032. arXiv:1903.01216
76. ATLAS and CMS Collaborations, LHC Higgs Combination Group, Procedure for the LHC Higgs boson search combination in Summer 2011. Technical Report ATL-PHYS-PUB 2011-11, CMS NOTE 2011/005 (2011). http://cdsweb.cern.ch/record/1379837
77. R. Barlow, C. Beeston, Fitting using finite Monte Carlo samples. Comput. Phys. Commun. **77**, 219 (1993). https://doi.org/10.1016/0010-4655(93)90005-W
78. ATLAS Collaboration, Measurement of the inelastic proton-proton cross section at $\sqrt{s} = 13TeV$ with the ATLAS detector at the LHC. Phys. Rev. Lett. **117**, 182002 (2016). https://doi.org/10.1103/PhysRevLett.117.182002. arXiv:1606.02625
79. CMS Collaboration, Measurement of the inelastic proton-proton cross section at $\sqrt{s} = 13TeV$. JHEP **07**, 161 (2018). https://doi.org/10.1007/JHEP07(2018)161. arXiv:1802.02613
80. LHC Higgs Cross Section Working Group, Handbook of LHC Higgs cross sections: 3. Higgs properties: Report of the LHC Higgs Cross Section Working Group. CERN Report CERN-2013-004 (2013). https://doi.org/10.5170/CERN-2013-004. arXiv:1307.1347

CMS Collaboration

Yerevan Physics Institute, Yerevan, Armenia
A. Tumasyan[1]

Institut für Hochenergiephysik, Vienna, Austria
W. Adam, J. W. Andrejkovic, T. Bergauer, S. Chatterjee, K. Damanakis, M. Dragicevic, A. Escalante Del Valle, P. S. Hussain, M. Jeitler[2], N. Krammer, L. Lechner, D. Liko, I. Mikulec, P. Paulitsch, F. M. Pitters, J. Schieck[2], R. Schöfbeck, D. Schwarz, S. Templ, W. Waltenberger, C.-E. Wulz[2]

Universiteit Antwerpen, Antwerpen, Belgium
M. R. Darwish[3], T. Janssen, T. Kello[4], H. Rejeb Sfar, P. Van Mechelen

Vrije Universiteit Brussel, Brussels, Belgium
E. S. Bols, J. D'Hondt, A. De Moor, M. Delcourt, H. El Faham, S. Lowette, S. Moortgat, A. Morton, D. Müller, A. R. Sahasransu, S. Tavernier, W. Van Doninck, D. Vannerom

Université Libre de Bruxelles, Brussels, Belgium
B. Clerbaux, G. De Lentdecker, L. Favart, D. Hohov, J. Jaramillo, K. Lee, M. Mahdavikhorrami, I. Makarenko, A. Malara, S. Paredes, L. Pétré, N. Postiau, E. Starling, L. Thomas, M. Vanden Bemden, C. Vander Velde, P. Vanlaer

Ghent University, Ghent, Belgium
D. Dobur, J. Knolle, L. Lambrecht, G. Mestdach, M. Niedziela, C. Rendón, C. Roskas, A. Samalan, K. Skovpen, M. Tytgat, N. Van Den Bossche, B. Vermassen, L. Wezenbeek

Université Catholique de Louvain, Louvain-la-Neuve, Belgium
A. Benecke, G. Bruno, F. Bury, C. Caputo, P. David, C. Delaere, I. S. Donertas, A. Giammanco, K. Jaffel, Sa. Jain, V. Lemaitre, K. Mondal, J. Prisciandaro, A. Taliercio, T. T. Tran, P. Vischia, S. Wertz

Centro Brasileiro de Pesquisas Fisicas, Rio de Janeiro, Brazil
G. A. Alves, E. Coelho, C. Hensel, A. Moraes, P. Rebello Teles

Universidade do Estado do Rio de Janeiro, Rio de Janeiro, Brazil
W. L. Aldá Júnior, M. Alves Gallo Pereira, M. Barroso Ferreira Filho, H. Brandao Malbouisson, W. Carvalho, J. Chinellato[5], E. M. Da Costa, G. G. Da Silveira[6], D. De Jesus Damiao, V. Dos Santos Sousa, S. Fonseca De Souza, J. Martins[7], C. Mora Herrera, K. Mota Amarilo, L. Mundim, H. Nogima, A. Santoro, S. M. Silva Do Amaral, A. Sznajder, M. Thiel, F. Torres Da Silva De Araujo[8], A. Vilela Pereira

Universidade Estadual Paulista, Universidade Federal do ABC, São Paulo, Brazil
C. A. Bernardes[6], L. Calligaris, T. R. Fernandez Perez Tomei, E. M. Gregores, P. G. Mercadante, S. F. Novaes, Sandra S. Padula

Institute for Nuclear Research and Nuclear Energy, Bulgarian Academy of Sciences, Sofia, Bulgaria
A. Aleksandrov, G. Antchev, R. Hadjiiska, P. Iaydjiev, M. Misheva, M. Rodozov, M. Shopova, G. Sultanov

University of Sofia, Sofia, Bulgaria
A. Dimitrov, T. Ivanov, L. Litov, B. Pavlov, P. Petkov, A. Petrov, E. Shumka

Instituto De Alta Investigación, Universidad de Tarapacá, Casilla 7 D, Arica, Chile
S. Thakur

Beihang University, Beijing, China
T. Cheng, T. Javaid[9], M. Mittal, L. Yuan

Department of Physics, Tsinghua University, Beijing, China
M. Ahmad, G. Bauer[10], Z. Hu, S. Lezki, K. Yi[10,11]

Institute of High Energy Physics, Beijing, China
G. M. Chen[9], H. S. Chen[9], M. Chen[9], F. Iemmi, C. H. Jiang, A. Kapoor, H. Liao, Z.-A. Liu[12], V. Milosevic, F. Monti, R. Sharma, J. Tao, J. Thomas-Wilsker, J. Wang, H. Zhang, J. Zhao

State Key Laboratory of Nuclear Physics and Technology, Peking University, Beijing, China
A. Agapitos, Y. An, Y. Ban, C. Chen, A. Levin, C. Li, Q. Li, X. Lyu, Y. Mao, S. J. Qian, X. Sun, D. Wang, J. Xiao, H. Yang

Sun Yat-Sen University, Guangzhou, China
M. Lu, Z. You

Institute of Modern Physics and Key Laboratory of Nuclear Physics and Ion-beam Application (MOE)-Fudan University, Shanghai, China
X. Gao[4], D. Leggat, H. Okawa, Y. Zhang

Zhejiang University, Hangzhou, Zhejiang, China
Z. Lin, C. Lu, M. Xiao

Universidad de Los Andes, Bogotá, Colombia
C. Avila, D. A. Barbosa Trujillo, A. Cabrera, C. Florez, J. Fraga

Universidad de Antioquia, Medellin, Colombia
J. Mejia Guisao, F. Ramirez, M. Rodriguez, J. D. Ruiz Alvarez

Faculty of Electrical Engineering, Mechanical Engineering and Naval Architecture, University of Split, Split, Croatia
D. Giljanovic, N. Godinovic, D. Lelas, I. Puljak

Faculty of Science, University of Split, Split, Croatia
Z. Antunovic, M. Kovac, T. Sculac

Institute Rudjer Boskovic, Zagreb, Croatia
V. Brigljevic, B. K. Chitroda, D. Ferencek, D. Majumder, M. Roguljic, A. Starodumov[13], T. Susa

University of Cyprus, Nicosia, Cyprus
A. Attikis, K. Christoforou, G. Kole, M. Kolosova, S. Konstantinou, J. Mousa, C. Nicolaou, F. Ptochos, P. A. Razis, H. Rykaczewski, H. Saka

Charles University, Prague, Czech Republic
M. Finger[13], M. Finger Jr.[13], A. Kveton

Escuela Politecnica Nacional, Quito, Ecuador
E. Ayala

Universidad San Francisco de Quito, Quito, Ecuador
E. Carrera Jarrin

Academy of Scientific Research and Technology of the Arab Republic of Egypt, Egyptian Network of High Energy Physics, Cairo, Egypt
A. A. Abdelalim[14,15], E. Salama[16,17]

Center for High Energy Physics (CHEP-FU), Fayoum University, El-Fayoum, Egypt
M. Abdullah Al-Mashad, M. A. Mahmoud

National Institute of Chemical Physics and Biophysics, Tallinn, Estonia
S. Bhowmik, R. K. Dewanjee, K. Ehataht, M. Kadastik, T. Lange, S. Nandan, C. Nielsen, J. Pata, M. Raidal, L. Tani, C. Veelken

Department of Physics, University of Helsinki, Helsinki, Finland
P. Eerola, H. Kirschenmann, K. Osterberg, M. Voutilainen

Helsinki Institute of Physics, Helsinki, Finland
S. Bharthuar, E. Brücken, F. Garcia, J. Havukainen, M. S. Kim, R. Kinnunen, T. Lampén,

K. Lassila-Perini, S. Lehti, T. Lindén, M. Lotti, L. Martikainen, M. Myllymäki, J. Ott, M. M. Rantanen, H. Siikonen, E. Tuominen, J. Tuominiemi

Lappeenranta-Lahti University of Technology, Lappeenranta, Finland
P. Luukka, H. Petrow, T. Tuuva

IRFU, CEA, Université Paris-Saclay, Gif-sur-Yvette, France
C. Amendola, M. Besancon, F. Couderc, M. Dejardin, D. Denegri, J. L. Faure, F. Ferri, S. Ganjour, P. Gras, G. Hamel de Monchenault, P. Jarry, V. Lohezic, J. Malcles, J. Rander, A. Rosowsky, M.Ö. Sahin, A. Savoy-Navarro[18], P. Simkina, M. Titov

Laboratoire Leprince-Ringuet, CNRS/IN2P3, Ecole Polytechnique, Institut Polytechnique de Paris, Palaiseau, France
C. Baldenegro Barrera, F. Beaudette, A. Buchot Perraguin, P. Busson, A. Cappati, C. Charlot, F. Damas, O. Davignon, B. Diab, G. Falmagne, B. A. Fontana Santos Alves, S. Ghosh, R. Granier de Cassagnac, A. Hakimi, B. Harikrishnan, G. Liu, J. Motta, M. Nguyen, C. Ochando, L. Portales, R. Salerno, U. Sarkar, J. B. Sauvan, Y. Sirois, A. Tarabini, E. Vernazza, A. Zabi, A. Zghiche

Université de Strasbourg, CNRS, IPHC UMR 7178, Strasbourg, France
J.-L. Agram[19], J. Andrea, D. Apparu, D. Bloch, G. Bourgatte, J.-M. Brom, E. C. Chabert, C. Collard, D. Darej, U. Goerlach, C. Grimault, A.-C. Le Bihan, P. Van Hove

Institut de Physique des 2 Infinis de Lyon (IP2I), Villeurbanne, France
S. Beauceron, C. Bernet, B. Blancon, G. Boudoul, A. Carle, N. Chanon, J. Choi, D. Contardo, P. Depasse, C. Dozen[20], H. El Mamouni, J. Fay, S. Gascon, M. Gouzevitch, G. Grenier, B. Ille, I. B. Laktineh, M. Lethuillier, L. Mirabito, S. Perries, L. Torterotot, M. Vander Donckt, P. Verdier, S. Viret

Georgian Technical University, Tbilisi, Georgia
I. Bagaturia[21], I. Lomidze, Z. Tsamalaidze[13]

RWTH Aachen University, I. Physikalisches Institut, Aachen, Germany
V. Botta, L. Feld, K. Klein, M. Lipinski, D. Meuser, A. Pauls, N. Röwert, M. Teroerde

RWTH Aachen University, III. Physikalisches Institut A, Aachen, Germany
S. Diekmann, A. Dodonova, N. Eich, D. Eliseev, M. Erdmann, P. Fackeldey, D. Fasanella, B. Fischer, T. Hebbeker, K. Hoepfner, F. Ivone, M.y. Lee, L. Mastrolorenzo, M. Merschmeyer, A. Meyer, S. Mondal, S. Mukherjee, D. Noll, A. Novak, F. Nowotny, A. Pozdnyakov, Y. Rath, W. Redjeb, H. Reithler, A. Schmidt, S. C. Schuler, A. Sharma, L. Vigilante, S. Wiedenbeck, S. Zaleski

RWTH Aachen University, III. Physikalisches Institut B, Aachen, Germany
C. Dziwok, G. Flügge, W. Haj Ahmad[22], O. Hlushchenko, T. Kress, A. Nowack, O. Pooth, A. Stahl, T. Ziemons, A. Zotz

Deutsches Elektronen-Synchrotron, Hamburg, Germany
H. Aarup Petersen, M. Aldaya Martin, P. Asmuss, S. Baxter, M. Bayatmakou, O. Behnke, A. Bermúdez Martínez, S. Bhattacharya, A. A. Bin Anuar, F. Blekman[23], K. Borras[24], D. Brunner, A. Campbell, A. Cardini, C. Cheng, F. Colombina, S. Consuegra Rodríguez, G. Correia Silva, M. De Silva, L. Didukh, G. Eckerlin, D. Eckstein, L. I. Estevez Banos, O. Filatov, E. Gallo[23], A. Geiser, A. Giraldi, G. Greau, A. Grohsjean, V. Guglielmi, M. Guthoff, A. Jafari[25], N. Z. Jomhari, B. Kaech, A. Kasem[24], M. Kasemann, H. Kaveh, C. Kleinwort, R. Kogler, M. Komm, D. Krücker, W. Lange, D. Leyva Pernia, K. Lipka, W. Lohmann[26], R. Mankel, I.-A. Melzer-Pellmann, M. Mendizabal Morentin, J. Metwally, A. B. Meyer, G. Milella, M. Mormile, A. Mussgiller, A. Nürnberg, Y. Otarid, D. Pérez Adán, A. Raspereza, B. Ribeiro Lopes, J. Rübenach, A. Saggio, A. Saibel, M. Savitskyi, M. Scham[24,27], V. Scheurer, S. Schnake[24], P. Schütze, C. Schwanenberger[23], M. Shchedrolosiev, R. E. Sosa Ricardo, D. Stafford, N. Tonon[†], M. Van De Klundert, F. Vazzoler, A. Ventura Barroso, R. Walsh, D. Walter, Q. Wang, Y. Wen, K. Wichmann, L. Wiens[24], C. Wissing, S. Wuchterl, Y. Yang, A. Zimermmane Castro Santos

University of Hamburg, Hamburg, Germany
A. Albrecht, S. Albrecht, M. Antonello, S. Bein, L. Benato, M. Bonanomi, P. Connor, K. De Leo, M. Eich, K. El Morabit, F. Feindt, A. Fröhlich, C. Garbers, E. Garutti, M. Hajheidari, J. Haller, A. Hinzmann, H. R. Jabusch, G. Kasieczka, R. Klanner, W. Korcari, T. Kramer, V. Kutzner, J. Lange, A. Lobanov, C. Matthies, A. Mehta, L. Moureaux, M. Mrowietz, A. Nigamova, Y. Nissan, A. Paasch, K. J. Pena Rodriguez, M. Rieger, O. Rieger, P. Schleper, M. Schröder, J. Schwandt, H. Stadie, G. Steinbrück, A. Tews, M. Wolf

Karlsruher Institut fuer Technologie, Karlsruhe, Germany
J. Bechtel, S. Brommer, M. Burkart, E. Butz, R. Caspart, T. Chwalek, A. Dierlamm, A. Droll, N. Faltermann, M. Giffels, J. O. Gosewisch, A. Gottmann, F. Hartmann[28], M. Horzela, U. Husemann, P. Keicher, M. Klute, R. Koppenhöfer, S. Maier, S. Mitra, Th. Müller, M. Neukum, G. Quast, K. Rabbertz, J. Rauser, D. Savoiu, M. Schnepf, D. Seith, I. Shvetsov, H. J. Simonis, N. Trevisani, R. Ulrich, J. van der Linden, R. F. Von Cube, M. Wassmer, S. Wieland, R. Wolf, S. Wozniewski, S. Wunsch, X. Zuo

Institute of Nuclear and Particle Physics (INPP), NCSR Demokritos, Aghia Paraskevi, Greece
G. Anagnostou, P. Assiouras, G. Daskalakis, A. Kyriakis, A. Stakia

National and Kapodistrian University of Athens, Athens, Greece
M. Diamantopoulou, D. Karasavvas, P. Kontaxakis, A. Manousakis-Katsikakis, A. Panagiotou, I. Papavergou, N. Saoulidou, K. Theofilatos, E. Tziaferi, K. Vellidis, E. Vourliotis, I. Zisopoulos

National Technical University of Athens, Athens, Greece
G. Bakas, T. Chatzistavrou, K. Kousouris, I. Papakrivopoulos, G. Tsipolitis, A. Zacharopoulou

University of Ioánnina, Ioannina, Greece
K. Adamidis, I. Bestintzanos, I. Evangelou, C. Foudas, P. Gianneios, C. Kamtsikis, P. Katsoulis, P. Kokkas, P. G. Kosmoglou Kioseoglou, N. Manthos, I. Papadopoulos, J. Strologas

MTA-ELTE Lendület CMS Particle and Nuclear Physics Group, Eötvös Loránd University, Budapest, Hungary
M. Csanád, K. Farkas, M. M. A. Gadallah[29], S. Lökös[30], P. Major, K. Mandal, G. Pásztor, A. J. Rádl[31], O. Surányi, G. I. Veres

Wigner Research Centre for Physics, Budapest, Hungary
M. Bartók[32], G. Bencze, C. Hajdu, D. Horvath[33,34], F. Sikler, V. Veszpremi

Institute of Nuclear Research ATOMKI, Debrecen, Hungary
N. Beni, S. Czellar, J. Karancsi[32], J. Molnar, Z. Szillasi, D. Teyssier

Institute of Physics, University of Debrecen, Debrecen, Hungary
P. Raics, B. Ujvari[35]

Karoly Robert Campus, MATE Institute of Technology, Gyongyos, Hungary
T. Csorgo[31], F. Nemes[31], T. Novak

Panjab University, Chandigarh, India
J. Babbar, S. Bansal, S. B. Beri, V. Bhatnagar, G. Chaudhary, S. Chauhan, N. Dhingra[36], R. Gupta, A. Kaur, A. Kaur, H. Kaur, M. Kaur, S. Kumar, P. Kumari, M. Meena, K. Sandeep, T. Sheokand, J. B. Singh[37], A. Singla, A. K. Virdi

University of Delhi, Delhi, India
A. Ahmed, A. Bhardwaj, B. C. Choudhary, M. Gola, A. Kumar, M. Naimuddin, P. Priyanka, K. Ranjan, S. Saumya, A. Shah

Saha Institute of Nuclear Physics, HBNI, Kolkata, India
S. Baradia, S. Barman[38], S. Bhattacharya, D. Bhowmik, S. Dutta, S. Dutta, B. Gomber[39], M. Maity[38], P. Palit, P. K. Rout, G. Saha, B. Sahu, S. Sarkar

Indian Institute of Technology Madras, Madras, India
P. K. Behera, S. C. Behera, P. Kalbhor, J. R. Komaragiri[40], D. Kumar[40], A. Muhammad, L. Panwar[40], R. Pradhan, P. R. Pujahari, A. Sharma, A. K. Sikdar, P. C. Tiwari[40], S. Verma

Bhabha Atomic Research Centre, Mumbai, India
K. Naskar[41]

Tata Institute of Fundamental Research-A, Mumbai, India
T. Aziz, I. Das, S. Dugad, M. Kumar, G. B. Mohanty, P. Suryadevara

Tata Institute of Fundamental Research-B, Mumbai, India
S. Banerjee, R. Chudasama, M. Guchait, S. Karmakar, S. Kumar, G. Majumder, K. Mazumdar, S. Mukherjee, A. Thachayath

National Institute of Science Education and Research, An OCC of Homi Bhabha National Institute, Bhubaneswar, Odisha, India
S. Bahinipati[42], A. K. Das, C. Kar, P. Mal, T. Mishra, V. K. Muraleedharan Nair Bindhu[43], A. Nayak[43], P. Saha, S. K. Swain, D. Vats[43]

Indian Institute of Science Education and Research (IISER), Pune, India
A. Alpana, S. Dube, B. Kansal, A. Laha, S. Pandey, A. Rastogi, S. Sharma

Isfahan University of Technology, Isfahan, Iran
H. Bakhshiansohi[44], E. Khazaie, M. Zeinali[45]

Institute for Research in Fundamental Sciences (IPM), Tehran, Iran
S. Chenarani[46], S. M. Etesami, M. Khakzad, M. Mohammadi Najafabadi

University College Dublin, Dublin, Ireland
M. Grunewald

INFN Sezione di Bari[a], Università di Bari[b], Politecnico di Bari[c], Bari, Italy
M. Abbrescia[a,b], R. Aly[a,c,14], C. Aruta[a,b], A. Colaleo[a], D. Creanza[a,c], N. De Filippis[a,c], M. De Palma[a,b], A. Di Florio[a,b], W. Elmetenawee[a,b], F. Errico[a,b], L. Fiore[a], G. Iaselli[a,c], M. Ince[a,b], G. Maggi[a,c], M. Maggi[a], I. Margjeka[a,b], V. Mastrapasqua[a,b], S. My[a,b], S. Nuzzo[a,b], A. Pellecchia[a,b], A. Pompili[a,b], G. Pugliese[a,c], R. Radogna[a], D. Ramos[a], A. Ranieri[a], G. Selvaggi[a,b], L. Silvestris[a], F. M. Simone[a,b], Ü. Sözbilir[a], A. Stamerra[a], R. Venditti[a], P. Verwilligen[a]

INFN Sezione di Bologna[a], Università di Bologna[b], Bologna, Italy
G. Abbiendi[a], C. Battilana[a,b], D. Bonacorsi[a,b], L. Borgonovi[a], L. Brigliadori[a], R. Campanini[a,b], P. Capiluppi[a,b], A. Castro[a,b], F. R. Cavallo[a], M. Cuffiani[a,b], G. M. Dallavalle[a], T. Diotalevi[a,b], F. Fabbri[a], A. Fanfani[a,b], P. Giacomelli[a], L. Giommi[a,b], C. Grandi[a], L. Guiducci[a,b], S. Lo Meo[a,47], L. Lunerti[a,b], S. Marcellini[a], G. Masetti[a], F. L. Navarria[a,b], A. Perrotta[a], F. Primavera[a,b], A. M. Rossi[a,b], T. Rovelli[a,b], G. P. Siroli[a,b]

INFN Sezione di Catania[a], Università di Catania[b], Catania, Italy
S. Costa[a,b,48], A. Di Mattia[a], R. Potenza[a,b], A. Tricomi[a,b,48], C. Tuve[a,b]

INFN Sezione di Firenze[a], Università di Firenze[b], Firenze, Italy
G. Barbagli[a], B. Camaiani[a,b], A. Cassese[a], R. Ceccarelli[a,b], V. Ciulli[a,b], C. Civinini[a], R. D'Alessandro[a,b], E. Focardi[a,b], G. Latino[a,b], P. Lenzi[a,b], M. Lizzo[a,b], M. Meschini[a], S. Paoletti[a], R. Seidita[a,b], G. Sguazzoni[a], L. Viliani[a]

INFN Laboratori Nazionali di Frascati, Frascati, Italy
L. Benussi, S. Bianco, S. Meola[28], D. Piccolo

INFN Sezione di Genova[a], Università di Genova[b], Genoa, Italy
M. Bozzo[a,b], P. Chatagnon[a], F. Ferro[a], R. Mulargia[a], E. Robutti[a], S. Tosi[a,b]

INFN Sezione di Milano-Bicocca[a], Università di Milano-Bicocca[b], Milan, Italy
A. Benaglia[a], G. Boldrini[a], F. Brivio[a,b], F. Cetorelli[a,b], F. De Guio[a,b], M. E. Dinardo[a,b], P. Dini[a], S. Gennai[a], A. Ghezzi[a,b], P. Govoni[a,b], L. Guzzi[a,b], M. T. Lucchini[a,b], M. Malberti[a], S. Malvezzi[a], A. Massironi[a], D. Menasce[a], L. Moroni[a], M. Paganoni[a,b], D. Pedrini[a], B. S. Pinolini[a], S. Ragazzi[a,b], N. Redaelli[a], T. Tabarelli de Fatis[a,b], D. Zuolo[a,b]

INFN Sezione di Napoli[a], Università di Napoli 'Federico II'[b], Naples, Italy; Università della Basilicata[c], Potenza, Italy; Università G. Marconi[d], Rome, Italy
S. Buontempo[a], F. Carnevali[a,b], N. Cavallo[a,c], A. De Iorio[a,b], F. Fabozzi[a,c], A. O. M. Iorio[a,b], L. Lista[a,b,49], P. Paolucci[a,28], B. Rossi[a], C. Sciacca[a,b]

INFN Sezione di Padova[a], Università di Padova[b], Padua, Italy; Università di Trento[c], Trento, Italy
P. Azzi[a], N. Bacchetta[a,50], M. Biasotto[a,51], D. Bisello[a,b], P. Bortignon[a], A. Bragagnolo[a,b], R. Carlin[a,b], P. Checchia[a], T. Dorigo[a], F. Gasparini[a,b], U. Gasparini[a,b], G. Grosso[a], L. Layer[a,52], E. Lusiani[a], M. Margoni[a,b], J. Pazzini[a,b], P. Ronchese[a,b], R. Rossin[a,b], F. Simonetto[a,b], G. Strong[a], M. Tosi[a,b], H. Yarar[a,b], M. Zanetti[a,b], P. Zotto[a,b], A. Zucchetta[a,b], G. Zumerle[a,b]

INFN Sezione di Pavia[a], Università di Pavia[b], Pavia, Italy
S. Abu Zeid[a,17], C. Aimè[a,b], A. Braghieri[a], S. Calzaferri[a,b], D. Fiorina[a,b], P. Montagna[a,b], V. Re[a], C. Riccardi[a,b], P. Salvini[a], I. Vai[a], P. Vitulo[a,b]

INFN Sezione di Perugia[a], Università di Perugia[b], Perugia, Italy
P. Asenov[a,53], G. M. Bilei[a], D. Ciangottini[a,b], L. Fanò[a,b], M. Magherini[a,b], G. Mantovani[a,b], V. Mariani[a,b], M. Menichelli[a], F. Moscatelli[a,53], A. Piccinelli[a,b], M. Presilla[a,b], A. Rossi[a,b], A. Santocchia[a,b], D. Spiga[a], T. Tedeschi[a,b]

INFN Sezione di Pisa[a], Università di Pisa[b], Scuola Normale Superiore di Pisa[c], Pisa, Italy; Università di Siena[d], Siena, Italy
P. Azzurri[a], G. Bagliesi[a], V. Bertacchi[a,c], R. Bhattacharya[a], L. Bianchini[a,b], T. Boccali[a], E. Bossini[a,b], D. Bruschini[a,c], R. Castaldi[a], M. A. Ciocci[a,b], V. D'Amante[a,d], R. Dell'Orso[a], M. R. Di Domenico[a,d], S. Donato[a], A. Giassi[a], F. Ligabue[a,c], G. Mandorli[a,c], D. Matos Figueiredo[a], A. Messineo[a,b], M. Musich[a,b], F. Palla[a], S. Parolia[a,b], G. Ramirez-Sanchez[a,c], A. Rizzi[a,b], G. Rolandi[a,c], S. Roy Chowdhury[a], T. Sarkar[a], A. Scribano[a], N. Shafiei[a,b], P. Spagnolo[a], R. Tenchini[a], G. Tonelli[a,b], N. Turini[a,d], A. Venturi[a], P. G. Verdini[a]

INFN Sezione di Roma[a], Sapienza Università di Roma[b], Rome, Italy
P. Barria[a], M. Campana[a,b], F. Cavallari[a], D. Del Re[a,b], E. Di Marco[a], M. Diemoz[a], E. Longo[a,b], P. Meridiani[a], G. Organtini[a,b], F. Pandolfi[a], R. Paramatti[a,b], C. Quaranta[a,b], S. Rahatlou[a,b], C. Rovelli[a], F. Santanastasio[a,b], L. Soffi[a], R. Tramontano[a,b]

INFN Sezione di Torino[a], Università di Torino[b], Turin, Italy; Università del Piemonte Orientale[c], Novara, Italy
N. Amapane[a,b], R. Arcidiacono[a,c], S. Argiro[a,b], M. Arneodo[a,c], N. Bartosik[a], R. Bellan[a,b], A. Bellora[a,b], C. Biino[a], N. Cartiglia[a], M. Costa[a,b], R. Covarelli[a,b], N. Demaria[a], M. Grippo[a,b], B. Kiani[a,b], F. Legger[a], C. Mariotti[a], S. Maselli[a], A. Mecca[a,b], E. Migliore[a,b], E. Monteil[a,b], M. Monteno[a], M. M. Obertino[a,b], G. Ortona[a], L. Pacher[a,b], N. Pastrone[a], M. Pelliccioni[a], M. Ruspa[a,c], K. Shchelina[a], F. Siviero[a,b], V. Sola[a], A. Solano[a,b], D. Soldi[a,b], A. Staiano[a], M. Tornago[a,b], D. Trocino[a], G. Umoret[a,b], A. Vagnerini[a,b]

INFN Sezione di Trieste[a], Università di Trieste[b], Trieste, Italy
S. Belforte[a], V. Candelise[a,b], M. Casarsa[a], F. Cossutti[a], A. Da Rold[a,b], G. Della Ricca[a,b], G. Sorrentino[a,b]

Kyungpook National University, Daegu, Korea
S. Dogra, C. Huh, B. Kim, D. H. Kim, G. N. Kim, J. Kim, J. Lee, S. W. Lee, C. S. Moon, Y. D. Oh, S. I. Pak, M. S. Ryu, S. Sekmen, Y. C. Yang

Chonnam National University, Institute for Universe and Elementary Particles, Kwangju, Korea
H. Kim, D. H. Moon

Hanyang University, Seoul, South Korea
E. Asilar, T. J. Kim, J. Park

Korea University, Seoul, South Korea
S. Choi, S. Han, B. Hong, K. Lee, K. S. Lee, J. Lim, J. Park, S. K. Park, J. Yoo

Kyung Hee University, Department of Physics, Seoul, South Korea
J. Goh

Sejong University, Seoul, South Korea
H. S. Kim, Y. Kim, S. Lee

Seoul National University, Seoul, South Korea
J. Almond, J. H. Bhyun, J. Choi, S. Jeon, W. Jun, J. Kim, J. Kim, J. S. Kim, S. Ko, H. Kwon, H. Lee, J. Lee, S. Lee, B. H. Oh, M. Oh, S. B. Oh, H. Seo, U. K. Yang, I. Yoon

University of Seoul, Seoul, South Korea
W. Jang, D. Y. Kang, Y. Kang, D. Kim, S. Kim, B. Ko, J. S. H. Lee, Y. Lee, J. A. Merlin, I. C. Park, Y. Roh, D. Song, I. J. Watson, S. Yang

Department of Physics, Yonsei University, Seoul, South Korea
S. Ha, H. D. Yoo

Sungkyunkwan University, Suwon, South Korea
M. Choi, M. R. Kim, H. Lee, Y. Lee, Y. Lee, I. Yu

College of Engineering and Technology, American University of the Middle East (AUM), Dasman, Kuwait
T. Beyrouthy, Y. Maghrbi

Riga Technical University, Riga, Latvia
K. Dreimanis, A. Gaile, A. Potrebko, M. Seidel, T. Torims, V. Veckalns

Vilnius University, Vilnius, Lithuania
M. Ambrozas, A. Carvalho Antunes De Oliveira, A. Juodagalvis, A. Rinkevicius, G. Tamulaitis

National Centre for Particle Physics, Universiti Malaya, Kuala Lumpur, Malaysia
N. Bin Norjoharuddeen, S. Y. Hoh[54], I. Yusuff[54], Z. Zolkapli

Universidad de Sonora (UNISON), Hermosillo, Mexico
J. F. Benitez, A. Castaneda Hernandez, H. A. Encinas Acosta, L. G. Gallegos Maríñez, M. León Coello, J. A. Murillo Quijada, A. Sehrawat, L. Valencia Palomo

Centro de Investigacion y de Estudios Avanzados del IPN, Mexico, Mexico
G. Ayala, H. Castilla-Valdez, I. Heredia-De La Cruz[55], R. Lopez-Fernandez, C. A. Mondragon Herrera, D. A. Perez Navarro, A. Sánchez Hernández

Universidad Iberoamericana, Mexico, Mexico
C. Oropeza Barrera, F. Vazquez Valencia

Benemerita Universidad Autonoma de Puebla, Puebla, Mexico
I. Pedraza, H. A. Salazar Ibarguen, C. Uribe Estrada

University of Montenegro, Podgorica, Montenegro
I. Bubanja, J. Mijuskovic[56], N. Raicevic

National Centre for Physics, Quaid-I-Azam University, Islamabad, Pakistan
A. Ahmad, M. I. Asghar, A. Awais, M. I. M. Awan, M. Gul, H. R. Hoorani, W. A. Khan, M. Shoaib, M. Waqas

Faculty of Computer Science, Electronics and Telecommunications, AGH University of Science and Technology, Kraków, Poland
V. Avati, L. Grzanka, M. Malawski

National Centre for Nuclear Research, Swierk, Poland
H. Bialkowska, M. Bluj, B. Boimska, M. Górski, M. Kazana, M. Szleper, P. Zalewski

Institute of Experimental Physics, Faculty of Physics, University of Warsaw, Warsaw, Poland
K. Bunkowski, K. Doroba, A. Kalinowski, M. Konecki, J. Krolikowski

Laboratório de Instrumentação e Física Experimental de Partículas, Lisbon, Portugal
M. Araujo, P. Bargassa, D. Bastos, A. Boletti, P. Faccioli, M. Gallinaro, J. Hollar, N. Leonardo, T. Niknejad, M. Pisano, J. Seixas, J. Varela

VINCA Institute of Nuclear Sciences, University of Belgrade, Belgrade, Serbia
P. Adzic[57], M. Dordevic, P. Milenovic, J. Milosevic

Centro de Investigaciones Energéticas Medioambientales y Tecnológicas (CIEMAT), Madrid, Spain
M. Aguilar-Benitez, J. Alcaraz Maestre, A. Álvarez Fernández, M. Barrio Luna, Cristina F. Bedoya, C. A. Carrillo Montoya, M. Cepeda, M. Cerrada, N. Colino, B. De La Cruz, A. Delgado Peris, D. Fernández Del Val, J. P. Fernández Ramos, J. Flix, M. C. Fouz, O. Gonzalez Lopez, S. Goy Lopez, J. M. Hernandez, M. I. Josa, J. León Holgado, D. Moran, C. Perez Dengra, A. Pérez-Calero Yzquierdo, J. Puerta Pelayo, I. Redondo, D. D. Redondo Ferrero, L. Romero, S. Sánchez Navas, J. Sastre, L. Urda Gómez, J. Vazquez Escobar, C. Willmott

Universidad Autónoma de Madrid, Madrid, Spain
J. F. de Trocóniz

Instituto Universitario de Ciencias y Tecnologías Espaciales de Asturias (ICTEA), Universidad de Oviedo, Oviedo, Spain
B. Alvarez Gonzalez, J. Cuevas, J. Fernandez Menendez, S. Folgueras, I. Gonzalez Caballero, J. R. González Fernández, E. Palencia Cortezon, C. Ramón Álvarez, V. Rodríguez Bouza, A. Soto Rodríguez, A. Trapote, C. Vico Villalba

Instituto de Física de Cantabria (IFCA), CSIC-Universidad de Cantabria, Santander, Spain
J. A. Brochero Cifuentes, I. J. Cabrillo, A. Calderon, J. Duarte Campderros, M. Fernandez, C. Fernandez Madrazo, A. García Alonso, G. Gomez, C. Lasaosa García, C. Martinez Rivero, P. Martinez Ruiz del Arbol, F. Matorras, P. Matorras Cuevas, J. Piedra Gomez, C. Prieels, A. Ruiz-Jimeno, L. Scodellaro, I. Vila, J. M. Vizan Garcia

University of Colombo, Colombo, Sri Lanka
M. K. Jayananda, B. Kailasapathy[58], D. U. J. Sonnadara, D. D. C. Wickramarathna

University of Ruhuna, Department of Physics, Matara, Sri Lanka
W. G. D. Dharmaratna, K. Liyanage, N. Perera, N. Wickramage

CERN, European Organization for Nuclear Research, Geneva, Switzerland
D. Abbaneo, J. Alimena, E. Auffray, G. Auzinger, J. Baechler, P. Baillon[†], D. Barney, J. Bendavid, M. Bianco, B. Bilin, A. Bocci, E. Brondolin, C. Caillol, T. Camporesi, G. Cerminara, N. Chernyavskaya, S. S. Chhibra, S. Choudhury, M. Cipriani, L. Cristella, D. d'Enterria, A. Dabrowski, A. David, A. De Roeck, M. M. Defranchis, M. Deile, M. Dobson, M. Dünser, N. Dupont, A. Elliott-Peisert, F. Fallavollita[59], A. Florent, L. Forthomme, G. Franzoni, W. Funk, S. Ghosh, S. Giani, D. Gigi, K. Gill, F. Glege, L. Gouskos, E. Govorkova, M. Haranko, J. Hegeman, V. Innocente, T. James, P. Janot, J. Kaspar, J. Kieseler, N. Kratochwil, S. Laurila, P. Lecoq, E. Leutgeb, A. Lintuluoto, C. Lourenço, B. Maier, L. Malgeri, M. Mannelli, A. C. Marini, F. Meijers, S. Mersi, E. Meschi, F. Moortgat, M. Mulders, S. Orfanelli, L. Orsini, F. Pantaleo, E. Perez, M. Peruzzi, A. Petrilli, G. Petrucciani, A. Pfeiffer, M. Pierini, D. Piparo, M. Pitt, H. Qu, T. Quast, D. Rabady, A. Racz, G. Reales Gutiérrez, M. Rovere, H. Sakulin, J. Salfeld-Nebgen, S. Scarfi, M. Selvaggi, A. Sharma, P. Silva, P. Sphicas[60], A. G. Stahl Leiton, S. Summers, K. Tatar, V. R. Tavolaro, D. Treille, P. Tropea, A. Tsirou, J. Wanczyk[61], K. A. Wozniak, W. D. Zeuner

Paul Scherrer Institut, Villigen, Switzerland
L. Caminada[62], A. Ebrahimi, W. Erdmann, R. Horisberger, Q. Ingram, H. C. Kaestli, D. Kotlinski, C. Lange, M. Missiroli[62], L. Noehte[62], T. Rohe

ETH Zurich-Institute for Particle Physics and Astrophysics (IPA), Zurich, Switzerland
T. K. Aarrestad, K. Androsov[61], M. Backhaus, P. Berger, A. Calandri, K. Datta, A. De Cosa, G. Dissertori, M. Dittmar, M. Donegà, F. Eble, M. Galli, K. Gedia, F. Glessgen, T. A. Gómez Espinosa, C. Grab, D. Hits, W. Lustermann, A.-M. Lyon, R. A. Manzoni, L. Marchese, C. Martin Perez, A. Mascellani[61], M. T. Meinhard, F. Nessi-Tedaldi, J. Niedziela, F. Pauss, V. Perovic, S. Pigazzini, M. G. Ratti, M. Reichmann, C. Reissel, T. Reitenspiess, B. Ristic, F. Riti, D. Ruini, D. A. Sanz Becerra, J. Steggemann[61], D. Valsecchi[28], R. Wallny

Universität Zürich, Zurich, Switzerland
C. Amsler[63], P. Bärtschi, C. Botta, D. Brzhechko, M. F. Canelli, K. Cormier, A. De Wit, R. Del Burgo, J. K. Heikkilä, M. Huwiler, W. Jin, A. Jofrehei, B. Kilminster, S. Leontsinis, S. P. Liechti, A. Macchiolo, P. Meiring, V. M. Mikuni, U. Molinatti, I. Neutelings, A. Reimers, P. Robmann, S. Sanchez Cruz, K. Schweiger, M. Senger, Y. Takahashi

National Central University, Chung-Li, Taiwan
C. Adloff[64], C. M. Kuo, W. Lin, S. S. Yu

National Taiwan University (NTU), Taipei, Taiwan
L. Ceard, Y. Chao, K. F. Chen, P.s. Chen, H. Cheng, W.-S. Hou, R. Khurana, Y. Y. Li, R.-S. Lu, E. Paganis, A. Psallidas, A. Steen, H.y. Wu, E. Yazgan, P.r. Yu

Department of Physics, Faculty of Science, Chulalongkorn University, Bangkok, Thailand
C. Asawatangtrakuldee, N. Srimanobhas

Physics Department, Science and Art Faculty, Çukurova University, Adana, Turkey
D. Agyel, F. Boran, Z. S. Demiroglu, F. Dolek, I. Dumanoglu[65], E. Eskut, Y. Guler[66], E. Gurpinar Guler[66], C. Isik, O. Kara, A. Kayis Topaksu, U. Kiminsu, G. Onengut, K. Ozdemir[67], A. Polatoz, A. E. Simsek, B. Tali[68], U. G. Tok, S. Turkcapar, E. Uslan, I. S. Zorbakir

Physics Department, Middle East Technical University, Ankara, Turkey
G. Karapinar[69], K. Ocalan[70], M. Yalvac[71]

Bogazici University, Istanbul, Turkey
B. Akgun, I. O. Atakisi, E. Gülmez, M. Kaya[72], O. Kaya[73], Ö. Özçelik, S. Tekten[74]

Istanbul Technical University, Istanbul, Turkey
A. Cakir, K. Cankocak[65], Y. Komurcu, S. Sen[75]

Istanbul University, Istanbul, Turkey
O. Aydilek, S. Cerci[68], B. Hacisahinoglu, I. Hos[76], B. Isildak[77], B. Kaynak, S. Ozkorucuklu, C. Simsek, D. Sunar Cerci[68]

Institute for Scintillation Materials of National Academy of Science of Ukraine, Kharkiv, Ukraine
B. Grynyov

National Science Centre, Kharkiv Institute of Physics and Technology, Kharkiv, Ukraine
L. Levchuk

University of Bristol, Bristol, UK
D. Anthony, E. Bhal, J. J. Brooke, A. Bundock, E. Clement, D. Cussans, H. Flacher, M. Glowacki, J. Goldstein, G. P. Heath, H. F. Heath, L. Kreczko, B. Krikler, S. Paramesvaran, S. Seif El Nasr-Storey, V. J. Smith, N. Stylianou[78], K. Walkingshaw Pass, R. White

Rutherford Appleton Laboratory, Didcot, UK
A. H. Ball, K. W. Bell, A. Belyaev[79], C. Brew, R. M. Brown, D. J. A. Cockerill, C. Cooke, K. V. Ellis,

K. Harder, S. Harper, M.-L. Holmberg[80], J. Linacre, K. Manolopoulos, D. M. Newbold, E. Olaiya, D. Petyt, T. Reis, G. Salvi, T. Schuh, C. H. Shepherd-Themistocleous, I. R. Tomalin, T. Williams

Imperial College, London, UK
R. Bainbridge, P. Bloch, S. Bonomally, J. Borg, S. Breeze, C. E. Brown, O. Buchmuller, V. Cacchio, V. Cepaitis, G. S. Chahal[81], D. Colling, J. S. Dancu, P. Dauncey, G. Davies, J. Davies, M. Della Negra, S. Fayer, G. Fedi, G. Hall, M. H. Hassanshahi, A. Howard, G. Iles, J. Langford, L. Lyons, A.-M. Magnan, S. Malik, A. Martelli, M. Mieskolainen, D. G. Monk, J. Nash[82], M. Pesaresi, B. C. Radburn-Smith, D. M. Raymond, A. Richards, A. Rose, E. Scott, C. Seez, A. Shtipliyski, R. Shukla, A. Tapper, K. Uchida, G. P. Uttley, L. H. Vage, T. Virdee[28], M. Vojinovic, N. Wardle, S. N. Webb, D. Winterbottom

Brunel University, Uxbridge, UK
K. Coldham, J. E. Cole, A. Khan, P. Kyberd, I. D. Reid

Baylor University, Waco, TX, USA
S. Abdullin, A. Brinkerhoff, B. Caraway, J. Dittmann, K. Hatakeyama, A. R. Kanuganti, B. McMaster, M. Saunders, S. Sawant, C. Sutantawibul, J. Wilson

Catholic University of America, Washington, DC, USA
R. Bartek, A. Dominguez, R. Uniyal, A. M. Vargas Hernandez

The University of Alabama, Tuscaloosa, AL, USA
A. Buccilli, S. I. Cooper, D. Di Croce, S. V. Gleyzer, C. Henderson, C. U. Perez, P. Rumerio[83], C. West

Boston University, Boston, MA, USA
A. Akpinar, A. Albert, D. Arcaro, C. Cosby, Z. Demiragli, C. Erice, E. Fontanesi, D. Gastler, S. May, J. Rohlf, K. Salyer, D. Sperka, D. Spitzbart, I. Suarez, A. Tsatsos, S. Yuan

Brown University, Providence, RI, USA
G. Benelli, B. Burkle, X. Coubez[24], D. Cutts, M. Hadley, U. Heintz, J. M. Hogan[84], T. Kwon, G. Landsberg, K. T. Lau, D. Li, J. Luo, M. Narain, N. Pervan, S. Sagir[85], F. Simpson, E. Usai, W. Y. Wong, X. Yan, D. Yu, W. Zhang

University of California, Davis, Davis, CA, USA
J. Bonilla, C. Brainerd, R. Breedon, M. Calderon De La Barca Sanchez, M. Chertok, J. Conway, P. T. Cox, R. Erbacher, G. Haza, F. Jensen, O. Kukral, G. Mocellin, M. Mulhearn, D. Pellett, B. Regnery, D. Taylor, Y. Yao, F. Zhang

University of California, Los Angeles, CA, USA
M. Bachtis, R. Cousins, A. Datta, D. Hamilton, J. Hauser, M. Ignatenko, M. A. Iqbal, T. Lam, E. Manca, W. A. Nash, S. Regnard, D. Saltzberg, B. Stone, V. Valuev

University of California, Riverside, Riverside, CA, USA
Y. Chen, R. Clare, J. W. Gary, M. Gordon, G. Hanson, G. Karapostoli, O. R. Long, N. Manganelli, W. Si, S. Wimpenny

University of California, San Diego, La Jolla, CA, USA
J. G. Branson, P. Chang, S. Cittolin, S. Cooperstein, D. Diaz, J. Duarte, R. Gerosa, L. Giannini, J. Guiang, R. Kansal, V. Krutelyov, R. Lee, J. Letts, M. Masciovecchio, F. Mokhtar, M. Pieri, B. V. Sathia Narayanan, V. Sharma, M. Tadel, F. Würthwein, Y. Xiang, A. Yagil

Department of Physics, University of California, Santa Barbara, Santa Barbara, CA, USA
N. Amin, C. Campagnari, M. Citron, G. Collura, A. Dorsett, V. Dutta, J. Incandela, M. Kilpatrick, J. Kim, A. J. Li, P. Masterson, H. Mei, M. Oshiro, M. Quinnan, J. Richman, U. Sarica, R. Schmitz, F. Setti, J. Sheplock, P. Siddireddy, D. Stuart, S. Wang

California Institute of Technology, Pasadena, CA, USA
A. Bornheim, O. Cerri, I. Dutta, J. M. Lawhorn, N. Lu, J. Mao, H. B. Newman, T. Q. Nguyen, M. Spiropulu, J. R. Vlimant, C. Wang, S. Xie, R. Y. Zhu

Carnegie Mellon University, Pittsburgh, PA, USA
J. Alison, S. An, M. B. Andrews, P. Bryant, T. Ferguson, A. Harilal, C. Liu, T. Mudholkar, S. Murthy, M. Paulini, A. Roberts, A. Sanchez, W. Terrill

University of Colorado Boulder, Boulder, CO, USA
J. P. Cumalat, W. T. Ford, A. Hassani, G. Karathanasis, E. MacDonald, F. Marini, R. Patel, A. Perloff, C. Savard, N. Schonbeck, K. Stenson, K. A. Ulmer, S. R. Wagner, N. Zipper

Cornell University, Ithaca, NY, USA
J. Alexander, S. Bright-Thonney, X. Chen, D. J. Cranshaw, J. Fan, X. Fan, D. Gadkari, S. Hogan, J. Monroy, J. R. Patterson, D. Quach, J. Reichert, M. Reid, A. Ryd, J. Thom, P. Wittich, R. Zou

Fermi National Accelerator Laboratory, Batavia, IL, USA
M. Albrow, M. Alyari, G. Apollinari, A. Apresyan, L. A. T. Bauerdick, D. Berry, J. Berryhill, P. C. Bhat, K. Burkett, J. N. Butler, A. Canepa, G. B. Cerati, H. W. K. Cheung, F. Chlebana, K. F. Di Petrillo, J. Dickinson, V. D. Elvira, Y. Feng, J. Freeman, A. Gandrakota, Z. Gecse, L. Gray, D. Green, S. Grünendahl, O. Gutsche, R. M. Harris, R. Heller, T. C. Herwig, J. Hirschauer, L. Horyn, B. Jayatilaka, S. Jindariani, M. Johnson, U. Joshi, T. Klijnsma, B. Klima, K. H. M. Kwok, S. Lammel, D. Lincoln, R. Lipton, T. Liu, C. Madrid, K. Maeshima, C. Mantilla, D. Mason, P. McBride, P. Merkel, S. Mrenna, S. Nahn, J. Ngadiuba, D. Noonan, V. Papadimitriou, N. Pastika, K. Pedro, C. Pena [86], F. Ravera, A. Reinsvold Hall [87], L. Ristori, E. Sexton-Kennedy, N. Smith, A. Soha, L. Spiegel, J. Strait, L. Taylor, S. Tkaczyk, N. V. Tran, L. Uplegger, E. W. Vaandering, H. A. Weber, I. Zoi

University of Florida, Gainesville, FL, USA
P. Avery, D. Bourilkov, L. Cadamuro, V. Cherepanov, R. D. Field, D. Guerrero, M. Kim, E. Koenig, J. Konigsberg, A. Korytov, K. H. Lo, K. Matchev, N. Menendez, G. Mitselmakher, A. Muthirakalayil Madhu, N. Rawal, D. Rosenzweig, S. Rosenzweig, K. Shi, J. Wang, Z. Wu

Florida State University, Tallahassee, FL, USA
T. Adams, A. Askew, R. Habibullah, V. Hagopian, T. Kolberg, G. Martinez, H. Prosper, C. Schiber, O. Viazlo, R. Yohay, J. Zhang

Florida Institute of Technology, Melbourne, FL, USA
M. M. Baarmand, S. Butalla, T. Elkafrawy [17], M. Hohlmann, R. Kumar Verma, M. Rahmani, F. Yumiceva

University of Illinois at Chicago (UIC), Chicago, IL, USA
M. R. Adams, H. Becerril Gonzalez, R. Cavanaugh, S. Dittmer, O. Evdokimov, C. E. Gerber, D. J. Hofman, D. S. Lemos, A. H. Merrit, C. Mills, G. Oh, T. Roy, S. Rudrabhatla, M. B. Tonjes, N. Varelas, X. Wang, Z. Ye, J. Yoo

The University of Iowa, Iowa City, IA, USA
M. Alhusseini, K. Dilsiz [88], L. Emediato, R. P. Gandrajula, G. Karaman, O. K. Köseyan, J.-P. Merlo, A. Mestvirishvili [89], J. Nachtman, O. Neogi, H. Ogul [90], Y. Onel, A. Penzo, C. Snyder, E. Tiras [91]

Johns Hopkins University, Baltimore, MD, USA
O. Amram, B. Blumenfeld, L. Corcodilos, J. Davis, A. V. Gritsan, L. Kang, S. Kyriacou, P. Maksimovic, J. Roskes, S. Sekhar, M. Swartz, T.Á. Vámi

The University of Kansas, Lawrence, KS, USA
A. Abreu, L. F. Alcerro Alcerro, J. Anguiano, P. Baringer, A. Bean, Z. Flowers, T. Isidori, S. Khalil, J. King, G. Krintiras, M. Lazarovits, C. Le Mahieu, C. Lindsey, J. Marquez, N. Minafra, M. Murray, M. Nickel, C. Rogan, C. Royon, R. Salvatico, S. Sanders, C. Smith, Q. Wang, J. Williams, G. Wilson

Kansas State University, Manhattan, KS, USA
B. Allmond, S. Duric, R. Gujju Gurunadha, A. Ivanov, K. Kaadze, D. Kim, Y. Maravin, T. Mitchell, A. Modak, K. Nam, J. Natoli, D. Roy

Lawrence Livermore National Laboratory, Livermore, CA, USA
F. Rebassoo, D. Wright

University of Maryland, College Park, MD, USA
E. Adams, A. Baden, O. Baron, A. Belloni, A. Bethani, S. C. Eno, N. J. Hadley, S. Jabeen, R. G. Kellogg, T. Koeth, Y. Lai, S. Lascio, A. C. Mignerey, S. Nabili, C. Palmer, C. Papageorgakis, L. Wang, K. Wong

Massachusetts Institute of Technology, Cambridge, MA, USA
D. Abercrombie, W. Busza, I. A. Cali, Y. Chen, M. D'Alfonso, J. Eysermans, C. Freer, G. Gomez-Ceballos, M. Goncharov, P. Harris, M. Hu, D. Kovalskyi, J. Krupa, Y. -J. Lee, K. Long, C. Mironov, C. Paus, D. Rankin, C. Roland, G. Roland, Z. Shi, G. S. F. Stephans, J. Wang, Z. Wang, B. Wyslouch

University of Minnesota, Minneapolis, MN, USA
R. M. Chatterjee, B. Crossman, A. Evans, J. Hiltbrand, Sh. Jain, B. M. Joshi, C. Kapsiak, M. Krohn, Y. Kubota, J. Mans, M. Revering, R. Rusack, R. Saradhy, N. Schroeder, N. Strobbe, M. A. Wadud

University of Mississippi, Oxford, MS, USA
L. M. Cremaldi

University of Nebraska-Lincoln, Lincoln, NE, USA
K. Bloom, M. Bryson, D. R. Claes, C. Fangmeier, L. Finco, F. Golf, C. Joo, I. Kravchenko, I. Reed, J. E. Siado, G. R. Snow†, W. Tabb, A. Wightman, F. Yan, A. G. Zecchinelli

State University of New York at Buffalo, Buffalo, NY, USA
G. Agarwal, H. Bandyopadhyay, L. Hay, I. Iashvili, A. Kharchilava, C. McLean, M. Morris, D. Nguyen, J. Pekkanen, S. Rappoccio, A. Williams

Northeastern University, Boston, MA, USA
G. Alverson, E. Barberis, Y. Haddad, Y. Han, A. Krishna, J. Li, J. Lidrych, G. Madigan, B. Marzocchi, D. M. Morse, V. Nguyen, T. Orimoto, A. Parker, L. Skinnari, A. Tishelman-Charny, T. Wamorkar, B. Wang, A. Wisecarver, D. Wood

Northwestern University, Evanston, IL, USA
S. Bhattacharya, J. Bueghly, Z. Chen, A. Gilbert, K. A. Hahn, Y. Liu, N. Odell, M. H. Schmitt, M. Velasco

University of Notre Dame, Notre Dame, IN, USA
R. Band, R. Bucci, S. Castells, M. Cremonesi, A. Das, R. Goldouzian, M. Hildreth, K. Hurtado Anampa, C. Jessop, K. Lannon, J. Lawrence, N. Loukas, L. Lutton, J. Mariano, N. Marinelli, I. Mcalister, T. McCauley, C. Mcgrady, K. Mohrman, C. Moore, Y. Musienko[13], H. Nelson, R. Ruchti, A. Townsend, M. Wayne, H. Yockey, M. Zarucki, L. Zygala

The Ohio State University, Columbus, OH, USA
B. Bylsma, M. Carrigan, L. S. Durkin, B. Francis, C. Hill, A. Lesauvage, M. Nunez Ornelas, K. Wei, B. L. Winer, B. R. Yates

Princeton University, Princeton, NJ, USA
F. M. Addesa, P. Das, G. Dezoort, P. Elmer, A. Frankenthal, B. Greenberg, N. Haubrich, S. Higginbotham, A. Kalogeropoulos, G. Kopp, S. Kwan, D. Lange, D. Marlow, K. Mei, I. Ojalvo, J. Olsen, D. Stickland, C. Tully

University of Puerto Rico, Mayaguez, PR, USA
S. Malik, S. Norberg

Purdue University, West Lafayette, IN, USA
A. S. Bakshi, V. E. Barnes, R. Chawla, S. Das, L. Gutay, M. Jones, A. W. Jung, D. Kondratyev, A. M. Koshy, M. Liu, G. Negro, N. Neumeister, G. Paspalaki, S. Piperov, A. Purohit, J. F. Schulte, M. Stojanovic, J. Thieman, F. Wang, R. Xiao, W. Xie

Purdue University Northwest, Hammond, IN, USA
J. Dolen, N. Parashar

Rice University, Houston, TX, USA
D. Acosta, A. Baty, T. Carnahan, M. Decaro, S. Dildick, K. M. Ecklund, P. J. Fernández Manteca, S. Freed, P. Gardner, F. J. M. Geurts, A. Kumar, W. Li, B. P. Padley, R. Redjimi, J. Rotter, W. Shi, S. Yang, E. Yigitbasi, L. Zhang[92], Y. Zhang

University of Rochester, Rochester, NY, USA
A. Bodek, P. de Barbaro, R. Demina, J. L. Dulemba, C. Fallon, T. Ferbel, M. Galanti, A. Garcia-Bellido, O. Hindrichs, A. Khukhunaishvili, E. Ranken, R. Taus, G. P. Van Onsem

The Rockefeller University, New York, NY, USA
K. Goulianos

Rutgers, The State University of New Jersey, Piscataway, NJ, USA
B. Chiarito, J. P. Chou, Y. Gershtein, E. Halkiadakis, A. Hart, M. Heindl, D. Jaroslawski, O. Karacheban[26], I. Laflotte, A. Lath, R. Montalvo, K. Nash, M. Osherson, S. Salur, S. Schnetzer, S. Somalwar, R. Stone, S. A. Thayil, S. Thomas, H. Wang

University of Tennessee, Knoxville, TN, USA
H. Acharya, A. G. Delannoy, S. Fiorendi, T. Holmes, E. Nibigira, S. Spanier

Texas A&M University, College Station, TX, USA
O. Bouhali[93], M. Dalchenko, A. Delgado, R. Eusebi, J. Gilmore, T. Huang, T. Kamon[94], H. Kim, S. Luo, S. Malhotra, R. Mueller, D. Overton, D. Rathjens, A. Safonov

Texas Tech University, Lubbock, TX, USA
N. Akchurin, J. Damgov, V. Hegde, K. Lamichhane, S. W. Lee, T. Mengke, S. Muthumuni, T. Peltola, I. Volobouev, Z. Wang, A. Whitbeck

Vanderbilt University, Nashville, TN, USA
E. Appelt, S. Greene, A. Gurrola, W. Johns, A. Melo, F. Romeo, P. Sheldon, S. Tuo, J. Velkovska, J. Viinikainen

University of Virginia, Charlottesville, VA, USA
B. Cardwell, B. Cox, G. Cummings, J. Hakala, R. Hirosky, M. Joyce, A. Ledovskoy, A. Li, C. Neu, C. E. Perez Lara, B. Tannenwald

Wayne State University, Detroit, MI, USA
P. E. Karchin, N. Poudyal

University of Wisconsin-Madison, Madison, WI, USA
S. Banerjee, K. Black, T. Bose, S. Dasu, I. De Bruyn, P. Everaerts, C. Galloni, H. He, M. Herndon, A. Herve, C. K. Koraka, A. Lanaro, A. Loeliger, R. Loveless, J. Madhusudanan Sreekala, A. Mallampalli, A. Mohammadi, S. Mondal, G. Parida, D. Pinna, A. Savin, V. Shang, V. Sharma, W. H. Smith, D. Teague, H. F. Tsoi, W. Vetens

Authors Affiliated with an Iinstitute or an International Laboratory Covered by a Cooperation Agreement with CERN,
Geneva, Switzerland
S. Afanasiev, V. Andreev, Yu. Andreev, T. Aushev, M. Azarkin, A. Babaev, A. Belyaev, V. Blinov[95], E. Boos, V. Borshch, D. Budkouski, V. Bunichev, O. Bychkova, V. Chekhovsky, R. Chistov[95], M. Danilov[95], A. Dermenev, T. Dimova[95], I. Dremin, M. Dubinin[86], L. Dudko, V. Epshteyn, G. Gavrilov, V. Gavrilov, S. Gninenko, V. Golovtcov, N. Golubev, I. Golutvin, I. Gorbunov, A. Gribushin, V. Ivanchenko, Y. Ivanov, V. Kachanov, L. Kardapoltsev[95], V. Karjavine, A. Karneyeu, V. Kim[95], M. Kirakosyan, D. Kirpichnikov, M. Kirsanov, V. Klyukhin, O. Kodolova[96], D. Konstantinov, V. Korenkov, A. Kozyrev[95], N. Krasnikov, E. Kuznetsova[97], A. Lanev, P. Levchenko, A. Litomin, N. Lychkovskaya, V. Makarenko, A. Malakhov, V. Matveev[95], V. Murzin, A. Nikitenko[98], S. Obraztsov, V. Okhotnikov,

I. Ovtin[95], V. Palichik, P. Parygin, V. Perelygin, M. Perfilov, S. Petrushanko, G. Pivovarov, S. Polikarpov[95], V. Popov, O. Radchenko[95], M. Savina, V. Savrin, D. Selivanova, V. Shalaev, S. Shmatov, S. Shulha, Y. Skovpen[95], S. Slabospitskii, V. Smirnov, D. Sosnov, A. Stepennov, V. Sulimov, E. Tcherniaev, A. Terkulov, O. Teryaev, I. Tlisova, M. Toms, A. Toropin, L. Uvarov, A. Uzunian, E. Vlasov, A. Vorobyev, N. Voytishin, B. S. Yuldashev[99], A. Zarubin, I. Zhizhin, A. Zhokin

† **Deceased**

1: Also at Yerevan State University, Yerevan, Armenia
2: Also at TU Wien, Vienna, Austria
3: Also at Institute of Basic and Applied Sciences, Faculty of Engineering, Arab Academy for Science, Technology and Maritime Transport, Alexandria, Egypt
4: Also at Université Libre de Bruxelles, Brussels, Belgium
5: Also at Universidade Estadual de Campinas, Campinas, Brazil
6: Also at Federal University of Rio Grande do Sul, Porto Alegre, Brazil
7: Also at UFMS, Nova Andradina, Brazil
8: Also at The University of the State of Amazonas, Manaus, Brazil
9: Also at University of Chinese Academy of Sciences, Beijing, China
10: Also at Nanjing Normal University Department of Physics, Nanjing, China
11: Now at The University of Iowa, Iowa City, IA, USA
12: Also at University of Chinese Academy of Sciences, Beijing, China
13: Also at an Institute or an International Laboratory Covered by a Cooperation Agreement with CERN, Geneva, Switzerland
14: Also at Helwan University, Cairo, Egypt
15: Now at Zewail City of Science and Technology, Zewail, Egypt
16: Also at British University in Egypt, Cairo, Egypt
17: Now at Ain Shams University, Cairo, Egypt
18: Also at Purdue University, West Lafayette, IN, USA
19: Also at Université de Haute Alsace, Mulhouse, France
20: Also at Department of Physics, Tsinghua University, Beijing, China
21: Also at Ilia State University, Tbilisi, Georgia
22: Also at Erzincan Binali Yildirim University, Erzincan, Turkey
23: Also at University of Hamburg, Hamburg, Germany
24: Also at RWTH Aachen University, III. Physikalisches Institut A, Aachen, Germany
25: Also at Isfahan University of Technology, Isfahan, Iran
26: Also at Brandenburg University of Technology, Cottbus, Germany
27: Also at Forschungszentrum Jülich, Juelich, Germany
28: Also at CERN, European Organization for Nuclear Research, Geneva, Switzerland
29: Also at Physics Department, Faculty of Science, Assiut University, Assiut, Egypt
30: Also at Karoly Robert Campus, MATE Institute of Technology, Gyongyos, Hungary
31: Also at Wigner Research Centre for Physics, Budapest, Hungary
32: Also at Institute of Physics, University of Debrecen, Debrecen, Hungary
33: Also at Institute of Nuclear Research ATOMKI, Debrecen, Hungary
34: Now at Universitatea Babes-Bolyai-Facultatea de Fizica, Cluj-Napoca, Romania
35: Also at Faculty of Informatics, University of Debrecen, Debrecen, Hungary
36: Also at Punjab Agricultural University, Ludhiana, India
37: Also at UPES-University of Petroleum and Energy Studies, Dehradun, India
38: Also at University of Visva-Bharati, Santiniketan, India
39: Also at University of Hyderabad, Hyderabad, India
40: Also at Indian Institute of Science (IISc), Bangalore, India
41: Also at Indian Institute of Technology (IIT), Mumbai, India
42: Also at IIT Bhubaneswar, Bhubaneswar, India
43: Also at Institute of Physics, Bhubaneswar, India
44: Also at Deutsches Elektronen-Synchrotron, Hamburg, Germany

45: Also at Sharif University of Technology, Tehran, Iran
46: Also at Department of Physics, University of Science and Technology of Mazandaran, Behshahr, Iran
47: Also at Italian National Agency for New Technologies, Energy and Sustainable Economic Development, Bologna, Italy
48: Also at Centro Siciliano di Fisica Nucleare e di Struttura Della Materia, Catania, Italy
49: Also at Scuola Superiore Meridionale, Università di Napoli 'Federico II', Naples, Italy
50: Also at Fermi National Accelerator Laboratory, Batavia, IL, USA
51: Also at Laboratori Nazionali di Legnaro dell'INFN, Legnaro, Italy
52: Also at Università di Napoli 'Federico II', Naples, Italy
53: Also at Consiglio Nazionale delle Ricerche-Istituto Officina dei Materiali, Perugia, Italy
54: Also at Department of Applied Physics, Faculty of Science and Technology, Universiti Kebangsaan Malaysia, Bangi, Malaysia
55: Also at Consejo Nacional de Ciencia y Tecnología, Mexico, Mexico
56: Also at IRFU, CEA, Université Paris-Saclay, Gif-sur-Yvette, France
57: Also at Faculty of Physics, University of Belgrade, Belgrade, Serbia
58: Also at Trincomalee Campus, Eastern University, Sri Lanka, Nilaveli, Sri Lanka
59: Also at INFN Sezione di Pavia, Università di Pavia, Pavia, Italy
60: Also at National and Kapodistrian University of Athens, Athens, Greece
61: Also at Ecole Polytechnique Fédérale Lausanne, Lausanne, Switzerland
62: Also at Universität Zürich, Zurich, Switzerland
63: Also at Stefan Meyer Institute for Subatomic Physics, Vienna, Austria
64: Also at Laboratoire d'Annecy-le-Vieux de Physique des Particules, IN2P3-CNRS, Annecy-le-Vieux, France
65: Also at Near East University, Research Center of Experimental Health Science, Mersin, Turkey
66: Also at Konya Technical University, Konya, Turkey
67: Also at Izmir Bakircay University, Izmir, Turkey
68: Also at Adiyaman University, Adiyaman, Turkey
69: Also at Istanbul Gedik University, Istanbul, Turkey
70: Also at Necmettin Erbakan University, Konya, Turkey
71: Also at Bozok Universitetesi Rektörlügü, Yozgat, Turkey
72: Also at Marmara University, Istanbul, Turkey
73: Also at Milli Savunma University, Istanbul, Turkey
74: Also at Kafkas University, Kars, Turkey
75: Also at Hacettepe University, Ankara, Turkey
76: Also at Faculty of Engineering, Istanbul University-Cerrahpasa, Istanbul, Turkey
77: Also at Yildiz Technical University, Istanbul, Turkey
78: Also at Vrije Universiteit Brussel, Brussels, Belgium
79: Also at School of Physics and Astronomy, University of Southampton, Southampton, UK
80: Also at University of Bristol, Bristol, UK
81: Also at IPPP Durham University, Durham, UK
82: Also at Faculty of Science, Monash University, Clayton, Australia
83: Also at Università di Torino, Turin, Italy
84: Also at Bethel University, St. Paul, MN, USA
85: Also at Karamanoğlu Mehmetbey University, Karaman, Turkey
86: Also at California Institute of Technology, Pasadena, CA, USA
87: Also at United States Naval Academy, Annapolis, MD, USA
88: Also at Bingol University, Bingol, Turkey
89: Also at Georgian Technical University, Tbilisi, Georgia
90: Also at Sinop University, Sinop, Turkey
91: Also at Erciyes University, Kayseri, Turkey
92: Also at Institute of Modern Physics and Key Laboratory of Nuclear Physics and Ion-beam Application (MOE)-Fudan University, Shanghai, China
93: Also at Texas A&M University at Qatar, Doha, Qatar
94: Also at Kyungpook National University, Daegu, South Korea

95: Also at Another Institute or International Laboratory Covered by a Cooperation Agreement with CERN, Geneva, Switzerland
96: Also at Yerevan Physics Institute, Yerevan, Armenia
97: Now at University of Florida, Gainesville, FL, USA
98: Also at Imperial College, London, UK
99: Also at Institute of Nuclear Physics of the Uzbekistan Academy of Sciences, Tashkent, Uzbekistan